

# **Single-Unit Leadless EEG Sensor**

by

**Bo Luan**

B.S. in Electrical Engineering, University of Pittsburgh, 2012

M.S. in Electrical Engineering, University of Pittsburgh, 2013

Submitted to the Graduate Faculty of

The Swanson School of Engineering in partial fulfillment

of the requirements for the degree of

**Doctor of Philosophy**

University of Pittsburgh

2017

UNIVERSITY OF PITTSBURGH  
SWANSON SCHOOL OF ENGINEERING

This dissertation was presented

by

**Bo Luan**

It was defended on

July 10, 2017

and approved by

Mingui Sun, Ph.D., Professor  
Depts. of Neurological Surgery, Electrical & Computer Engineering, and Bioengineering

Yiran Chen, Ph.D., Associate Professor  
Department of Electrical & Computer Engineering

Wenyan Jia, Ph.D., Research Assistant Professor  
Department of Neurological Surgery

Zhi-Hong Mao, Ph.D., Associate Professor  
Departments of Electrical & Computer Engineering, and Bioengineering

Robert J. Sclabassi, M.D., Ph.D., Professor Emeritus, CEO  
Computational Diagnostics, Inc.

Ervin Sejdić, Ph.D., Associate Professor  
Departments of Electrical & Computer Engineering, and Bioengineering

Dissertation Director: Mingui Sun, Ph.D., Professor  
Depts. of Neurological Surgery, Electrical & Computer Engineering, and Bioengineering

Copyright © by Bo Luan

2017

# **SINGLE-UNIT LEADLESS EEG SENSOR**

Bo Luan, PhD

University of Pittsburgh, 2017

Non-convulsive seizure (NCS) and non-convulsive status epilepticus (NCSE) are severe neurological disorders within intensive care units (ICUs) and emergency departments (EDs). Traditionally, physiological monitoring in ICUs and EDs focuses on cardiopulmonary variables, including blood pressure and heart rate. The neurological conditions, on the other hand, are often assessed by bedside observations from physicians. Without proper monitoring tools, the NCS and NCSE that lack observable clinical manifestations are easily overlooked or misdiagnosed. The problem can be amplified among patients with impaired consciousness who cannot respond to environmental stimuli. The delayed detection and treatment lead to substantial morbidity, mortality, and healthcare costs.

Currently, electroencephalography (EEG) is the most effective diagnostic tool for NCS and NCSE in ICUs and EDs. Meanwhile, less than two percent of the critically ill patients in ICUs and EDs are undergoing EEG. The under-adoption or decreased utilization of EEG originates from challenges to accommodate EEG into established practice protocols. Therefore, the timely acquisition of EEG has been one of the paramount needs in today's emergency care.

This dissertation presents a novel EEG sensor that is leadless, self-contained, and the size of a U.S. Penny. The sensor enables rapid EEG setup and efficient EEG acquisition. The dissertation first investigated into a novel EEG electrode-structure enclosing four unique arc-shaped electrodes. We demonstrated the feasibility of such electrode configuration by experimental investigations on both a physical model and a healthy human subject. The

dissertation then presented Monte Carlo simulations to predict the statistical performance of the single-unit sensor on the whole brain. A forward computation algorithm was implemented to compute the scalp potential in response to dipolar sources within an analytically modeled brain. The data-informed findings indicated that the whole-brain quantitative performance of this electrode configuration is comparable to the cup electrode currently used as the gold standard. The results are presented in a multi-variant probability density function. Taken a step further, a deterministic solution to such probability model was derived. These results provide insights into the workings of the single-unit sensor. Furthermore, a single-unit sensor prototype was constructed with a specially designed electronic system. The performance of the prototype was validated through experiments on a healthy human subject. Lastly, the efficacy of the prototype is demonstrated indirectly using pre-recorded EEG data from epilepsy patients. It has been observed that seizure signal can be detected via a neighboring bipolar recording configuration, which closely simulates the case of single-unit sensors for the detection of NCS and NCSE. The results of series of investigations conclude the feasibility and single-unit sensors in detecting epileptic EEG signals.

## TABLE OF CONTENTS

|   |             |
|---|-------------|
| <b>PREFACE.....</b>   | <b>XIII</b> |
| <b>1.0 INTRODUCTION.....</b>  | <b>1</b>    |
| <b>1.1 MOTIVATION OF THE WORK .....</b>                             | <b>1</b>    |
| <b>1.2 MAJOR GOALS OF THE WORK.....</b>                             | <b>3</b>    |
| <b>1.3 CONTRIBUTION OF THE WORK .....</b>                           | <b>5</b>    |
| <b>1.4 OUTLINE OF THE DISSERTATION.....</b>                         | <b>6</b>    |
| <b>2.0 BACKGROUND .....</b>   | <b>7</b>    |
| <b>2.1 NCS AND NCSE IN EMERGENCY CARE.....</b>                      | <b>7</b>    |
| <b>2.2 ELECTROENCEPHALOGRAPHY (EEG) .....</b>                       | <b>10</b>   |
| <b>2.2.1 History of EEG.....</b>                                    | <b>10</b>   |
| <b>2.2.2 Efficacy of EEG .....</b>                                  | <b>10</b>   |
| <b>2.2.3 Review of EEG Systems .....</b>                            | <b>12</b>   |
| <b>2.2.4 Practical Barriers to Adopt EEG in Emergency Care.....</b> | <b>16</b>   |
| <b>2.3 SKIN-GRABBING AND GEL-FREE EEG ELECTRODE.....</b>            | <b>18</b>   |
| <b>3.0 PROPOSED SYSTEM FOR RAPID EEG MEASUREMENT .....</b>          | <b>22</b>   |
| <b>3.1 OVERVIEW OF THE PROPOSED SYSTEM .....</b>                    | <b>22</b>   |
| <b>3.2 PRACTICAL BENEFITS OF THE PROPOSED SENSOR.....</b>           | <b>26</b>   |
| <b>4.0 FEASIBILITY DEMONSTRATION.....</b>                           | <b>28</b>   |
| <b>4.1 AN AMPLIFIER DESIGN FOR FEASIBILITY TESTS.....</b>           | <b>28</b>   |
| <b>4.2 EXPERIMENT ON PHYSICAL MODELS .....</b>                      | <b>31</b>   |
| <b>4.2.1 Experimental Design .....</b>                              | <b>31</b>   |

|         |   |    |
|---------|---|----|
| 4.2.2   | Verification with Simulation Program .....                      | 33 |
| 4.2.3   | Experimental Results .....                                      | 35 |
| 4.3     | EXPERIMENT ON HUMAN SUBJECT.....                                | 37 |
| 4.3.1   | Experimental Design .....                                       | 37 |
| 4.3.2   | Statistical Analysis.....                                       | 38 |
| 4.3.3   | Experimental Results .....                                      | 39 |
| 5.0     | FORWARD SOLUTION OF MULTI-SHELL MODELS .....                    | 45 |
| 5.1     | MONTE CARLO SIMULATION.....                                     | 45 |
| 5.1.1   | Simulation Method .....   | 45 |
| 5.1.1.1 | Concentric Multi-Shell Spherical Volume Conductor Model.....    | 46 |
| 5.1.1.2 | Current Dipole Source Models .....                              | 47 |
| 5.1.1.3 | An Algorithm for Computing EEG Forward Solution.....            | 49 |
| 5.1.2   | Experimental Results .....                                      | 54 |
| 5.2     | PROBABILISTIC MODELS FOR SOURCE-POTENTIAL<br>RELATIONSHIP ..... | 56 |
| 5.2.1   | Formation of the Mathematical Problem.....                      | 57 |
| 5.2.2   | Approach to the Mathematical Problem .....                      | 59 |
| 6.0     | HARDWARE DESIGN AND IMPLEMENTATION .....                        | 63 |
| 6.1     | PROTOTYPE DESIGN .....  | 63 |
| 6.2     | IMPROVED DESIGN.....  | 71 |
| 7.0     | EFFICACY DEMONSTRATION ON SINGLE-UNIT SENSOR .....              | 80 |
| 7.1     | HUMAN SUBJECT EXPERIMENT.....                                   | 80 |
| 7.1.1   | Experiment Protocol.....  | 81 |

|       |   |     |
|-------|---|-----|
| 7.1.2 | Experimental Results .....                                      | 85  |
| 7.2   | INDIRECT DEMONSTRATION FOR EFFICACY VALIDATION .....            | 94  |
| 7.2.1 | Rationality of Validation Study.....                            | 94  |
| 7.2.2 | Reference Conversion to Bipolar Montage .....                   | 96  |
| 7.2.3 | Experimental Results .....                                      | 98  |
| 8.0   | SUMMARY OF THE WORK AND FUTURE EXTENSIONS .....                 | 102 |
| 8.1   | DISCUSSION.....   | 103 |
| 8.2   | CONTRIBUTION OF THE WORK .....                                  | 104 |
| 8.3   | RECOMMENDATIONS FOR FUTURE EXTENSIONS.....                      | 104 |
|       | APPENDIX A. ABBREVIATIONS .....                                 | 107 |
|       | APPENDIX B. ADS1299 REGISTER MAP .....                          | 110 |
|       | APPENDIX C. SINGLE-UNIT SENSOR HARDWARE BILL OF MATERIALS ..... | 111 |
|       | APPENDIX D. ELECTRODE-SKIN CONTACT IMPEDANCE MEASUREMENTS....   | 113 |
|       | BIBLIOGRAPHY .....  | 114 |



## LIST OF TABLES

|   |    |
|---|----|
| Table 1. Letter indications of placement sites in 10-20 system.....                   | 14 |
| Table 2. Schematic of electrode connections in feasibility experiment.....            | 43 |
| Table 3. Comparison of single-unit sensor and electrodes employing 10-20 mapping..... | 55 |
| Table 4. Gold cup electrode designated geometric scale and actual measurement .....   | 93 |
| Table 5. Referential montage recording pairs .....                                    | 98 |
| Table 6. Bipolar montage recording pairs derived from Table 5.....                    | 98 |

## LIST OF FIGURES

|  |    |
|--|----|
| Figure 1. Schematic of the teeth structure on the skin-screw electrode.....                        | 19 |
| Figure 2. An actual skin-screw electrode and the microscopic view of the teeth structure.....      | 20 |
| Figure 3. Statistical comparison between the disc electrode and the skin-screw electrode.....      | 21 |
| Figure 4. Schematic of the single-unit sensor. ....  | 22 |
| Figure 5. An actual single-unit sensor and the microscopic view of its skin-contacting surface.    | 23 |
| Figure 6. The operation mechanism of the switches implemented in the single-unit sensor. ....      | 24 |
| Figure 7. The single-unit sensor working concept.....  | 25 |
| Figure 8. Schematic diagram of the EEG amplifier circuitry. ....                                   | 28 |
| Figure 9. Picture of the actual circuitry used for feasibility test. ....                          | 30 |
| Figure 10. The physical models constructed for the experiment. ....                                | 31 |
| Figure 11. The dipolar source model presents in (a) side view and (b) front view. ....             | 32 |
| Figure 12. Schematic of the experimental platform.....   | 33 |
| Figure 13. The interface of the simulation program. ....   | 35 |
| Figure 14. The acquired signal from the physical model.....  | 36 |
| Figure 15. Four gold cup electrodes were installed closely at the occipital region of the scalp... | 37 |
| Figure 16. Typical EEG waveforms collected during experiments. ....                                | 41 |
| Figure 17. Spectral plots of signals collected from six electrode orientations. ....               | 42 |
| Figure 18. Box plot of alpha-wave energy in six electrode orientations. ....                       | 43 |
| Figure 19. A four-layer spherical volume conductor model.....                                      | 47 |
| Figure 20. Visualization of simulation program created in this study. ....                         | 51 |
| Figure 21. Randomly generate sensor locations on the sphere surface. ....                          | 52 |

|   |    |
|---|----|
| Figure 22. Randomly generate dipole locations within the layer of gray matter.....              | 53 |
| Figure 23. The potential distribution plots.....  | 55 |
| Figure 24. Block diagram of the prototype electronic system.....                                | 63 |
| Figure 25. The ADS1299 bio-potential front-end and its external circuitry.....                  | 66 |
| Figure 26. The schematic of the MSP430 microcontroller and the RN-42 Bluetooth module. ...      | 67 |
| Figure 27. The power management circuit. ....   | 68 |
| Figure 28. The PCB layout design and the produced board. ....                                   | 69 |
| Figure 29. Raw EEG signal acquired using the circuit board presented in Figure 28 (c). ....     | 70 |
| Figure 30. PSD plot of the 150-second EEG signal acquired from the board. ....                  | 70 |
| Figure 31. Block diagram of the single-unit sensor electronics system .....                     | 71 |
| Figure 32. The improved schematic for ADS1299 front-end and external circuitry.....             | 75 |
| Figure 33. Schematic for ATmega328p MCU and its external circuitry.....                         | 76 |
| Figure 34. Schematic for the power management system. ....                                      | 77 |
| Figure 35. The electronic system acquired testing signals generated by function generator. .... | 79 |
| Figure 36. Flow of the experiment procedures. ....  | 81 |
| Figure 37. Four single-unit sensor electrode structure prototypes.....                          | 83 |
| Figure 38. Placement configuration of the four gold cup electrodes. ....                        | 83 |
| Figure 39. EEG recording environment using the single-unit sensor prototype.....                | 84 |
| Figure 40. The EEG signals acquired while performing Task 1.....                                | 85 |
| Figure 41. The EEG signals acquired while performing Task 2.....                                | 86 |
| Figure 42. The EEG signals acquired while performing Task 3.....                                | 87 |
| Figure 43. PSD plots of two experiment sessions using the 20-mm-diameter single-unit sensor.    | 88 |
| Figure 44. Spectral plots of data recorded using the 20-mm-diameter single-unit sensor. ....    | 89 |

|  |     |
|--|-----|
| Figure 45. PSD plots of two experiment sessions using gold cup electrodes..... | 90  |
| Figure 46. Spectral plots of data recorded using the gold cup electrodes.....  | 91  |
| Figure 47. Alpha frequency band signal energy comparison. ....                 | 92  |
| Figure 48. Three views of 128 channel locations in 3D space .....              | 96  |
| Figure 49. Established adjacent bipolar recording pairs .....                  | 97  |
| Figure 50. Topographic energy maps of the epileptic EEG signals .....          | 100 |
| Figure 51. Time series plot of 3-second epileptic EEG signals.....             | 101 |

## PREFACE

I have always been amazed by sciences and technologies that save and promote people's life. Having my Ph.D. study as a valuable opportunity to catch a glimpse of it is one of the best things happened in my life. I am very grateful to people who provided me with the opportunity and those who encouraged me along the way.

To my supervisor, Dr. Mingui Sun, whom offered me the valuable opportunity and has spared no efforts to guide me. For years, I have thought about a proper way to express a sincere "thank you" to him, but then I realized no words can ever describe my heartfelt gratitude and respect to him. Dr. Sun's mind and many other things I learned are the most precious life-changing gift I obtained during my Ph.D. life to carry on and live confidently many years ahead.

My sincere appreciation to my committee members whom spared their precious time and provided valuable expertise to help me: Dr. Robert J. Sclabassi, Dr. Zhi-Hong Mao, Dr. Yiran Chen, Dr. Wenyan Jia, Dr. Ervin Sejdić, and Dr. Mingui Sun. I am grateful to learn from and supported by those great minds.

I am also thankful to Dr. William Stanchina for his tuition support in Spring 2015, Dr. Ching-Chung Li for his guidance on many courses and projects, Sandy Weisberg for her continuous advises. Also thank Dr. Yaguang Zheng, Dr. Parthasarathy Thirumala, William Mcgahey. I appreciate colleagues I met at Dr. Sun's lab, including Yicheng Bai, Yuecheng Li, Hao Wang, and Paresh Vasandani. I learned from their fields of expertise and dedicated attitudes. I want to thank many kind people in the Pitt community for offering me help, and creating an excellent atmosphere for us to research, study, and live.

Thank my friends all over the world for their kind bless, and all the good memories we had together. Thank Ran Sun for always encouraging me with a big and confident heart.

To my grandmother, aunt, uncles, brother, and other family members for always taking care of me and keeping me in mind. To my grandfather whom I forever in debt to, I will fight harder and live better to make you proud.

Finally, with no doubt, I could never imagine any of the wonderful things ever possible to me without the endless love from my mom and dad.

Bo Luan

July 2017 in Pittsburgh

## **1.0 INTRODUCTION**

### **1.1 MOTIVATION OF THE WORK**

Non-convulsive seizure (NCS) and non-convulsive status epilepticus (NCSE) are severe neurological disorders. Previous clinical studies reported their association with protracted mortality (18% – 57% [1, 2]) and substantial morbidity (39% [1]). The majority of seizures in intensive care units (ICUs) and emergency departments (EDs) are non-convulsive (8% – 20% [3]). Compare to other neurological disorders, NCS/NCSE lack overt and tonic-clonic clinical manifestations [4]. Their clinical signs are often subtle or even absent [5]. These make NCS/NCSE usually go unrecognized without proper monitoring tools.

Electroencephalography (EEG) has proven to be a prominent tool for diagnosing NCS/NCSE during the emergency and critical care process [3, 6-9]. EEG enables timely, ongoing, and bedside monitoring while providing therapeutically valuable insights on cerebral functions. Despite its merits, the current clinical assessment of patients' neurological functions in ICUs and EDs are primarily dependent on clinical bedside observations or “neurochecks” [10], which are often discrete or subjective. The adoption of EEG in the emergency and critical care remains inadequate [11].

The under-adoption of EEG in emergency medicine is because the timely acquisition of EEG is particularly challenging. For instance, the EEG preparation procedures are tedious,

uncomfortable, and time-consuming. It is a common practice to use collodion to interface and secure electrodes to the scalp although the nitrocellulose-based compound is highly flammable and hazardous. Regularly, abrasion is required to remove stratum corneum to reduce skin impedance. In some circumstances, removal of hair is necessary to interface cup electrodes to the scalp better. Moreover, electric leads are required to connect electrodes to the amplifier box, interfering with clinical management. More importantly, the procedure requires about 20-45 minutes for a professionally trained medical personnel, during which medical personnel cannot complete other significant procedures in parallel. Many other logistical, technological, and financial barriers have been accounted for the problem of EEG application at current emergency setting. Subsequently, most of the emergency settings emphasize the continuous monitoring of cardio, renal, and pulmonary functions [12, 13]. Intracranial pressure is often the only monitoring tool to the brain in a general ICU, and this monitoring is mostly an invasive procedure.

Therefore, it is a paramount need in today's emergency care to bring a disruptive change in the way of acquiring EEG so that accurate EEG could be obtained conveniently with less labor effort and better cost-efficiency in ICUs and EDs. It should also relieve the burdens on patients. The experience of collecting EEG should be as easy as collecting ECG.

To address the unmet clinical need, this work presents the design of a novel EEG sensor by combining formerly separated functional blocks of a traditional EEG collection system into an integrated but miniature piece. Multiple electrodes, amplifiers, analog-to-digital converters (ADCs), microcontroller, data transmission modules, coin battery, and other components are aggregated into a unitary, self-contained tiny piece of hardware while eliminating all leads and cords to make the device completely leadless. We name this device as the "single-unit leadless EEG sensor", or the "single-unit sensor" in short. This unique sensor idea has been patent-



disclosed in 2017 [14]. By merely pressing the new EEG sensor against the patient's unprepared scalp and twist slightly, the device attaches to the scalp and start to collect EEG.

## **1.2 MAJOR GOALS OF THE WORK**

The entire study on the single-unit sensor was accomplished through completing four major and consecutive goals.

The first goal was to demonstrate the feasibility of a novel electrode configuration. It was also a task at this stage to investigate whether the orientation of the electrode arrangement was a factor to influence recorded signals. To our knowledge, there had been no previous studies implemented a four quarter-arc shape electrode structure close to the single-unit sensor, let along the placement in such compact space. Thus, before further discussion into such an unconventional design, two feasibility questions needed to be answered: 1) Can EEG be bipolarly recorded with electrodes in a close separation of at most 20 mm? This question was the most fundamental one regarding the single-unit sensor design. If we could demonstrate an affirmative answer, then, the second question was whether it was possible to maximize signal energy by orienting the recording electrodes to a particular direction. The feasibility demonstration was conducted through a human subject experiment.

While the feasibility study on the human subject provided experimental evidence on the sensor structure in obtaining EEG, the second goal was to statistically describe the overall performance of the single-unit sensor on whole-brain. A Monte Carlo simulation was performed to compute surface potentials originating from a large number of randomly generated dipolar sources within a statistically modeling of the brain. The numerical source-potential relationship

was established through a forward computing algorithm. The simulation also managed to yield a comparative analysis between the single-unit sensor and a standard 10-20 system. These results of the simulation were interpreted as multi-variable probability density functions. The deterministic equations to describe these probability density distributions were then derived, which provided rigorous analytical insights into the study of the single-unit sensor.

With the first two goals being completed, the third goal was to build a single-unit sensor prototype, which included the construction of an electrode structure and the development of an electronics hardware. The single-unit sensor is cylindrically shaped with a diameter similar to the U.S. Dime. The electrode structure encloses four arc-shape skin-screw electrode-pieces with minimal separation between adjacent electrodes. Among four electrodes, two at opposite locations are configured as bipolar inputs, while the other two connects to the mutual bias channel to suppress common-mode signals. The power-optimized hardware features a 24-bit analog front-end for EEG measurement, an 8-bit RISC microprocessor (MCU), a Bluetooth low energy (LE) module, a dynamic switch, and a power management circuit that regulate raw battery power to various regulated voltage values for digital and analog modules in the system.

The final goal was to test the efficacy of single-unit sensor in collecting EEG and epileptic signal. Another human subject experiment was conducted using the constructed sensor prototype. EEG signals were recorded during human subject's eyes open, eyes closure, and eyes blink. Waveforms with distinct time-domain and frequency-domain features were observed. We then carried out an indirect comparison to test sensor's efficacy in collecting epilepsy. This demonstration established the same geometric scale between the single-unit sensor EEG signal and a 128-channel EEG data utilizing standard 10-10 mapping. The approach proved that the

bipolar recording setup similar to the single-unit sensor and the EEG system employing the 10-20 system produced similar observable features.

### **1.3 CONTRIBUTION OF THE WORK**

This dissertation presents a miniature EEG sensor that is leadless, self-contained with four electrodes, and free-of-gel. The sensor enables rapid and convenient setup of EEG monitoring, which is particularly suitable to critically ill patients in emergency and point-of-care applications.

To be specific, the major contributions of the dissertation are:

- The derivation of a probabilistic model describing the analytical relationship between the dipolar source distribution within a multilayer spherical volume conductor and the potential distribution observed from the scalp.
- The investigation of a novel EEG electrode structure for rapid EEG attachment and capturing.
- The design and implementation of an electronic system specifically for the single-unit sensor.
- The indirect efficacy demonstration of the single-unit sensor prototype in detecting epileptic signal from a clinical EEG data.
- Provide a single-unit sensor design.

To summarize, this dissertation presents the investigation of the single-unit EEG sensor using statistical, analytical, and experimental approaches. With such device, the EEG can be monitored rapidly and continuously at the site of care in emergency medicine.

## **1.4 OUTLINE OF THE DISSERTATION**

This dissertation is presented in eight chapters including the previous introductory chapter:

Chapter 2.0 is a brief literature review on neurological disorders in emergency care, EEG, EEG systems, and a skin-screw electrode technology utilized in this work.

Chapter 3.0 presents the proposed single-unit sensor. The practical advantages associated with the sensor have been explained.

Chapter 4.0 demonstrates a feasibility investigation on closely spaced electrodes similar to the single-unit sensor electrode structure in collecting EEG signals. The experiments were carried out on both a physical model and a human subject.

In Chapter 5.0, a fast computing algorithm was utilized to compute surface potential relating to the dipole source within a multi-shell spherical volume conductor model. A Monte Carlo simulation was employed utilizing this algorithm to quantitatively studied to predict all possible recorded values. Furthermore, a probabilistic model in the form of a multi-variant probability density function was derived, which relates the average signal strength on the scalp in response to the strength of cortical sources using a statistically modeled human brain.

Chapter 6.0 explains the hardware design of the single-unit sensor. We developed a low-power, low-noise, and Bluetooth-enabled electronic system specifically for the sensor.

Chapter 7.0 presents human subject experiment utilizing the single-unit sensor prototypes. Then, the chapter presents the efficacy demonstration on the single-unit sensor in detecting epileptic signals. The demonstration was carried out indirectly based on an epileptic data recorded using the standard 10-20 system.

Chapter 8.0 summarizes the work and provides author's suggestions for future extensions regarding the development of the single-unit sensor.

## **2.0 BACKGROUND**

### **2.1 NCS AND NCSE IN EMERGENCY CARE**

NCS and NCSE are devastating neurological disorders. NCS is the electrographic seizure activity accompanied by impaired consciousness, with a duration longer than 10 seconds. The associated clinical signs are minimal or none. The occasional subtle clinical manifestations include eye deviation, nystagmus, and face myoclonus [15]. NCSE is the prolonged NCS (usually with longer than 30 minutes of duration), along with either 1) continuous seizure activity or 2) multiple seizures in series (often two or more) without complete recovery of consciousness in between seizures [16].

Currently, the majority of the seizures reported in comatose critically ill patients in ICUs and EDs are NCS and NCSE (NCS 75% [17], NCSE 39% [18]), with higher prevalence in children [9] and elderly [19]. At least 8% of comatose cases in ICUs are involved with NCS/NCSE. The occurrences of NCS/NCSE are also associated with frequent conditions including coma and epilepsy as listed earlier. Then, the total incidents of NCS and NCSE in ICUs would reach above 20% of the whole critically ill patients' population.

Critically ill patients in ICUs and EDs are often in comatose, sedated, or paralyzed conditions. The detection of NCS/NCSE can be particularly challenging in these patients as the physical communication pathways between them and surrounding environments are blocked. To date, the neurological conditions in ICUs and EDs are assessed primarily using clinical bedside observations. Some use the "neurochecks" [10], which are series of procedures to manually check patient's neurological status through apparent clinical manifestations (e.g., nystagmus, pupillarity abnormalities). Although these set of manual methods have been utilized extensively, they could

be problematic in some circumstances. For example, evaluation standards are subjective across physicians and observations are intermittent. Patients' therapeutic drug dosage and superimposed neurological deficits easily interfere with the observations. There might be hours before an apparent manifestation of a clinical onset can be observed. As a result, physicians' diagnosis of NCS/NCSE might be either absent or delayed. Too often the problem can only be confronted after the clinical onset, not to mention these observations rarely reveal the underlying mechanisms of NCS/NCSE, including pathological triggers and duration. For example, a study by Jordan *et al.* [20] investigated into the delay intervals to diagnose NCSE due to lack of EEG. The study focused on 30 patients with NCSE transporting into ED from paramedic ambulance. They concluded that the average delay to diagnose NCSE was 153.8 minutes. The misdiagnoses to other conditions including stroke and transient ischemic attack caused most of the delay.

Without timely, rigorous, and continuous means of observation tools, the delayed or absence of diagnosis to NCS/NCSE is a significant factor to add mortality and morbidity in ICUs and EDs. For instance, a study by Young *et al.* [2] demonstrated a mortality of 36% if the NCSE was diagnosed within 30 minutes of onset, whereas the rate nearly doubled to 75% when the diagnoses were delayed over 24 hours. More literature demonstrated that unidentified, delayed diagnosis or delayed treatment caused added mortality [21], and prolonged morbidity [22, 23].

The morbidity and mortality also contribute to increased financial burdens [24]. We haven't found a report to analyze explicitly the expenses for NCS/NCSE management, but a tangible cost could be derived. The annual direct cost of status epilepticus (SE) inpatient admissions [25] was 4 billion dollars, NCSE contributes more than a fifth to nearly a quarter of SE [26] would cost more than 800 million dollars. This cost was solely for the annual direct price of NCSE inpatient admission, which did not take into account a majority of other direct and

indirect costs. Additional costs included repetitive ambulance calls, and either reentry of or extended stay at ICUs. A retrospective cohort analysis by Dasta *et al.* [24] reported that the average daily cost associated with ICU stay was \$7,728 for the first day, \$3,872 for day two, and \$3,436 from the third day. If considering the numbers from Litt *et al.* [19] that NCSE caused on average 17 days of prolonged ICU stay, the cost would be considered extensively higher. Notice that this financial effort was only a mild portion of the entire medical care process, aside from costs of surgery, rehabilitation, and some other indirect costs. Laccheo *et al.* [22] also studied the extended hospital stay due to NCS/NCSE. The study summarized that the median duration for the total ICU stay was ten days for NCS/NCSE patient group, and seven days for patients without NCS/NCSE, that was three more days for NCS/NCSE. The duration of the total hospital stay was 12 days for NCS/NCSE patient group, and nine days for patients without NCS/NCSE, that was also three more days for NCS/NCSE. While the difference in days of stay in the study of Laccheo *et al.* [22] might not reach statistical significance, we can never underestimate the cost of each additional day of hospital/ICU stay.

Meanwhile, NCS/NCSE are fully detectable [3, 17, 22], treatable and potentially reversible [4, 5, 10, 27-29] conditions. EEG is considered to be a prime clinical tool to detect NCS/NCSE associated with coma or altered mental status (AMS) in critically ill patients in ICUs and EDs. In several previous clinical studies, EEG demonstrated efficiency when detecting NCS and NCSE [29]. For example, according to an ICU study carried out by Jette *et al.* [17], the detection rate of first NCS/NCSE using EEG was more than 50% within one hour, more than 80% within 24 hours of produces, and reached 100% with further continuous monitoring. In this case of study, the EEG was remarkable than any other brain assessment approach.

## **2.2 ELECTROENCEPHALOGRAPHY (EEG)**

### **2.2.1 History of EEG**

The history of EEG dates back over a century ago. In the year of 1875, English physician Richard Caton reported the first discovery of electrical current of the brain, which he demonstrated on the exposed surface of the gray matter of rabbits and monkeys [30]. This pioneering finding exploited the groundwork for later scientists, who included German psychiatrist Hans Berger [31]. In 1924, Dr. Hans Berger accomplished the world's first recording of the rhythmic electrical activities from a human brain, including the well-known EEG signature waveform, the “alpha waves”, which is in a range of 8 – 13 Hz. He recorded and illustrated the signal in the form of time series plot, which used voltage differences between scalp sites at vertical axis and versus time at horizontal axis. The output was presented as deflections of printing nozzle pins on long paper sheets [32]. Dr. Berger also studied the alteration of EEG patterns in association with the nature of epilepsy. Fischer and Löwenbach in 1934 [33] demonstrated through animals of the first reported epileptiform spikes. The first systematic research on epilepsy was carried out by Gibbs *et al.* in Boston in 1935 [34]. These early explorations established the foundation for many EEG and seizure specific clinical applications since then.

### **2.2.2 Efficacy of EEG**

There are several reasons from neurology perspective to explain why EEG is currently the best available tool to detect epileptic seizure activities [35-38].



- 1) EEG provides the uttermost millisecond scale resolution. EEG measures the electrical potential on scalp surface originating from rhythmic neuron activities within the cerebral cortex [39]. The changes of neuron activities within the cortex are on the order of the millisecond. The millisecond scale resolution is one of the highest among current major neuroimaging techniques (e.g., fMRI, PET, and CT).
- 2) While achieving the excellent temporal resolution, high channel-count EEG also retains a reasonable spatial resolution (e.g., 128 [35], 256 [40], and up to more than 300 electrodes [41]).
- 3) EEG provides therapeutically important insights into hypoxia and ischemia at the reversible stage [10]. The clustered neurons are distributed in six layers of the cerebral cortex. EEG activity is generated and summed mainly from large cortical pyramidal neurons in the third and fifth layer [39, 42]. Some of these neurons are vulnerable to hypoxia and ischemia. Therefore, the EEG monitoring can find cerebral injuries and neuronal dysfunctions at an earlier stage, when no obvious clinical manifestations could be observed.
- 4) EEG serves as a bedside diagnostic tool for seizure in emergency and point-of-care [34]. While the magnetoencephalography (MEG) also provides millisecond scale temporal resolution, it is not practically available at the bedside. EEG, on the other side, can be available at every bedside, which instantly opens a unique and vital window to observe patient's neurological functions.
- 5) The continuous EEG can monitor the brain for an extended period. A prolonged duration (typically longer than 30 minutes, up to days and weeks) of EEG, the continuous EEG, is often utilized when monitoring disorders such as NCS and NCSE,

rather than routine and intermitted neuroimaging tools. For instance, a clinical study in critically ill children [9] suggested that while 52% of the children have seizure detected within the first hour of EEG management, the detection rate increased to 87% with the continuous EEG within 24 hours. Another study of 110 patients (nine convulsive seizures and 101 non-convulsive seizures) [3] suggested that while the detection of seizure was 56% within the first hour, the detection rate increased to 88% within 24 hours.

The merits above have enabled the EEG to be a rigorous detection method for systematic disorders affecting brain neurological system. It is particularly valuable to potentially identify and segment the primary focus of a pathological condition from propagation areas [35]. For instance, in a study involving 32 patients, 128-channel EEG source imaging localized the focal epileptogenic area accurately in 30 patients (93.7%) [35]. EEG provides direct and early evidence of thalamocortical epileptogenic process at a reversible stage when no clinical indication can be identified [2, 7, 35]. In clinical studies where EEG has been considered, 81% of the decisions on monitored patients were impacted by EEG [29]. These merits also make EEG the most suitable tool for NCS and NCSE in critically ill patients [2, 3, 7, 8, 29].

### **2.2.3 Review of EEG Systems**

Acquiring high fidelity EEG is essential for clinical monitoring, as the quality of signal pivots the outcome of the diagnosis. Three essential blocks of a clinical EEG system are: a) electrodes to sense the scalp potential; b) data acquisition machine to condition, amplify, filter, and digitize the signal; and c) a reviewing device (e.g., a PC or a mobile device) to enable data-hosting, visualization, analysis, and real-time control (RTC) of the hardware.

From the context of electrochemistry, the electrode is a metal conductor that governs electrical transportation to make an oxidation reaction when the electrode acts as a cathode and to make a reduction reaction when the electrode serves as an anode. During the application of cup electrodes to the scalp, it is necessary to fill a certain amount of electrolyte (e.g., collodion) between the electrode and scalp. The electrochemical reaction happens at the interface with electrolyte, which makes the electrolyte the transportation media for ionic current generated within the brain to the electrode. These ionic currents are transduced into electric current by the charge transfer interaction between electrode, body, and electrolyte in contact [43]. Then, a chemical reaction occurs within the compound during charge transfer to conduct electrical current. The weak electric current is sensed and picked up by the electrode, subsequently enters the electronic instrumentation to be amplified. When the electrode is in contact with ions generated from the scalp and transduced by the electrolyte, there is a charge transfer, which causes the neutrality to be changed. The uneven distribution of cations (positively charged ions) and anions (negatively charged ions) create a potential difference, which is the half-cell potential.

Most clinical EEG electrodes are the gold cup electrode (also called disc electrode) made from copper or silver chloride materials [44]. This non-invasive electrode is a 10-mm-diameter thin round metal plate having a 1-mm-diameter hole in the center, with a lead to connect the amplifier. The gold cup electrode forms a groove shape to accumulate EEG paste better. In some occasions during attachment, hair removal is needed to ensure better contact quality from the electrode to the scalp. With skin preparation, the impedance associated with cup electrodes can be as low as approximately 5 to 10 k $\Omega$  [44-48]. The reasonable conductivity of gold cup electrode is partly due to the material's electron compatibility with scalp electrical current flow, which consists electric ions including Na<sup>+</sup>, K<sup>+</sup>, Ca<sup>++</sup>, and Cl<sup>-</sup> [49]. The ingredients of electrolyte usually include

sodium chloride as one of the major components as well. Sodium chloride (salt) is a water-soluble salt capable of carrying large concentration of ions, which makes the chemical compound a good conductor. The cup electrodes made of silver chloride provides a low half-cell potential.

The 10-20 mapping was developed by H. H. Jasper to standardize interpretation and ensure reproducibility of EEG diagnostic results. It was then recognized and popularized by International Federation of EEG Societies in 1958 [50]. The 10-20 mapping describes the electrode sites by relative proportional distances in percentage between cranial landmarks on scalp surface. Specifically, the numbers “10” and “20” illustrates the proportionate distance in percentage between neighboring electrodes, which are either 10% or 20% of between two ears on left and right, or frontal nasion (midpoint between forehead and nose) and posterior inion (central bottom of occipital protuberance). To adequately cover all regions of the brain, electrode locations are labeled with a letter abbreviation depicting brain areas as shown in Table 1. The number after the letter abbreviation denote specific channel.

**Table 1.** Letter indications of placement sites in 10-20 system

| <b>Letter Abbreviation</b> | <b>Location on the Head</b>                          |
|----------------------------|--|
| C                          | Central Lobe   |
| F                          | Frontal Lobe   |
| O                          | Occipital Lobe                                       |
| P                          | Parietal Lobe  |
| T                          | Temporal Lobe  |
| Cz                         | Electrode placed on the crisscross of two mid-lines  |
| FC                         | Electrode sites between Frontal and Central Lobe     |
| FP                         | Frontal Pole   |
| PO                         | Electrode sites between Parietal and Occipital Lobes |

The original standard 10-20 mapping includes about 21 standard positions, which results in average inter-electrode distance to be approximately 6 cm [51]. The spatial sampling with this electrode spacing might not be sufficient enough for some applications needing more details and accuracy (e.g., ERP research). Thus, the 10-20 system has been further spread to 10-10 system [52] and 10-05 system [53] by supplementing electrode sites between the spaces in 10-20 system.

The full functional systems include amplifier, electrode jack box, EEG controller, isolated power supply, acquisition computer, monitoring screen, video camera, and data transmission module. The system sometimes is implemented into a workstation form, which is designed with a base of rolling wheels for mobility, and stacked by a multi-layer shelve on top to load equipment.

An example of clinically used EEG system is Natus Xltek LTM. The system is designed for long-term clinical monitoring of scalp and intracranial EEG. The system provides up to 256 channels according to the standard 10-20 mapping. Its low-noise quantum amplifiers offer up to 16 kHz sampling frequency, 16-bit resolution, and wide bandwidth. At the same time, it enables simultaneous HD video stream. Clinical applications require high sampling of raw data with large data packets, and therefore the system uses wired Transmission Control Protocol (TCP) or Internet Protocol (IP) to transfer raw data to a remote Microsoft SQL server. The system works with various forms of electrodes supporting its data ports, including surface and intracranial electrodes.

There are software tools to display various data in real time, which include the raw time series, filter settings, impedance status, and simultaneous video recording. Other techniques to visualize raw data have been utilized, including quantitative EEG (qEEG) technique employing frequency analysis, and probability mapping. Sensitive changes of colors on the topographic map is helpful for visual inspection, especially for some lesions that are too subtle to show on raw EEG traces [54, 55]. The qEEG display types include the compressed spectral array (CSA), brain

electrical activity mapping (BEAM) [57], cerebral function monitor (CFM), and topographic brain mapping (TBM).

#### **2.2.4 Practical Barriers to Adopt EEG in Emergency Care**

Nowadays, only two percent of emergency departments are equipped with EEG, apparently short of demand [10]. The under-adoption of EEG is because performing high-quality EEG sessions in emergency represents major challenges in procedural, logistical, and financial aspects [15]. For example, one of the challenges is to accommodate EEG system to current ICUs and EDs. Unlike in the neurological intensive care units (Neuro-ICUs) and epilepsy monitoring unit (EMUs) where EEG can be prioritized, the EEG in a general ICU has to be arranged among existing protocols and devices. Under this circumstance, the interferences generated by human and equipment might influence the operation of EEG systems, as EEG amplitude is weak compared to the competing environmental noise and interferences. The undesired source of signals, including ambient noises and motion artifacts, some with magnitudes of several orders higher than EEG is presented during the recording, which could be picked up by the electrodes. For example, the magnetic and electric field interference generated by alternating current (AC) contributes to a major source. The power line interference induces frequencies including 50 Hz and 60 Hz. Besides, the electrode leads, body, and amplifier circuit form a conductive loop. According to Faraday's law [56], the AC generated magnetic field can induce electromotive force (EMF) within the loop, which results in AC potential. A study from Huhta and Webster [57] illustrated that the area of conductive loop was almost in a linear relationship with AC potential, with  $120 \mu\text{V}/\text{m}^2$  loop areas. The friction and deformation of electrode leads caused signal attenuation to add linearly to the signal into the

amplifier input. This AC potential introduced to the EEG system contaminated the recorded signal. Besides, sources such as thermal, triboelectricity and bio-potential could interfere with EEG.

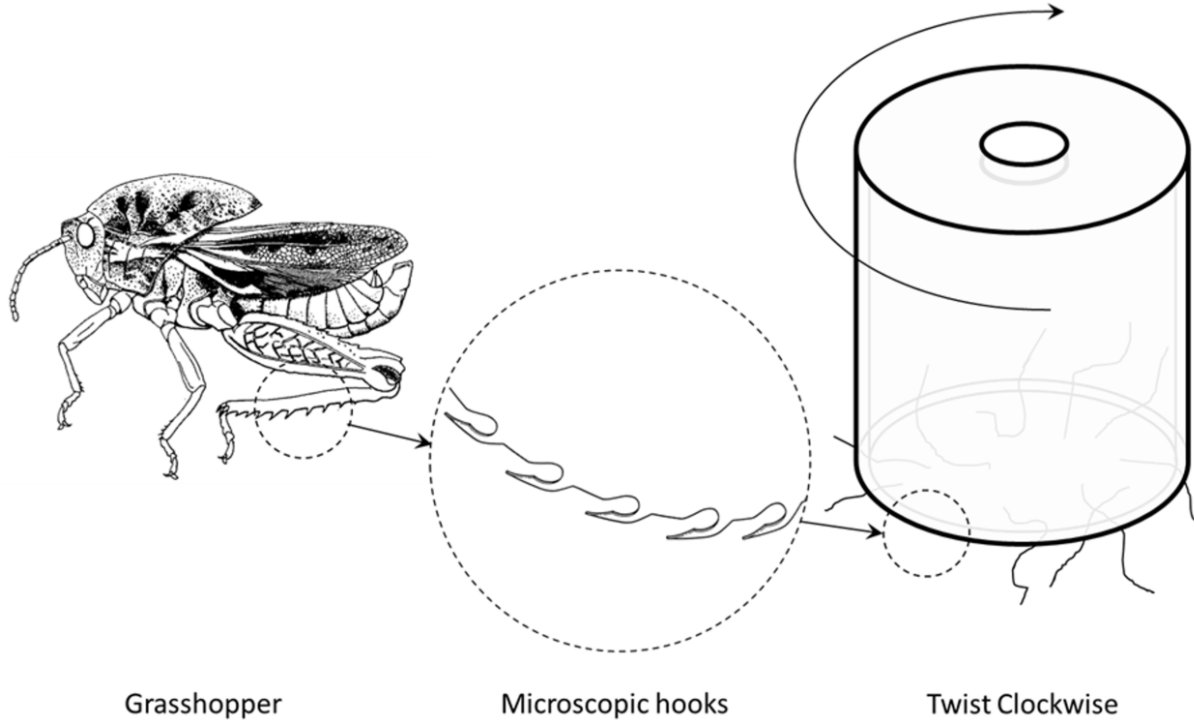
The setup procedures for traditional EEG system is time-consuming, and it represents a challenge to arrange a time for an EEG preparation in parallel with other currently established procedures. The typical setup time for the standard 10-20 EEG is 20 – 45 minutes, during which the physicians can continue very limited procedures simultaneously. The preparation procedures are tedious, uncomfortable or even painful. Skin abrasion is needed at each site using chemical compounds and cotton swabs to remove stratum corneum, the high-impedance skin layer. Occasionally, hair removal is required to secure fixation or improve contact. Once skin abrasion is done, conductive EEG paste (e.g., collodion, a flammable nitrocellulose and ether compound) is applied to individual electrodes to allow it to be securely fixed onto the recording site. The procedure is messy as the paste is smeared over patient's head. The paste is a water-soluble compound and will gradually either deteriorate due to body heat, air dried due to ventilation, or displaced because of head movement, which will further add excessive motion artifacts and drift potentials entering the amplifier circuit. This issue is amplified during patient's transportation and long-term monitoring. While these traditional EEG systems provide superb signal qualities, their cumbersome and irritating features drastically hinder their use in certain applications, such as point-of-care and emergency medicine. It is doubtful that current procedures can be performed in parallel efficiently with EEG.

### 2.3 SKIN-GRABBING AND GEL-FREE EEG ELECTRODE

A unique design of the single-unit sensor is the arc-shaped electrode with miniaturized hooks on the skin-contacting surface. This biomechanical design originates from the “skin-grabbing and gel-free electrode” developed by Sun *et al.* [58, 59]. In this section, we describe the work briefly. The inventors were inspired by the spectacular ability of the grasshopper to grab and hold objects using sawtooth-shaped spines on its tibia (Figure 1). The sawtooth-shaped spines are on both walking and jumping legs of the grasshopper, which help the insect to thrust against the surface of a plant (e.g., leaf or grass), and endure strong force when launching a jump.

Such biological mechanism is innovated into the skin grabbing electrode as many microscopic hooks on the distal surface of the electrode. The hooks firmly grab the scalp surface the stratum corneum, which is the outer most cornified layer of the epidermis. The stratum corneum has a thickness of 0.02 – 0.7 mm (approximately  $\frac{3}{4}$  of the epidermis) [60], consisting mostly the dead cell membrane due to metabolism. During the metabolism, the inner epidermis layer, containing stratum granulosum, stratum spinosum, and stratum germinativum, generates new skin cells and progressively pushes dead cells to the skin surface. The cells remain in stratum corneum for certain period. The stratum corneum acts as a natural barrier to resist pathogen, bacteria, and water loss, but at the same time, the dead cell membranes in stratum corneum are more impermeable (approximately 50 k $\Omega$  with one square millimeter of skin [61]), which is a major barrier against the transfer of ions. The dead cells in stratum corneum contribute to high impedance and are usually abraded or hydrated to achieve a lower impedance.

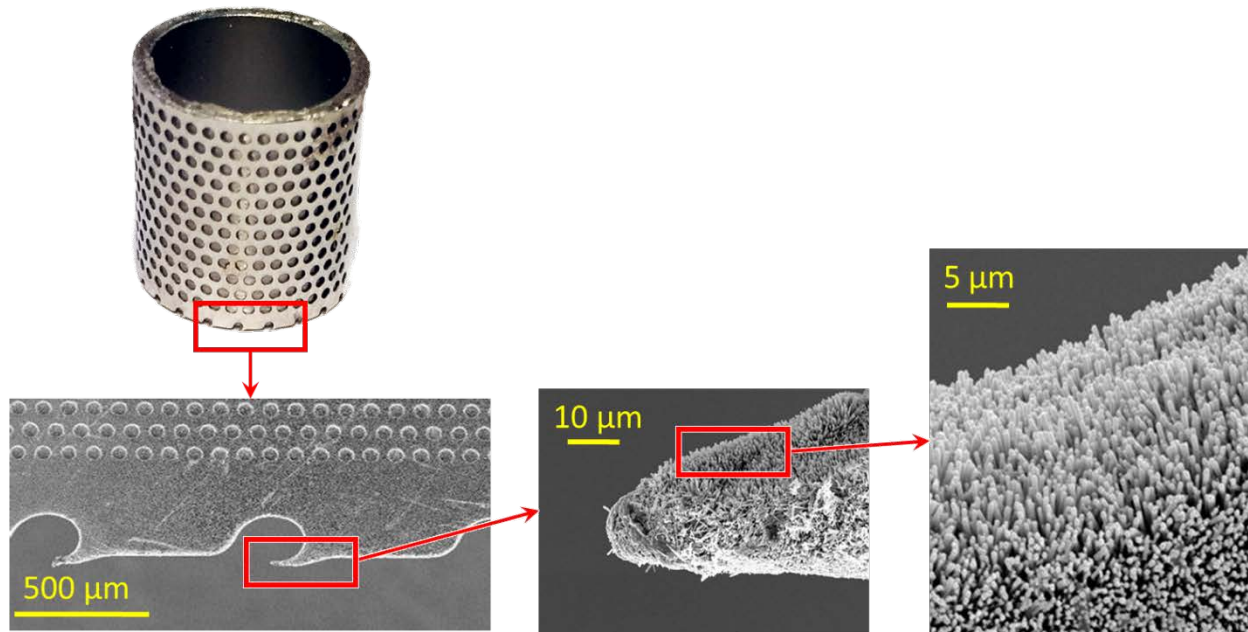




**Figure 1.** Schematic of the teeth structure on the skin-screw electrode. The microscopic teeth design was inspired by spine structure on grasshopper's leg. The grasshopper sketch is adapted from [62] (© 1962 Entomological Society of South Africa (ESSA)).

By implementing the microscopic teeth on the skin-grabbing electrode, the teeth purposefully penetrate through the thin layer of stratum corneum to firmly grab the skin. A secure fixation is formed without the need for any adhesive paste. Furthermore, the teeth penetrate through high-impedance stratum corneum layer to make a steady electrical connection with scalp at a lower impedance, which saves the effort of using skin preparation gel to rub off skin cells to reduce impedance. With such structure on the electrode, no skin preparation or EEG paste is needed. By merely pressing the electrode against the unprepared scalp and twisting slightly, the electrode can painlessly grab the skin firmly and start to collect EEG.

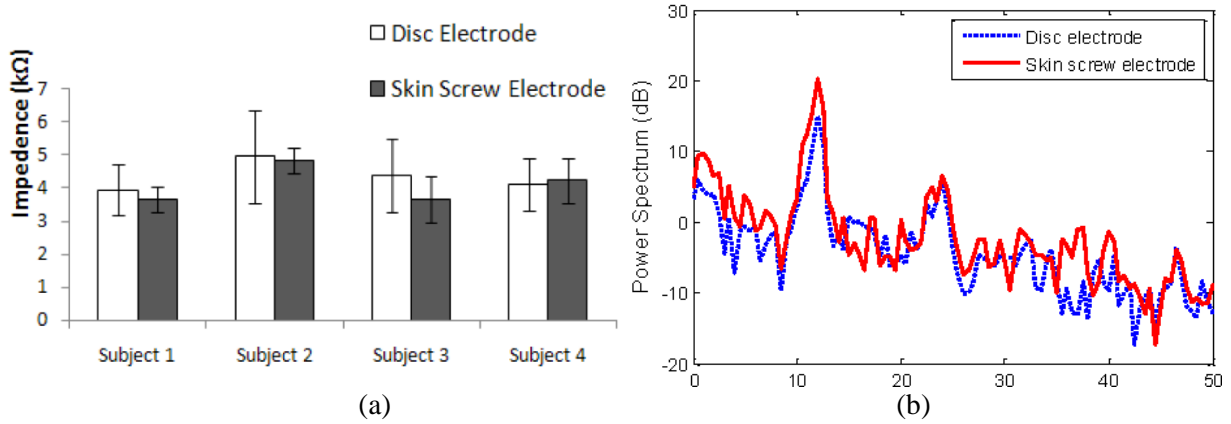
Figure 2 shows an actual skin-screw electrode. The material utilized to construct the electrodes is grade 316L stainless steel, which has desirable mechanical properties, biocompatibility, and complies with the U.S. Food and Drug Administration (FDA) standard. The electrodes are manufactured via photolithography, which produces the microscopic hooks precisely while achieving a very low cost. To further increase contact area to improve conductivity, the surface of the microscopic teeth can be further coated with zinc oxide nanowire protrusions. Zinc oxide is a safe material that has been used to assist healing of wounds on skin and as an additive to food products.



**Figure 2.** An actual skin-screw electrode and the microscopic view of the teeth structure. The teeth are covered by nanowires to increase conductance.

A performance test [58] was executed in terms of impedance, spontaneous and evoked EEG measurement of the skin-grabbing electrode comparing with traditional disc electrode (gold

cup electrode). The student t-test indicated that no significant difference was observed between two types of electrodes (Figure 3 (a)), and the EEG signal recorded by the skin-screw electrode is comparable to the signal recorded by gold cup electrode (Figure 3 (b)).



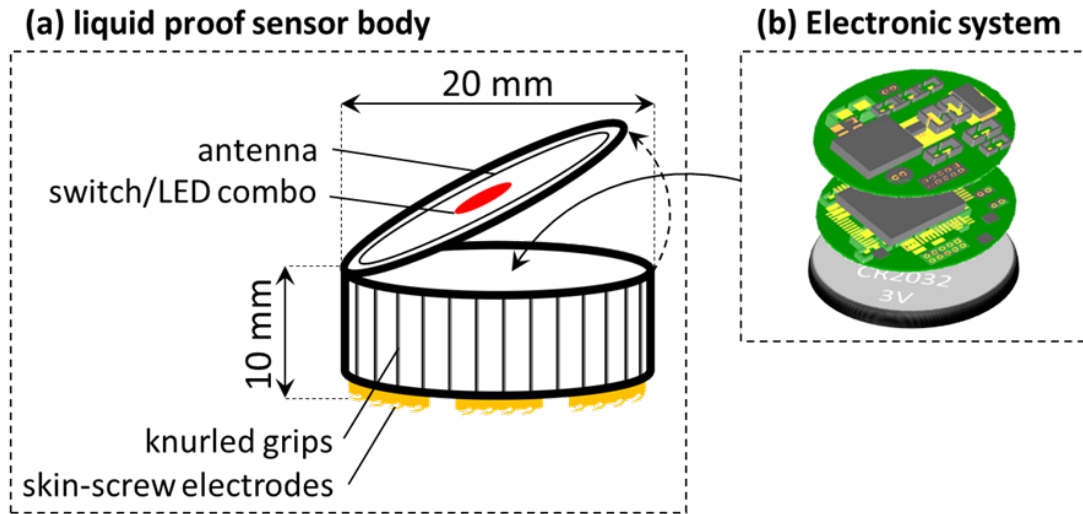
**Figure 3.** Statistical comparison between the disc electrode and the skin-screw electrode. (a) electrode-skin impedance measurement comparison between disk electrode and the skin-screw electrode. (b) The spectra estimated using Welch’s method for traditional disk electrode, and the skin-grabbing electrode. This figure is adapted from [58] (© 2012 IEEE).

Rather than initially used as multiple cylindrically shaped skin-grabbing electrodes to serve as recording electrodes and reference electrodes, in this work, multiple arc-shaped skin-screw electrode pieces were combined into a cylindrically shaped unit, with separation between one arc and another. Next, we describe the details of the proposed sensor in Chapter 3.0.

### 3.0 PROPOSED SYSTEM FOR RAPID EEG MEASUREMENT

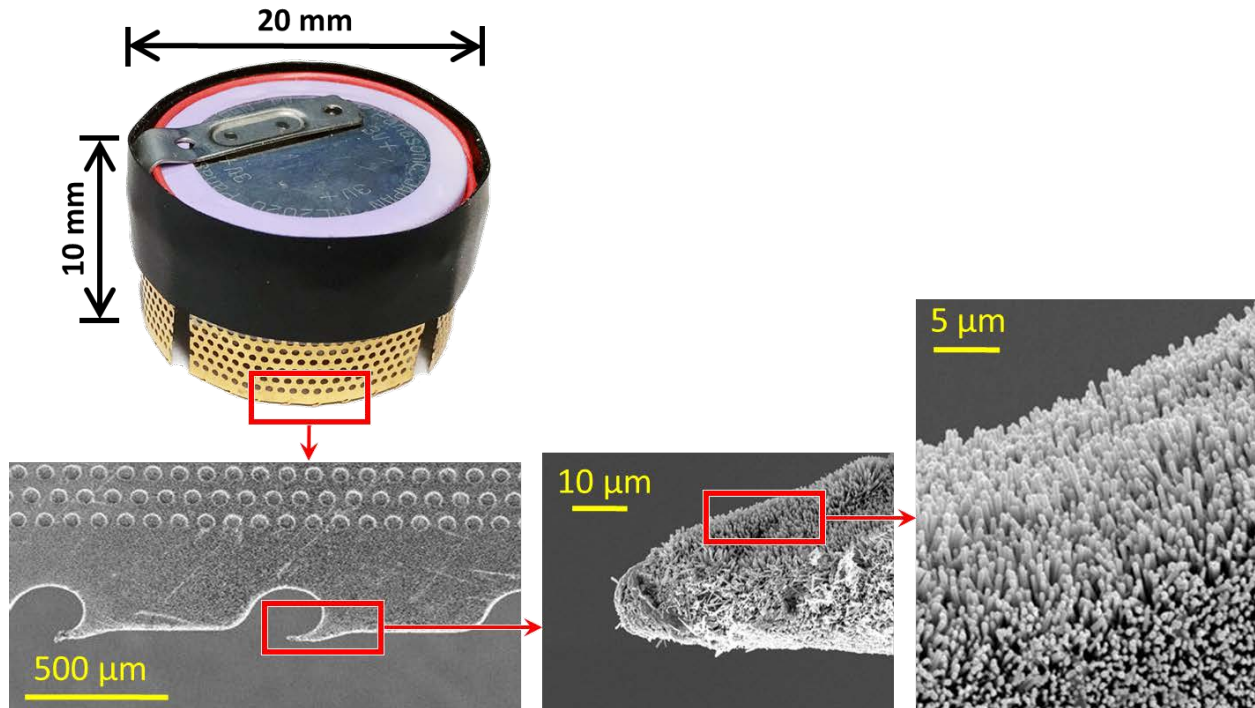
#### 3.1 OVERVIEW OF THE PROPOSED SYSTEM

The envisioned single-unit sensor (depicted in Figure 4) is in the shape of a flat cylinder (approximately 20 mm in diameter as the U.S. dime, and 10 mm in height). The sensor is composed of two essential building blocks: (a) a cylindrical sensor body and (b) a highly integrated electronic system fitted inside the electrode structure. The cylindrical body is assembled by enclosing four thin arc-shaped metal plate electrodes.



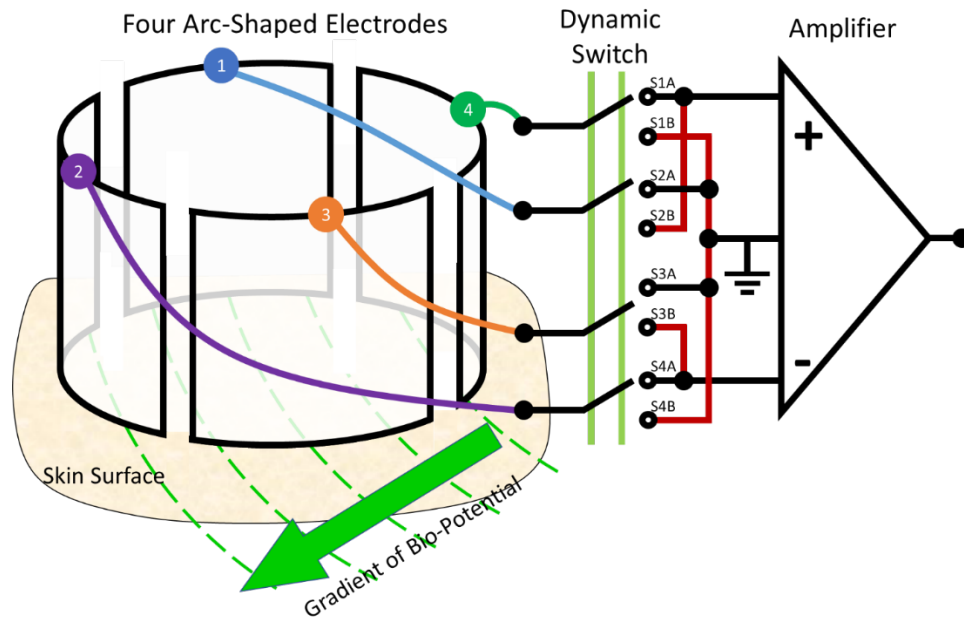
**Figure 4.** Schematic of the single-unit sensor. The building blocks of the sensor include: (a) a sensor body composed of four quarter-arc segments of skin-screw electrodes and (b) a highly integrated electronic system and a coin battery fitted inside the sensor.

In the sensor body structure, the arc length of each electrode plate is 12.5 mm with separation of 3.25 mm in between adjacent electrodes. On average, five microscopic hooks are installed on the distal edge of each plate electrode. The arc-shaped electrode plates are thoroughly coated with gold sputtering to improve electrical conduction. In addition, as is shown in Figure 5, on the distal skin-contacting surface of the electrodes, there are microscopic hooks in micrometer scale wrapped with nanowire protrusions. This unique bio-mechanic design enables the sensor to firmly grasp the stratum corneum, and make a steady electrical connection at a lower impedance. The skin-grabbing design of arc-shaped electrodes originates from the skin-screw electrode [58, 59], which have been previously described in Section 2.3. The packaging of the sensor is finished with rubber in knurled pattern to facilitate secure gripping and twisting.



**Figure 5.** An actual single-unit sensor and the microscopic view of its skin-contacting surface.

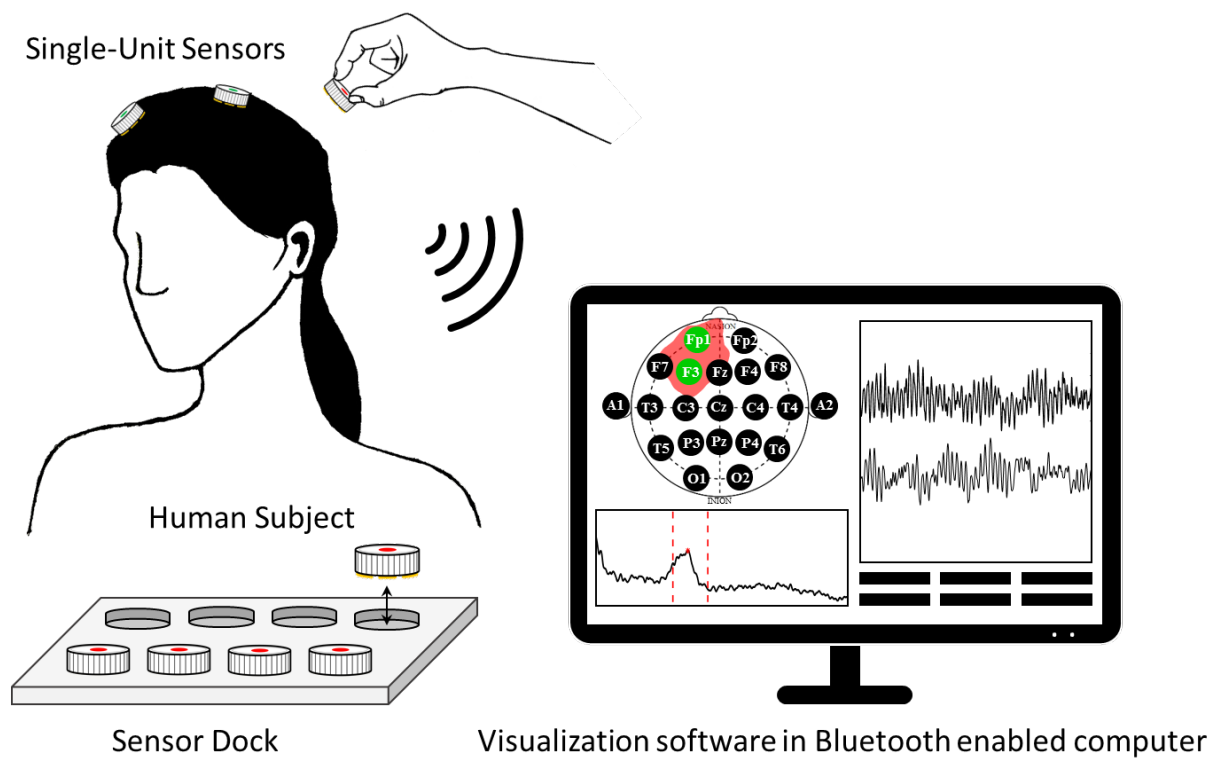
There is a specially developed electronic system fitted inside the hollow sensor body. The electronic system includes four analog switches to switch the orientation of recording electrodes. There is a bio-potential front-end to acquire and digitize EEG signal. The signal is wirelessly transmitted to a remote computer by a Bluetooth module. An MCU manages the operation of switches, EEG signal acquisition, and data transmission. A power management circuitry regulates a battery power supply to multiple voltage levels to power up every module in the electronic system. An LED indicator light on top of the sensor indicates the operation and data transmission status.



**Figure 6.** The operation mechanism of the switches implemented in the single-unit sensor.

The working concept of the single-unit sensor is demonstrated in Figure 7. By merely pressing the sensor against the human subject's unprepared scalp and twisting clockwise slightly, the device firmly grabs the skin and starts to acquire EEG. Notably, the switching feature shifts

the connection of electrodes to either recording or bias channels to the amplifier, thus manage the recording orientations to lie along the gradient of bio-potential. Subsequently, a greater amount of potential among two recording orientations could be selected. The digitized signal then transmits wirelessly to a Bluetooth enabled device. The brain monitoring can be set up rapidly to allow the underlying neurological conditions to be monitored and evaluated instantaneously.



**Figure 7.** The single-unit sensor working concept. The sensors can be rapidly installed onto the unprepared scalp and instantaneously start to acquire EEG signal. The EEG signal is wirelessly transmitted to a Bluetooth enabled computing device (e.g., computer) visualized for further monitoring and analysis.

### 3.2 PRACTICAL BENEFITS OF THE PROPOSED SENSOR

The practical benefits of the proposed single-unit sensor highlights in three aspects. Firstly, the single-unit sensor enables timely EEG setup. The timely EEG setup is a critical feature in emergency medicine because rapid diagnosis and reaction may save a patient's dying brain (as in clinicians' phrase "time is brain" [63]). While traditional EEG preparation procedures regularly consume 20 – 45 minutes of time, the single-unit sensor shortens the preparation time, which opens valuable early timing window to observe epileptic onsets. The brain injuries caused by seizure with may be reversible within a short amount of time immediately after clinical onset [64]. Therefore, early detection increases the chances of reversing conditions.

Secondly, by using bipolar recording montage of adjacent electrodes, the single-unit sensor opens a unique window to let a specific brain region of interest to be studied without the necessity of installing electrodes across a large area or whole brain. The region of interests for certain neurological disorders has been extensively investigated. For the EEG assessment of well-understood conditions, a fewer number of electrodes could speed up the preparation process, which implies the accelerated detection and treatment. For patients with critical conditions like head trauma, the single-unit sensors may also be an alternative to the installation of electrodes on whole-scalp. Another merit of bipolar recordings is that the sharp changes in a small focal area could be well observed. Adjacent electrodes in the sensor-unit sensor have a separation of 3.25 mm, and the opposite electrodes have a separation of 20 mm. This close distance enables a higher density of electrodes placed in the area. This feature ensures a satisfying sensitivity and specificity in the region of interest.

Thirdly, compared to a conventional EEG workstation and its carrying cart with a mass number of electrode leads, the single-unit sensor is leadless and compact due to its distinct design

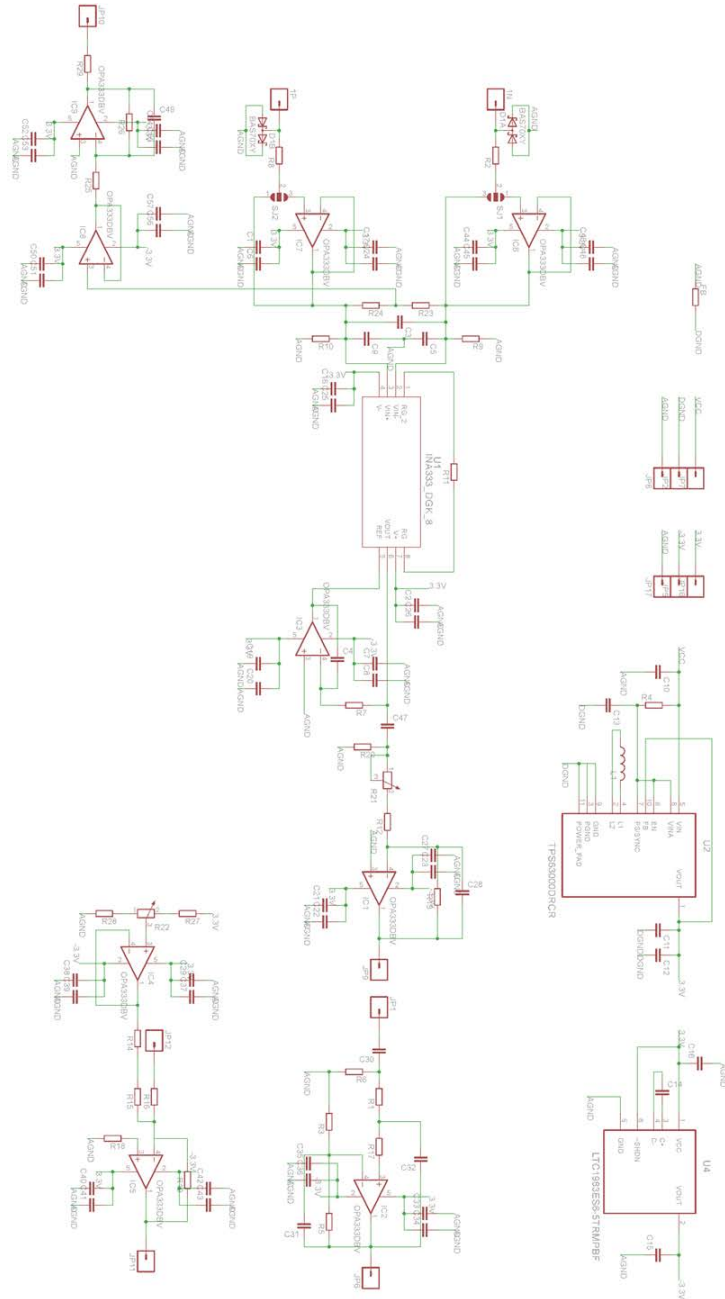


and high integration of functional modules. This advantage makes the accommodation of EEG in ICUs and EDs increasingly practical. The single-unit sensor reduces the interfering length of the period to the established emergency procedures and setups. Other subsequent procedures can be carried out promptly. An increase in efficiency could be expected accordingly. Furthermore, by improving convenience and efficiency, the EEG could be considered as a higher priority among emergency procedures. The improved efficiency further allows EEG to be acquired at the site of emergency care outside of the clinical environment.

The benefits as mentioned above enable a rapid and convenient means of EEG monitoring with fewer labor efforts. If implemented successfully, the solution reduces the hurdles to bring and adopt EEG into ICUs and EDs, which would eventually lead to decreased morbidity, mortality, and financial burden.

## 4.0 FEASIBILITY DEMONSTRATION

### 4.1 AN AMPLIFIER DESIGN FOR FEASIBILITY TESTS



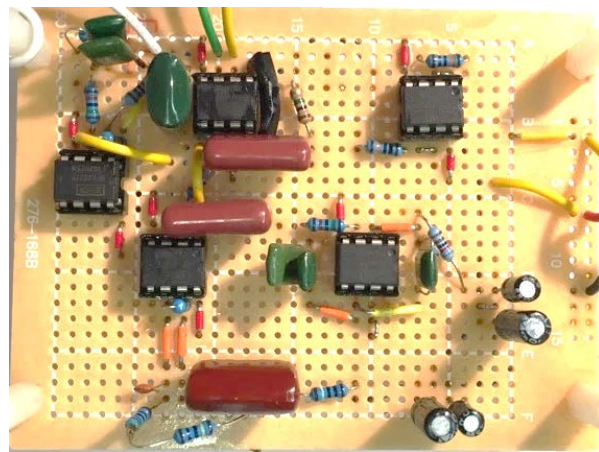
**Figure 8.** Schematic diagram of the EEG amplifier circuitry.

A multi-stage cascaded analog amplifier circuitry was designed and implemented for feasibility experiments (Figure 8). A protection circuit with two-way diodes was designed at the input of the circuitry to ground any large input voltage above 0.7 V. Then, at the first stage of the circuitry, two voltage follower circuits were constructed for an ultra-high input impedance to avoid loading effects to the input signal. This design also isolated the amplifiers from directly connecting to the recording electrodes. At the second stage, a low-power instrumentation amplifier was implemented. The specific choice of instrumentation amplifier was Texas Instruments (TI) INA118, which had an input differential impedance of  $10 \parallel 1$  ( $G\Omega \parallel pF$ ), and a common-mode impedance of  $10 \parallel 4$  ( $G\Omega \parallel pF$ ) [65]. It further offered high precision (50  $\mu V$  maximum offset voltage, 0.5  $\mu V/^{\circ}C$  maximum drift, 5nA maximum input bias current, and 350  $\mu A$  quiescent current [65]). Additionally, it provided common-mode rejection ratio (CMRR) at the minimum of 110 dB. The precision and high CMRR offered by this instrumentation amplifier were critical to our application to suppress half-cell potential from electrodes, as well as to suppress common-mode noise from the environment. The low power consumption property of the instrumentation amplifier was ideal for battery operation. The external resistor  $R_G$  enabled an adjustable amplifier gain. The gain for this stage was set to be six. The first stage gain cannot be too large since the input produces a small differential signal between two input terminals. A large gain would drive the amplifier output to near the supply voltage, which may saturate the amplifier. For example, if a gain of 100 was applied at the first stage, it would increase a 10  $\mu V$  EEG to 1 mV, but would also increase a 500-mV direct current (DC) offset to 50 V.

At the third stage, a negative feedback integrator was implemented. It fed the inverse of DC drift integrated from signal back to the instrumentation amplifier's reference terminal so that the drifting potential was canceled from the input. This design feature allowed the system to

suppress input offset voltage, half-cell potential, and DC drifts. The operational amplifier used for the next-stage amplification was TI TLC277CP, which was configured with a non-inverting design to maintain the same polarity on the output. A potentiometer was installed to allow an adjustable gain. The actual gain obtained was in a range between 5.76 – 101, which could be adjusted to obtain a desired output signal strength within a limited range.

The circuit implemented at the final stage was a second-order Butterworth filter employing the Sallen–Key topology [66]. This filter design allowed the circuitry to amplify the signal while suppresses the frequency components with a sharp cutoff, as well as a wide dynamic range. Our designed cutoff frequency for the low-pass filter was 49 Hz (actual measured cutoff frequency was 49.4 Hz). Therefore, the electromagnetic interference (EMI) from the electrical power system at 60 Hz could be suppressed efficiently. A voltage regulator and an optional level shifter (to interface with an ADC that requires non-negative voltages) was also designed and implemented. The overall gain achieved at this circuit was between 5,000 – 12,000. The actual circuitry is shown in Figure 9. This circuitry was then utilized to acquire actual EEG for the feasibility experiment.

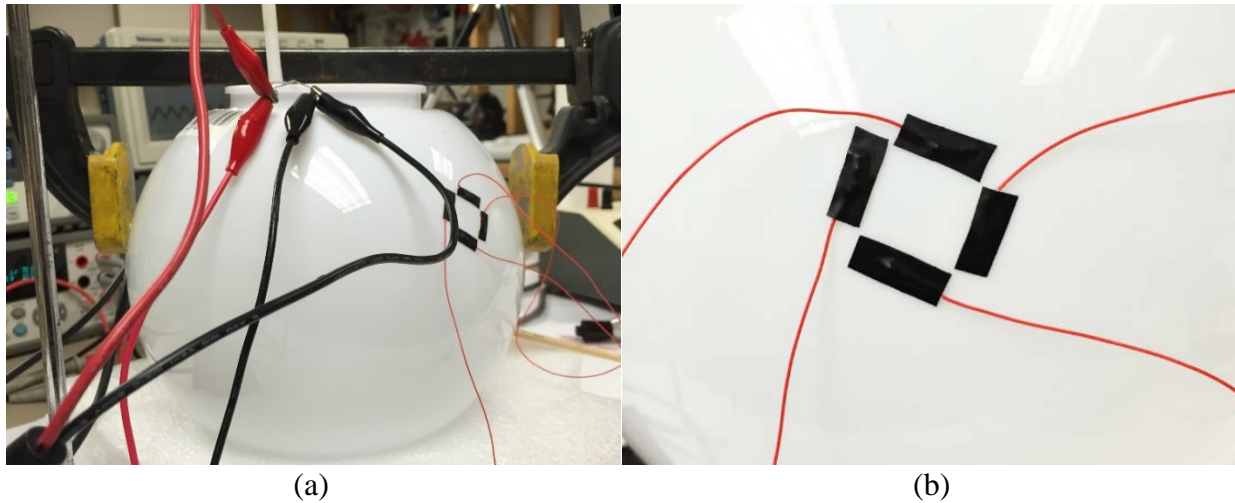


**Figure 9.** Picture of the actual circuitry used for feasibility test. The components were installed and soldered on a through-hole circuit prototyping board.

## 4.2 EXPERIMENT ON PHYSICAL MODELS

### 4.2.1 Experimental Design

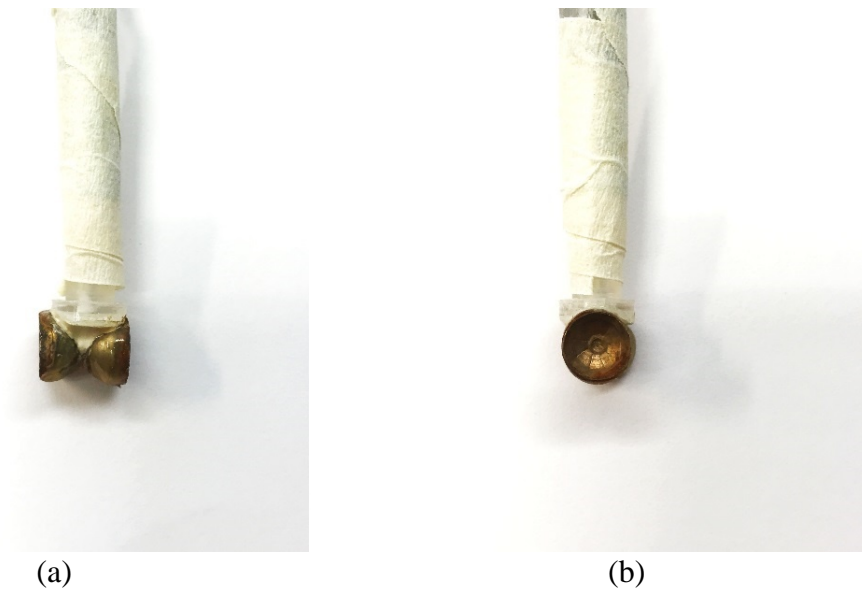
We approached the two feasibility problems by first utilizing a physical model of a plastic sphere (Figure 10 (a)) with dimensions similar to an actual human head. The conducting property of the sphere was achieved by filling saline solution into the hollow center space. After thorough stirring, the conductivity of the salt solution in the sphere was maintained at 0.33 S/m (measured by a YSI Model 35 conductance meter), similar to the average conductivity of human brain reported in the literature [67, 68].



**Figure 10.** The physical models constructed for the experiment. (a) The single-layer spherical volume conductor model. (b) The capacitive electrode plates on the surface of plastic sphere.

The dipolar source model was then constructed using two small copper sinks facing opposite direction separated by an insulator (as shown Figure 11). Once the dipole was dipped into

the saline solution of the volume conductor model and induced an AC signal from the signal generator, an AC field was created within the volume conductor. In order to measure the potential across different locations of the conductor, a capacitive coupling was formed between each electrode on the sphere surface and the saline solution across the thin wall of the spherical container.

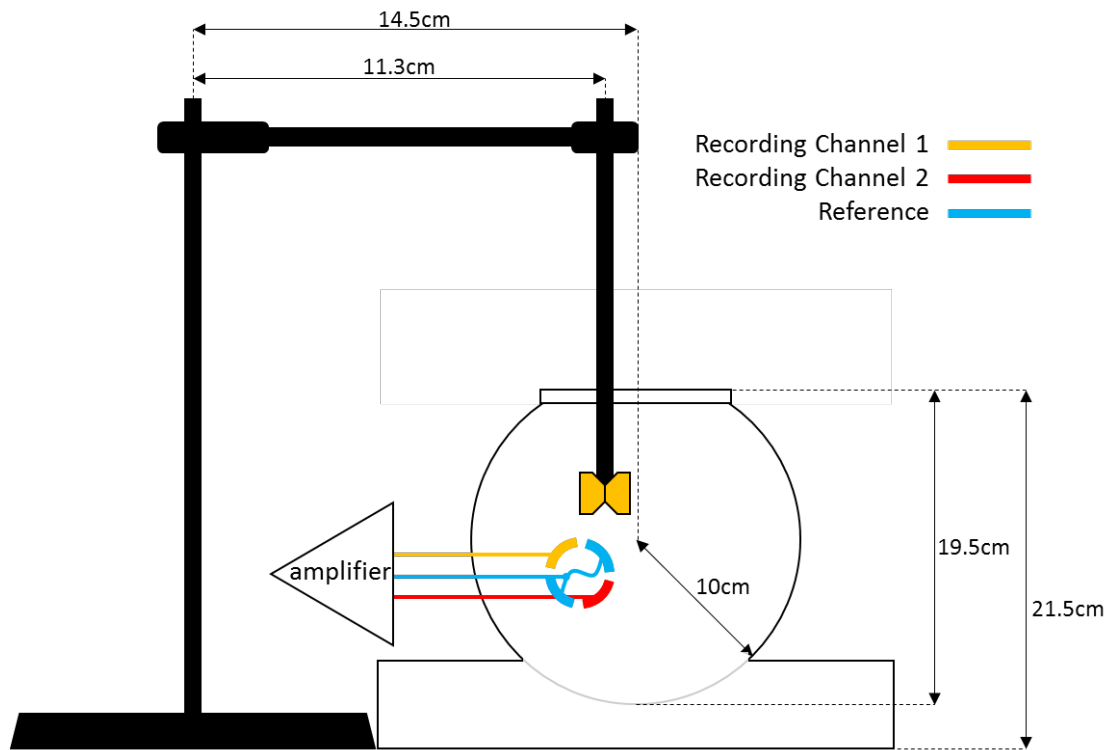


**Figure 11.** The dipolar source model presents in (a) side view and (b) front view.

Four capacitive sensing electrodes were constructed to measure the surface potential of the volume conductor model. Figure 10 (b) depicts the electrodes. Thin copper plates (covered by black tape) with size and placement configuration similar to the design of a single-unit sensor were attached to the surface of the sphere with an approximately 20mm distance between two opposite sensing electrodes.

The schematic of experiment setup is presented in Figure 12. The dimension of each component was precisely measured so that the spatial location and orientation of dipole model

with respect to spherical volume conductor model and surface electrodes could be derived by measuring some of the known parameters. The multi-stage cascaded EEG amplifier circuitry described in Section 4.1 was connected to the surface electrodes to measure the signal induced by the dipolar source inside the sphere.



**Figure 12.** Schematic of the experimental platform.

#### 4.2.2 Verification with Simulation Program

To validate the accuracy of the experiment procedures, the results were compared with a simulation program. A simple homogeneous spherical volume conductor model was utilized to

simulate the generation of electric potential at the surface of volume conductor due to the dipole source inside. Sidman *et al.* [69] reported a mathematic model to determine the surface potential of a unit-radius homogenous volume conductor when the dipole information was known. Assuming the homogeneous sphere had a radius of  $R$  and conductivity of  $\sigma$ , the surface potential was expressed as:

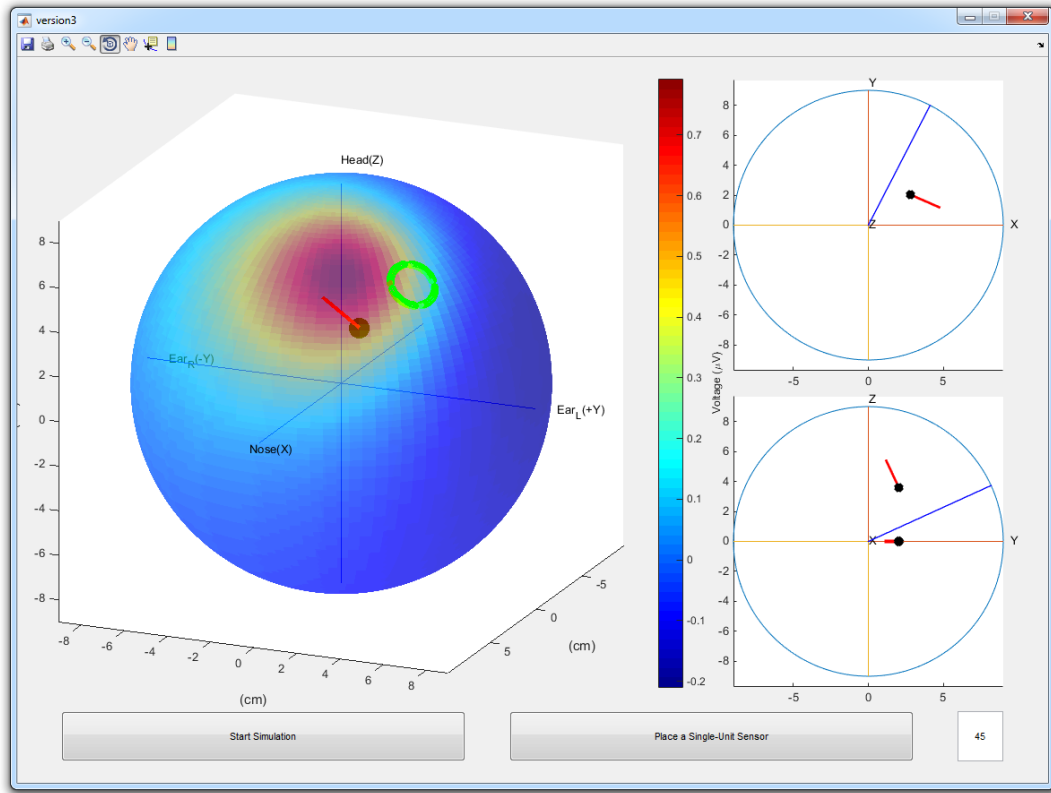
$$\varphi = \frac{1}{4\pi\sigma_1 R^2 q} \sum_{i=1}^3 m_i \left[ \frac{2(e_i - d_i)}{q^2} + e_i + \frac{e_i s - d_i}{q + 1 - s} \right] \quad (1)$$

where  $d_i$ ,  $m_i$ , and  $e_i$  were the vector elements of dipole location vector  $\mathbf{d}$ , current dipole moment  $\mathbf{m}$  and surface point  $\mathbf{e}$ , accordingly. Further,  $q$  was derived as follow:

$$q = |\mathbf{e} - \mathbf{d}| = \left[ \sum_{i=1}^3 (e_i - d_i)^2 \right]^{\frac{1}{2}} \quad (2)$$

A graphic user interface (GUI) in MATLAB software was developed to visualize the simulation model. The interface allowed users to graphically input and choose parameters: dipole location vector, current dipole strength, and the surface points. After inputting these values, Equation (1) was computed using the provided parameters. The result of potential computation on the whole spherical surface is shown in Figure 13. Using a similar method, the potential differences of the single-unit sensor could also be simulated on the surface of the sphere.



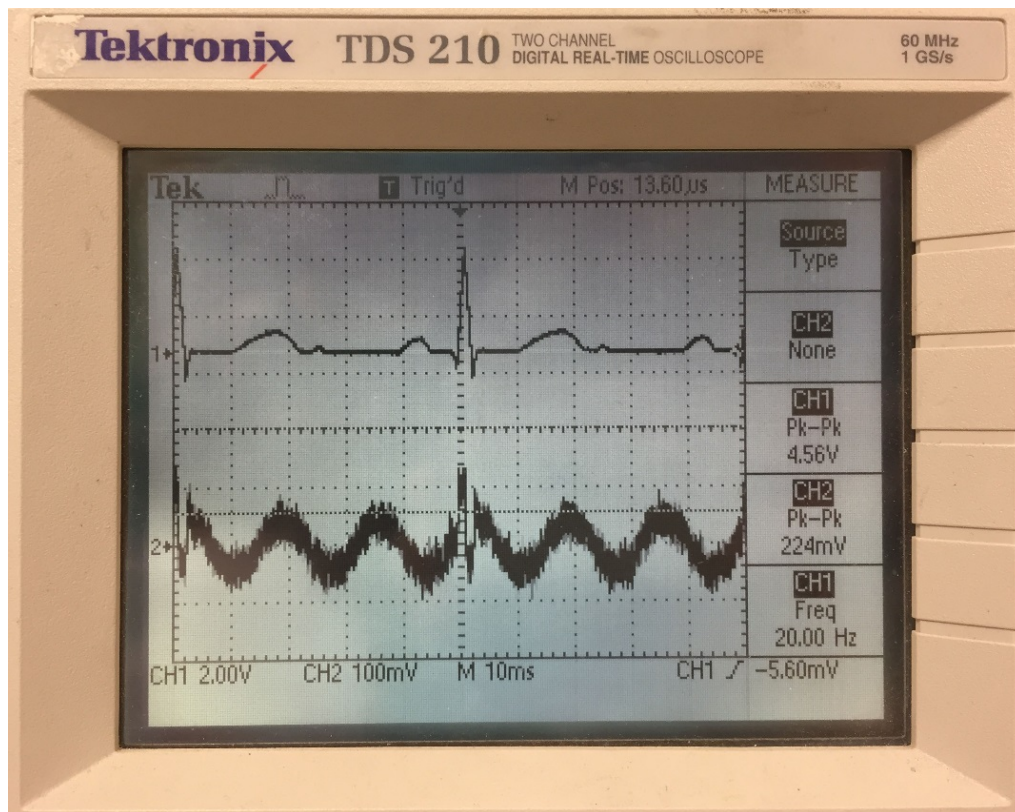


**Figure 13.** The interface of the simulation program. In the left side sphere, the black dot inside represents the dipole. The red line pointing from the black dot to sphere surface represents the dipole moment. The gradient color on the sphere surface represents the potential strength, which the values are indicated in the vertical color bar. The four green arcs on the sphere surface represent four arc electrodes, similar to the electrode configuration of the single-unit sensor. On the right side, the top and bottom circles, respectively, provide the top and side views of the volume conductor model.

### 4.2.3 Experimental Results

Figure 14 shows the dipole induced signal at the top and the surface electrode measured signal at the bottom. Particularly, a simulated cardiac signal with amplitude of 2 V peak-to-peak voltage and a frequency of 20 Hz was generated and induced by the dipolar source model. The actual

measured signal from the surface of the sphere model when the dipole was excited had an amplitude of 100 mV, and same frequency as to the input. Although the output signal measured by surface capacitive electrodes was observed, the signal strength reduced by a factor of 20, while generating large background noise.

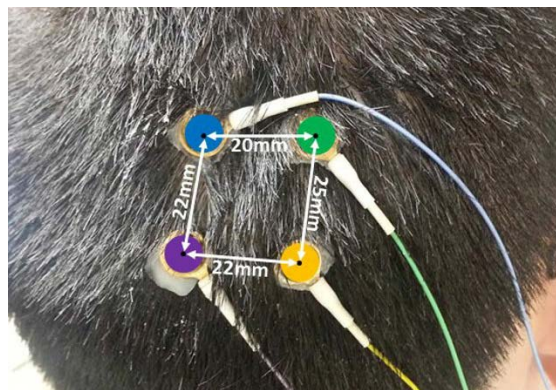


**Figure 14.** The acquired signal from the physical model. The input signal to the dipole is presented at the top, and the acquired signal from surface electrodes is presented at the bottom.

## 4.3 EXPERIMENT ON HUMAN SUBJECT

### 4.3.1 Experimental Design

The feasibility problems were then approached by conducting experiments on an actual human subject. Four standard gold cup electrodes were installed on the scalp of the male, healthy subject. The actual inter-distances of the electrodes were measured to be 20, 22, 22 and 25 mm, respectively. The setup of four electrodes are seen in Figure 15. The electrodes were color-coded for easy identification. There were six ways to connect these electrodes as described previously. In any of these connections, two electrodes were connected to the pair of signal inputs of a differential amplifier, and the rest two electrodes were tied together and connected to the analog ground of the same amplifier. The EEG data were acquired using the amplifier circuit described in Section 4.1. The LabVIEW 2010 software from National Instruments (NI) was used to record data at a sampling rate of 500 Hz with 16-bit resolution. The software was able to display the recorded EEG signal in real-time and to save the raw data for further processing.



**Figure 15.** Four gold cup electrodes were installed closely at the occipital region of the scalp. This figure is adapted from our publication [70] (© 2014 IEEE).

To verify that true EEG was recorded, a signature EEG signal had to be identified. We approached this problem by focusing on the alpha wave in the EEG [8]. This waveform has been known to be closely associated with human alertness and wakefulness. It emerges into a strong rhythm when the subject is relaxed with eyes closed, and almost disappears when the human subject becomes alert with eyes open. For most people, the frequencies of the alpha wave are in the range of 8 – 13 Hz [9]. These valuable properties enabled us to use the alpha wave as a signature signal to study the presence of the EEG and compare its energy value among different electrode orientations.

#### **4.3.2 Statistical Analysis**

The simple but effective spectral analysis was used to process raw data. We divided each data, which was sampled at 500 Hz, into five-second segments (2,500 data points). The number of segments divided depends on the length of data. In order to suppress spectral leakage, the Hamming window with five-second length was applied to each segment, and the discrete Fourier transform (DFT) was computed for each windowed segment padded with zeros so that the length of the DFT was 4,096. The energy value of alpha band, which was defined by the magnitude squared of DFT within 8 – 13 Hz, was calculated for each segment to study the effect of electrode orientation.

In each five-second segment, an energy value for the alpha band was computed from DFT result. Therefore, for each electrode orientation, we were able to compute a set of energy values for all segments of data. We performed such analysis for all cases of electrode orientations. In total, six sets of energy values were computed. The null hypothesis was that the energy values of

six sets of data acquired using different electrode orientations were indifferent. The standard one-way analysis of variance (ANOVA) was utilized to test the null hypothesis.

### **4.3.3 Experimental Results**

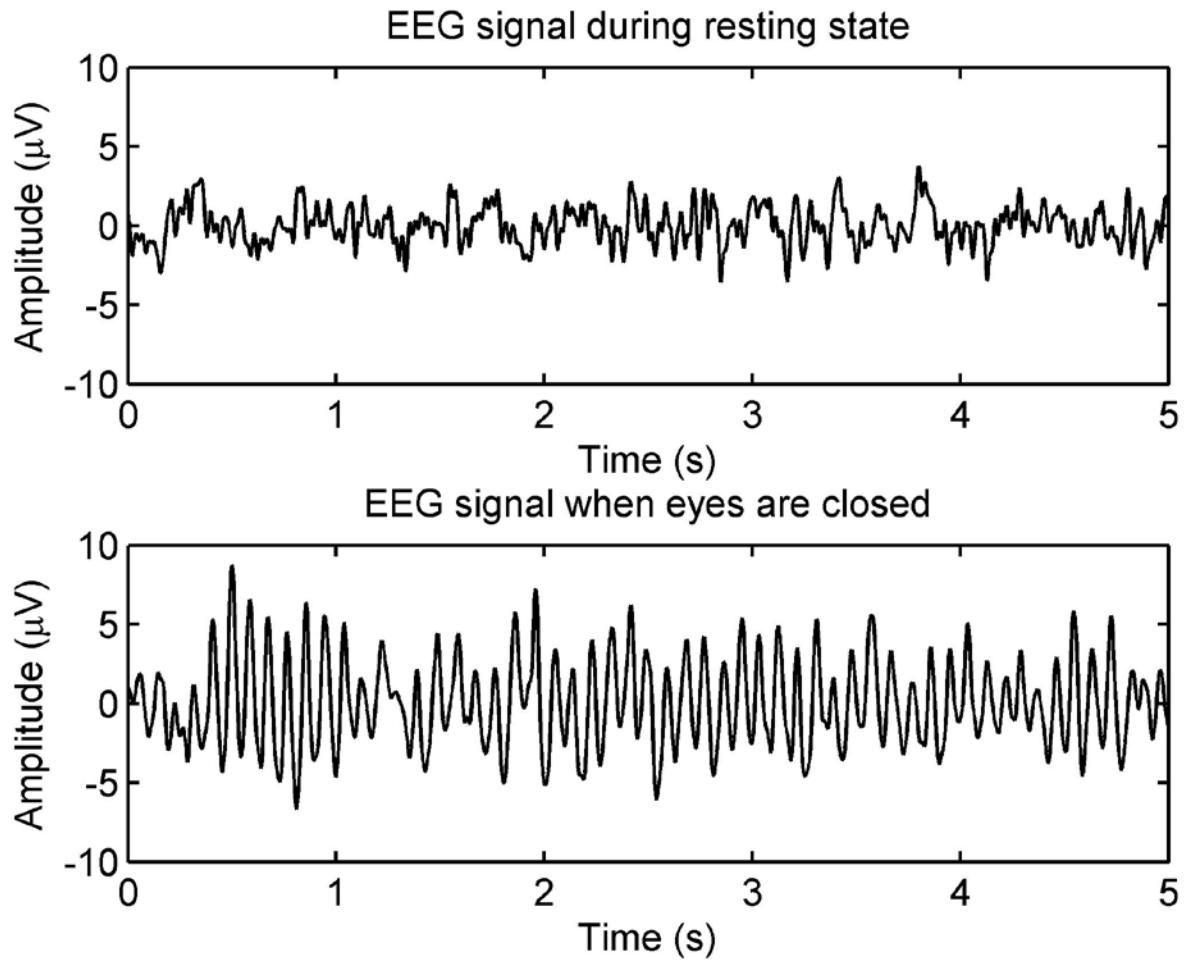
During the experiments, the subject was instructed to sit back, relax and move as little as possible. Four gold cup electrodes were placed on the occipital lobe location of the scalp (as seen in Figure 15). The reason for selecting occipital lobe to collect EEG signal was because previous EEG studies have shown that the alpha wave can be observed clearly in this area [39, 71]. The EEG signal was recorded for at least 120 seconds as the subject sit quietly. After this resting state, the subject was given an instruction to close eyes for at least 180 seconds. In the first session, the blue and orange EEG leads were connected together to the ground of the differential amplifier. In the following five sessions, the positions of reference and input electrodes altered in the ways shown in Table 2 so that the effects of different electrode orientations on the acquired EEG signal energy could be investigated.

The amplifier circuit (described in Section 4.1) was able to acquire and amplify the signal with a gain of 7,320 and a common-mode rejection ratio (CMRR) over 110 dB. In each experiment, we were able to observe EEG at subject's resting-state with eyes open. Then, the alpha wave was observed after the subject closed eyes. Figure 16 presents two typical recorded signals when subject's eyes open (top panel) and closed (bottom panel). Figure 17 demonstrates the averaged power spectra over all segments of data for six forms of electrode connections. From this figure, the alpha wave can be clearly observed.

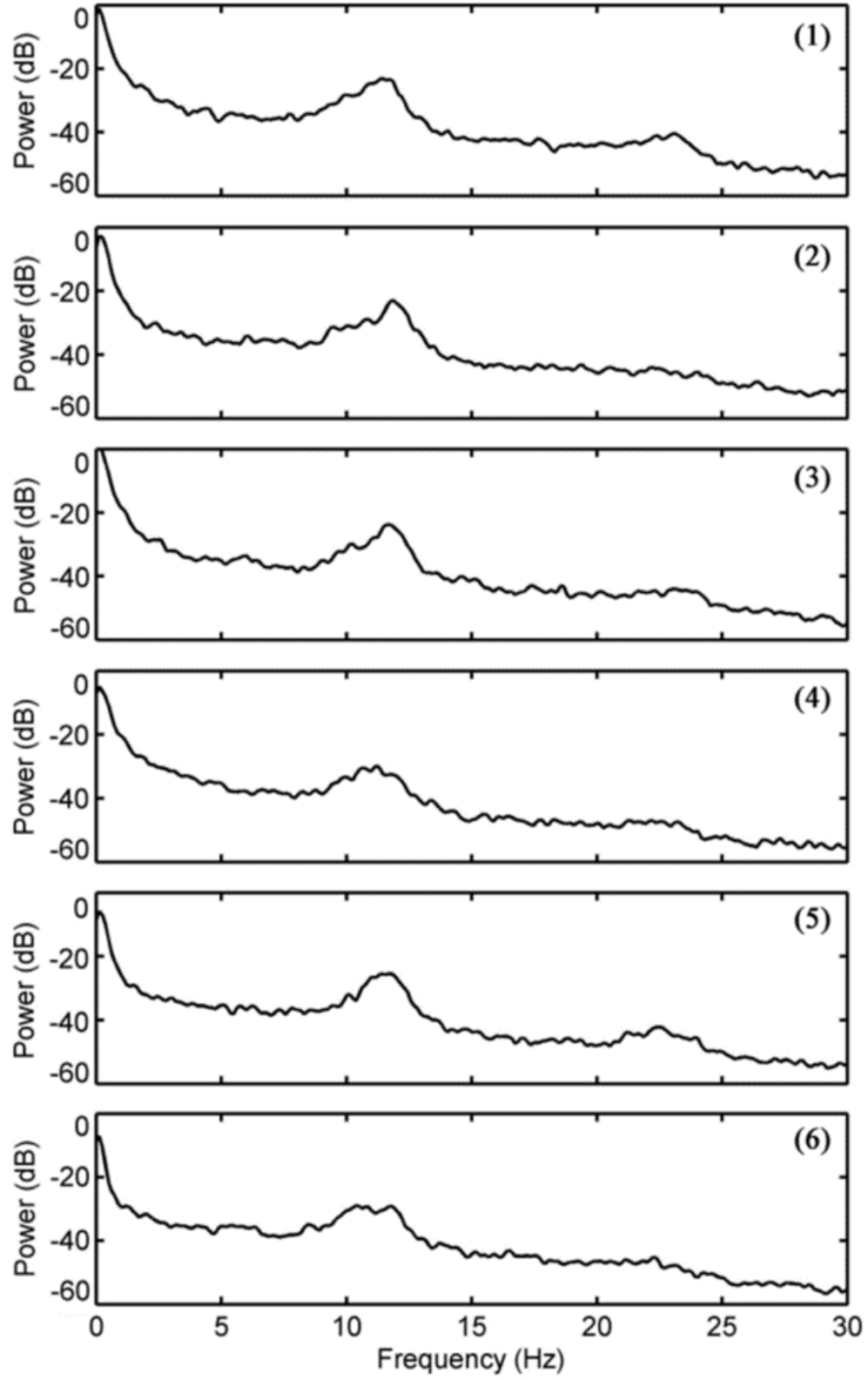
To determine whether the change of electrode orientation affects the energy of the alpha wave, a one-way ANOVA test was conducted to test the truthfulness of the null hypothesis stated

previously. Our calculation revealed that not all the averaged energy of alpha wave calculated from the six electrode orientations were equal. At least the means of alpha wave energy from two orientations were different ( $p < 0.01$ ). Therefore, the null hypothesis was rejected, and we concluded that the orientation of electrodes affected the alpha wave energy.

A box plot of the alpha-wave energy values is shown in Figure 18. It can be seen that the energy values at the six orientations differ between orientation groups (1, 2, 3, 5) and (4, 6). The energy values for group 4 and group 6 were smaller than other orientations. Table 2 summarizes the six connections and the corresponding signal central frequencies and energy. Among six experiment sessions, the reference channels in two sessions were connected at crisscross location (1, 2), two were connected vertically (3, 5), and the remaining two electrodes were connected horizontally (4, 6). Observed from the Table 2, it was demonstrated that the reference connections at crisscross orientation generated highest signal power, while the reference connections at the horizontal orientation generated the smallest signal power. This suggested that the direction of the maximum gradient of the alpha wave on the occipital site did not lie horizontally.



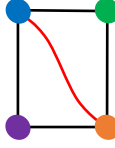
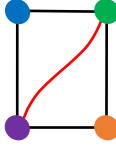

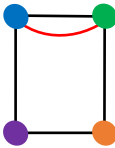
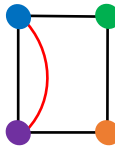
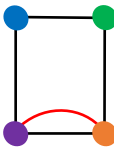
**Figure 16.** Typical EEG waveforms collected during experiments. The top panel presents the waveform when the subject's eyes were open, and the bottom panel presents the waveform when the subject's eyes were closed. This figure is adapted from our publication [70] (© 2014 IEEE).



**Figure 17.** Spectral plots of signals collected from six electrode orientations. The alpha wave components within 8 – 13Hz range can be observed in all six cases. This figure is adapted from our publication [70] (© 2014 IEEE).

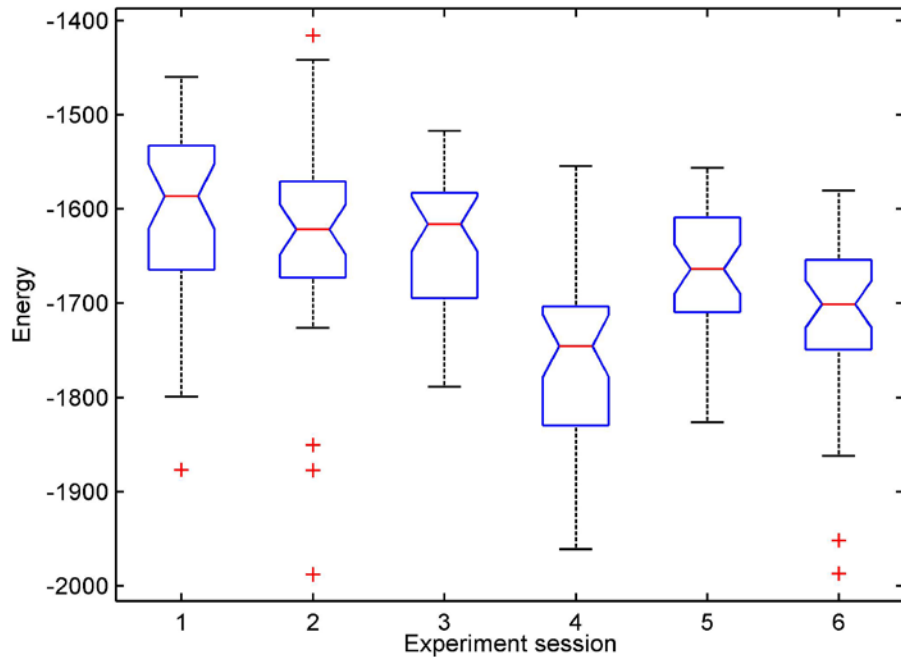


**Table 2.** Schematic of electrode connections in feasibility experiment. This table is adapted from our publication [70] (© 2014 IEEE).

| Experiment session     | 1   | 2   | 3   | 4  | 5   | 6   |
|------------------------|---|---|---|--|---|---|
| Electrodes orientation |  |  |  |  |  |  |
| Reference connection   | Blue, Orange  | Green, Purple   | Green, Orange   | Blue, Green  | Blue, Purple  | Purple, Orange  |
| Peak frequency (Hz) *  | 11.72   | 11.84   | 11.72   | 11.23  | 11.72   | 11.72   |
| Power (dB) **          | -23.35  | -22.9   | -23.76  | -29.86   | -25.47  | -29.14  |

\* The frequency where maximum magnitude of power is observed within 8 – 13 Hz alpha frequency band.

\*\* Power at the peak frequency.



**Figure 18.** Box plot of alpha-wave energy in six electrode orientations. Median values are labeled as the dash lines in the center of boxes. The margins at two sides of the box represent 25th and 75th percentiles. The red color “+” crisscross marks in the plot represent outliers. This figure is adapted from our publication [70] (© 2014 IEEE).

Our feasibility study demonstrated that EEG signal, including the alpha wave, could be recorded reliably when electrodes were placed at a separation of approximately 20 mm. Further, our study found that the signal energy was related to the orientation of the recording electrodes on the scalp. We changed the orientations of recording electrodes and compared the energy values of alpha wave signal recording using electrode at different orientations. The results indicated that there was at least one favorable orientation to optimize signal quality. The results derived from this chapter provided experimental evidence for the design and construction of a single-unit sensor.

## **5.0 FORWARD SOLUTION OF MULTI-SHELL MODELS**

### **5.1 MONTE CARLO SIMULATION**

The feasibility experiment validated that the closely spaced EEG electrodes with placement same to single-unit sensor design could acquire EEG. Furthermore, a quantitative analysis was needed to study the overall feasibility of the sensor, including a comparative analysis of the sensor to standard 10-20 systems, in order to compare with the current gold standard as the benchmark. These objectives could not be accomplished solely by performing experiments.

Therefore, a set of simulations was performed to quantitatively study: 1) can the sensor acquire EEG reliably? 2) will the selection of sensor orientation be an important factor to influence signal strength? The results demonstrated positive answers to these questions. Moreover, the signal sensor acquired was calculated to be comparable to the signal from the standard 10-20 system. These results warranted the further design and construction of a single-unit wireless EEG sensor.

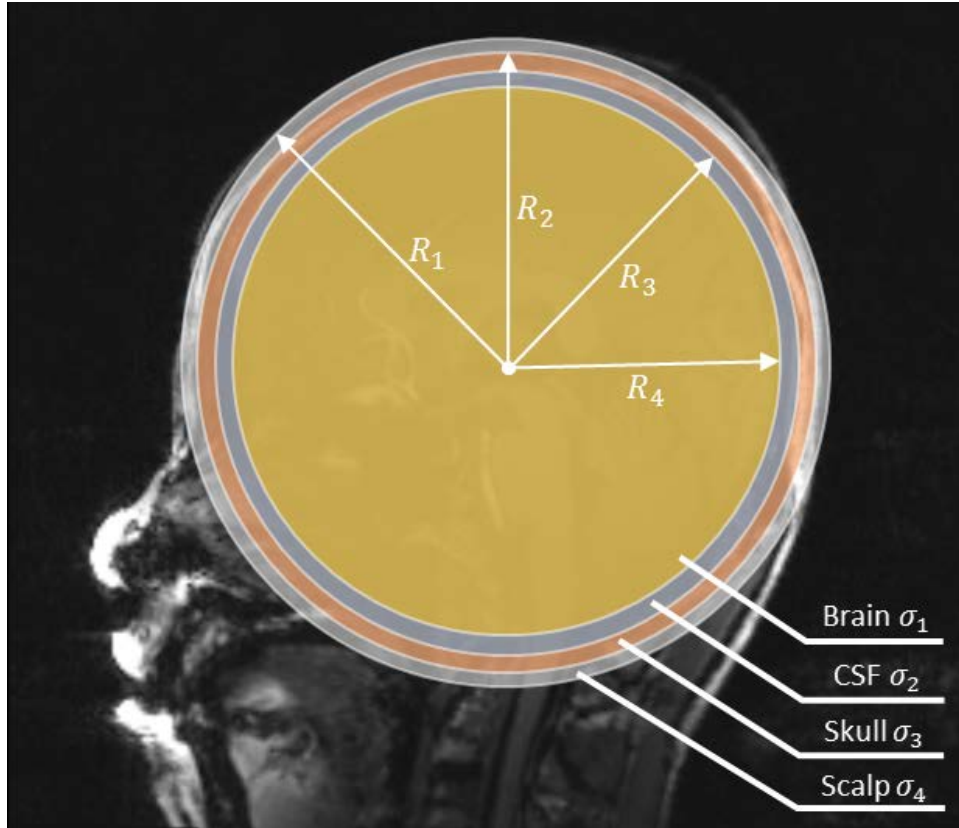
#### **5.1.1 Simulation Method**

In the simulation, three mathematical models were built to help analytically compute the theoretical scalp potential: 1) a concentric multi-layer spherical volume conductor model which described the electrical conductivities and dimensions of each layer of the head; 2) a source model which represented the assembled electrical neural activity within a small region of the brain, and 3) a model of single-unit wireless EEG sensor which included four electrodes for the measurement of EEG on the surface of the scalp surface.

#### 5.1.1.1 Concentric Multi-Shell Spherical Volume Conductor Model

Computationally determine the scalp electrical potential resulting from sources located within the brain required a volume conductor model. The model contained parameters to reflect equivalent head geometry and electrical conductivities. It was utilized to simulate the voltage distribution on scalp generated by the neuronal sources inside the brain. While models employing the boundary element method (BEM) and the finite element method (FEM) constructed full informational volume models [71-73] with greater details to describe human head, a spherical model, comparatively, might be simpler to speed up the computation. The human head could be modeled as a sphere or spheroid of single scalp layer, or multiple layers with various radius and conductivity parameters describing brain, cerebrospinal fluid (optional), skull and scalp. Some four-layer models were developed in previous studies such as Stok [68], as well as Coffin and Cohen [74].

This study utilized a concentric four-layer spherical model from Sun [75]. The four layers were the brain, cerebrospinal fluid (CSF), skull, and scalp, each with unique conductivity and thickness parameter. The model and analytic solutions were presented by Stok [68]. This model assumed  $R_1 = 9$  cm head radius. The skull, CSF and brain are  $R_2 = 0.9467R_1$ ,  $R_3 = 0.8667R_1$ , and  $R_4 = 0.8400R_1$  proportional to the 9-cm head radius, respectively. The Stok model [68] also assumed the scalp, skull, CSF and brain have conductivity of  $\sigma_4 = 0.33$ ,  $\sigma_3 = 0.0042$ ,  $\sigma_2 = 1.0$ , and  $\sigma_1 = 0.33$  S/m, accordingly. In summation, there were eight parameters for the four-layer head model (as illustrated in Figure 19).



**Figure 19.** A four-layer spherical volume conductor model. It contained layers representing brain, cerebrospinal fluid (CSF), skull, scalp, with corresponding radius  $R_4$ ,  $R_3$ ,  $R_2$ ,  $R_1$ , and corresponding conductivity values  $\sigma_1$ ,  $\sigma_2$ ,  $\sigma_3$ , and  $\sigma_4$ .

#### 5.1.1.2 Current Dipole Source Models

Some small clusters of active neurons in the grey matter of the brain generating electrical current were approximated by current dipole models. The current dipole model source was characterized by six parameters, of which three described the dipole location in three-dimensional coordinate system, and the other three described the strength vector [67]. Depending on activities and populations of active neurons, single or various dipoles in a whole could be used to affect the surface potential of the scalp. In some EEG studies where one dipole might not sufficiently

describe the current sources within the brain, multiple dipole models with different location and strength parameters could be used simultaneously.

To quantitatively calculate the neuronal activities, our study referred to the analytical analysis by previous studies [42, 71, 76]. The researchers constructed realistically shaped 3D individual neuron model to investigate the contribution of each neuron in the neocortex to electrical current. Hämäläinen decided that the average volume current density of cerebral cortex during normal brain activity was  $175 \text{ nA/mm}^2$  (equivalent to  $\text{nA} \cdot \text{mm/mm}^3$ ) [42]. Then, the average value of dipole moment  $M$  with cerebral cortex surface with neuron population value  $s_i$  and cortical thickness value  $d$  could be analytically computed. The computation was proposed by da Silva [71]:

$$M = s_i \times d \times 175 (\text{nA} \cdot \text{mm}) \quad (3)$$

The cerebral cortex is the central information processing module of the brain [77]. It is a folded thick sheet of gray tissue that typically has a thickness between 2 mm to 5 mm, with 1,600 – to 4,000  $\text{cm}^2$  surface area and at least  $10^{10}$  neurons for an adult brain [42, 78], which makes the average density of neuron to be  $10^4$  neurons per square millimeter [49]. The da Silva's study [71] determined the average value of the cortical thickness  $d$  to be 3 mm. By supplementing  $d = 3 \text{ mm}$  into the Equation (3) above, the average strength of the dipole moment  $M$  was then calculated by:

$$M = s_i \times 525 (\text{nA} / \text{mm}) \quad (4)$$

where  $525 \text{ nA/mm}$  was the average surface current density [71]. It was assumed that the area of activation was uniformly distributed in three different ranges:  $(0 - 10 \text{ cm}^2)$ ,  $(0 - 15 \text{ cm}^2)$ , and  $(0 - 20 \text{ cm}^2)$ . This expression was later used in the simulation model for the calculation of strength of dipole moment.

### 5.1.1.3 An Algorithm for Computing EEG Forward Solution

To computationally calculate the electrical current on the surface of a spherical volume conductor model, a forward computation algorithm presented by Sun [75] in 1997 was utilized in the study. The Sun's algorithm is beneficial when performing large numbers of simulation iterations in our current study. The approach provides a closed-form approximation to a sum of infinite series that had been modeling the multi-shell spherical model, while substantially reducing computation cost (8.9 % compared to the direct method) and mean squared error (0.066%) [75]. According to the algorithm, the potential value  $v$  at a surface point  $s$  at the multi-shell concentric spherical volume conductor is calculated by:

$$v = \frac{1}{4\pi\sigma_4 R^2} \sum_{n=1}^{\infty} c_n f^{n-1} \mathbf{m} \cdot \left[ \mathbf{r}_\theta P_n(\cos \theta) + \mathbf{t}_\theta \frac{P_n^1(\cos)}{n} \right] \quad (5)$$

In the above relationship, parameter  $\sigma_4$  denotes the conductivity value of the scalp, and  $R = \sqrt{s_x^2 + s_y^2 + s_z^2}$  is the outer radius of the spherical volume conductor. The term  $C_n$  is calculated by  $C_n = \frac{(2n+1)^4 (cd)^{2n+1}}{\Gamma}$  [74], of which the term  $\Gamma$  is expressed as:

$$\begin{aligned} \Gamma = & d^{2n+1} \left[ b^{2n+1} n \left( \frac{\sigma_1}{\sigma_2} - 1 \right) \left( \frac{\sigma_2}{\sigma_3} - 1 \right) (n+1) + c^{2n+1} \left( \frac{\sigma_1}{\sigma_2} n + n + 1 \right) \left( \frac{\sigma_2}{\sigma_3} n + n + 1 \right) \right] \\ & \cdot \left[ \left( \frac{\sigma_3}{\sigma_4} n + n + 1 \right) + (n+1) \left( \frac{\sigma_3}{\sigma_4} - 1 \right) d^{2n+1} \right] \\ & + (n+1) c^{2n+1} \left[ b^{2n+1} \left( \frac{\sigma_1}{\sigma_2} - 1 \right) \left( \frac{\sigma_2}{\sigma_3} n + \frac{\sigma_2}{\sigma_3} + n \right) + c^{2n+1} \left( \frac{\sigma_1}{\sigma_2} n + n + 1 \right) \left( \frac{\sigma_2}{\sigma_3} n - 1 \right) \right] \\ & \cdot \left[ n \left( \frac{\sigma_3}{\sigma_4} - 1 \right) + \left( \frac{\sigma_3}{\sigma_4} n + \frac{\sigma_3}{\sigma_4} + n \right) d^{2n+1} \right] \end{aligned} \quad (6)$$

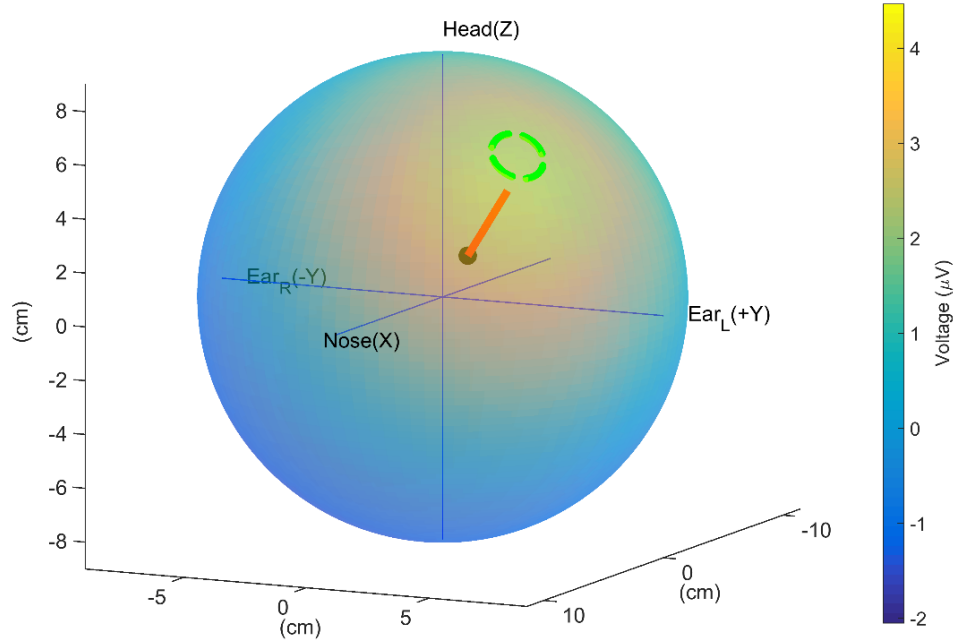
where  $\mathbf{r}_0 = \frac{\mathbf{r}}{|\mathbf{r}|}$  is the radial unit vector of dipole location vector  $\mathbf{r}$ , and  $\mathbf{t}_0$  is a tangential unit vector that can be represented in terms of dipole location vector  $\mathbf{r}$  and surface point  $\mathbf{s}$  where potential value  $v$  is calculated:

$$\mathbf{t}_0 = \frac{\mathbf{r} \times \mathbf{s} \times \mathbf{r}}{|\mathbf{r} \times \mathbf{s} \times \mathbf{r}|} \quad (7)$$

In this equation, six parameters characterizing dipole current source are  $(r_x, r_y, r_z)$  and  $(m_x, m_y, m_z)$ , which accordingly define the dipole location vector  $\mathbf{r}$  and the current dipole moment  $\mathbf{m}$ . The potential  $v$  is calculated at the surface point  $\mathbf{s}$  as defined by  $(s_x, s_y, s_z)$ .

To study the scalp electrical potential recorded by the single-unit sensor, a model describing the configuration of single-unit sensor electrode structure was constructed. Specifically, four arcs plotted by many surface points were created on the surface of the sphere model to represent four arc-shaped electrodes of the single-unit sensor, with a spacing of 20 mm between opposite two arcs (Figure 20). The distance between opposite arcs was defined according to arc (Euclidean) distance in 3D space. An electrode covered a certain area of the scalp. Each of the arc-shaped electrodes, therefore, measured an averaged potential summed from potentials derived from each location covered underneath it. The measurement value of each arc-shaped electrode was the average of all potential values on all points on or close to the arc. The potential differences between the two configurations were then calculated.





**Figure 20.** Visualization of simulation program created in this study. The four green arcs on the surface of the sphere represent four electrodes. The black dot represents the location of the dipole. The red line pointing from black dot to sphere surface represents the dipole moment. The color on the surface of the sphere represents the calculated strength of the potential, with corresponding values indicated in the color bar. This figure is adapted from our publication [79] (© 2015 IEEE).

During the simulation, a dipole source was uniformly randomly generated a shell of the spherical model. The shell was assumed to be the gray matter layer within the brain, imitating the actual scenario of active neuron distribution in gray matter. According to Kiourti's five-layer head model, the thickness of this layer was set to be 14 mm from the sphere surface [80]. 1,000 single-unit sensors were then randomly generated on the sphere surface. 1,000 dipoles were generated, and the overall histogram of the potential difference was computed. In the simulation of the single-unit sensor, the bigger potential difference between the two pairs of outputs was saved for all generated sensors. Simultaneously, one potential difference was also randomly selected and saved among the two pairs in all generated sensors.

For each dipole, a large number of surface points were randomly generated on the sphere model following the uniform distribution, so that there should be an equivalent amount of points in any randomly selected surface area with the same size (as presented in Figure 21 (a)) on the sphere surface. To satisfy such random points generation, the location  $x, y, z$  of each point was computed as follow:

- 1) Generate  $u, v \in [0,1]$  as two independent standard uniform variants. Then, the variants

$\theta$  and  $\varphi$  could be derived as follow:

$$\theta = 2\pi u$$

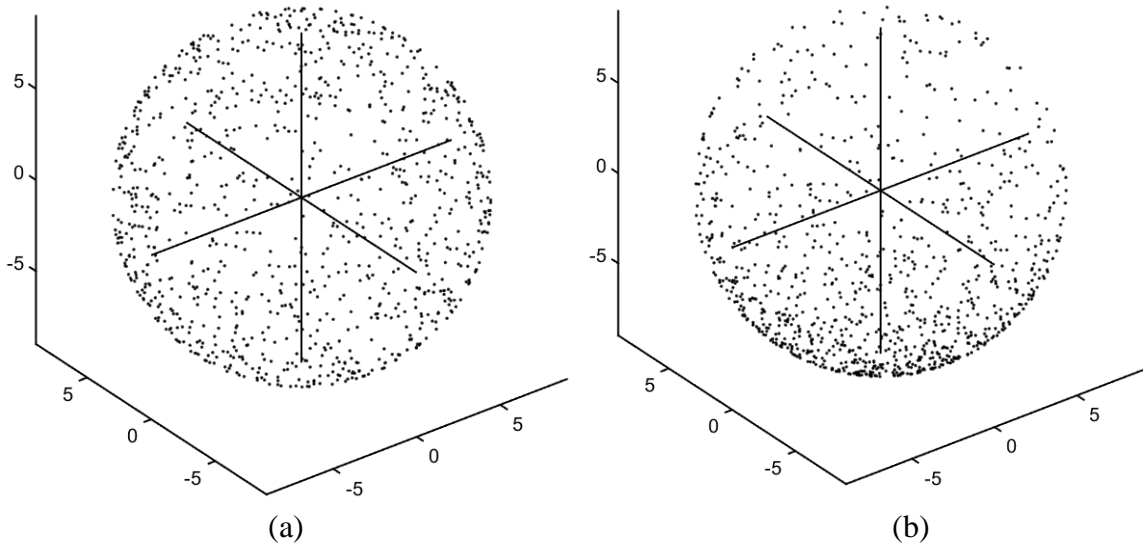
$$\varphi = \cos^{-1}(2v-1)$$

- 2) The surface point was expressed in spherical coordinate:

$$x = R \cos \theta \sin \varphi$$

$$y = R \sin \theta \sin \varphi$$

$$z = R \cos \varphi$$

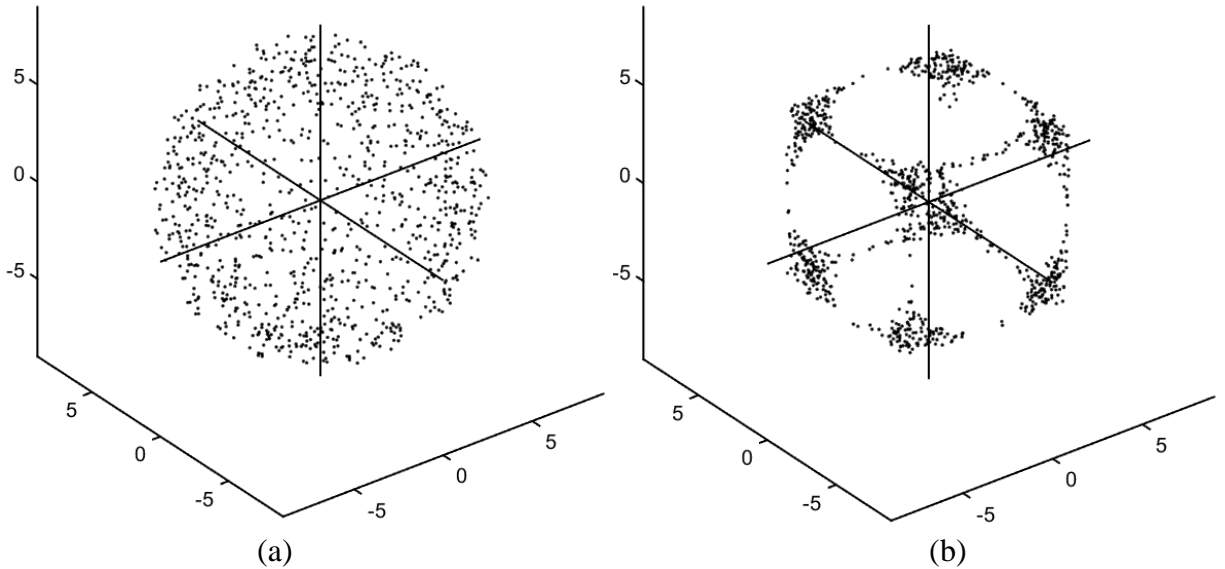


**Figure 21.** Randomly generate sensor locations on the sphere surface. (a) Sensor locations as denoted by points are evenly distributed on the surface, which is the correct way of randomly generating surface points. (b) Points are densely clustered near the south pole, which should be avoided.

A histogram of these differential potentials was utilized to display the distribution of these potentials. The above process was repeated for a large number of randomly generated dipoles. The locations of these dipoles were all distributed uniformly within the 14-mm shell in the head model, and their orientations were also randomized.

The dipolar sources were generated randomly and uniformly within the gray matter shell of the spherical model. In any random space of the same size, there should be the same number of dipolar sources, as is shown in Figure 22 (a). To ensure the point distribution was the same as that in Figure 22 (a), the point generation method was as follow:

- 1) Generated  $X_1$ ,  $X_2$ , and  $X_3$  three independent standard normal variants. We also limited  $X_1$ ,  $X_2$ , and  $X_3 \in [aR, R]$ , where the  $aR$  and  $R$  defined the boundaries of the gray matter.
- 2) Selected the points  $(X_1, X_2, X_3)$  satisfying  $(aR)^2 \leq X_1^2 + X_2^2 + X_3^2 \leq R^2$ .

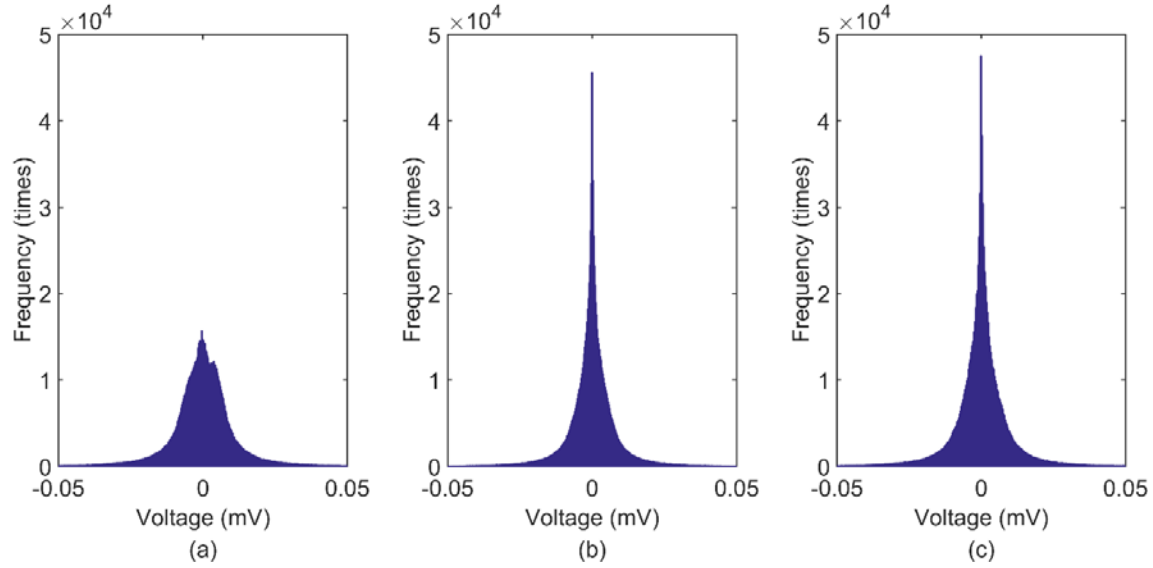


**Figure 22.** Randomly generate dipole locations within the layer of gray matter. Left panel: Dipole locations as denoted by points are evenly distributed within the layer, which is the correct way of randomly generating surface points. Right panel: Points are densely clustered near corners of a cube, which needs to be avoided.

The sum of all the histograms according to all the dipoles was plotted as an overall indicator of the potential distribution recorded by the sensor. The percentage above a given threshold in this plot was used to evaluate the ability of the single-unit sensor in acquiring EEG signal. To compare the EEG signals recorded by the four-arc electrodes with the EEG recording employing the standard 10-20 system, we further modeled the electrodes in a standard 10-20 system. For each dipole, two surface points representing two adjacent electrodes were created on the surface of the sphere, and the potential difference between adjacent electrodes was computed. The inter-electrode distance was set to 45 mm [81]. 1,000 bipolar recordings were calculated for each dipole.

### 5.1.2 Experimental Results

Figure 23 shows the distribution of potential differences of single-unit sensor model comparing to the standard 10-20 system model considering cortical surface area range ( $0 - 15 \text{ cm}^2$ ). The center shoots for subplots (b) and (c) demonstrates the relatively high occurrence of small values. The sensor model selecting bigger potential differences among two pairs showed fewer occurrences of smaller values. In Table 3, we list detailed comparison between the single-unit sensor model and the standard 10-20 system model. This table compares the percentage of potential difference larger than a certain threshold among all recorded potential differences. At either  $0.5 \text{ } \mu\text{V}$  or  $1 \text{ } \mu\text{V}$  threshold, the single-unit sensor selecting bigger potential differences showed comparable performance as the 10-20 system. The choice of thresholds was based on the measurement resolution of today's EEG amplifiers. For example, the TI ADS1299 analog front-end amplifier has 24-bit resolution, which allows it to measure as accurately as about  $0.3 \text{ } \mu\text{V}$ .



**Figure 23.** The potential distribution plots. The potential distribution for (a) our proposed sensor selecting bigger potential difference among two pairs; (b) the sensor randomly selecting one pair of electrodes among the two; (c) Bipolar recordings acquired from two adjacent electrodes in the standard 10-20 system. This figure is adapted from our publication [79] (© 2015 IEEE).

**Table 3.** Comparison of single-unit sensor and electrodes employing 10-20 mapping. This table is adapted from our publication [79] (© 2015 IEEE).

| Surface Area Range      | Voltage Threshold ( $\mu\text{V}$ ) | Sensor Max Difference (%) | Sensor Random Difference (%) | 10-20 System Difference (%) |
|-------------------------|-------------------------------------|---------------------------|------------------------------|-----------------------------|
| (0 – 10 $\text{cm}^2$ ) | 0.5                                 | 84.17                     | 69.58                        | 83.51                       |
|                         | 1                                   | 69.92                     | 51.99                        | 72.91                       |
| (0 – 15 $\text{cm}^2$ ) | 0.5                                 | 88.41                     | 76.01                        | 87.44                       |
|                         | 1                                   | 77.66                     | 61.38                        | 78.84                       |
| (0 – 20 $\text{cm}^2$ ) | 0.5                                 | 91.16                     | 80.56                        | 90.08                       |
|                         | 1                                   | 82.59                     | 68.19                        | 82.87                       |

Our simulation study results demonstrated that the sensor with closely-spaced electrodes could acquire EEG. The study further demonstrated that, when selecting certain sensor

configuration, the quality of the acquired signal was similar to that of the standard 10-20 system. The results of this simulation study indicated that the single-unit wireless EEG sensor was feasible and warranted further study and construction.

## **5.2     PROBABILISTIC MODELS FOR SOURCE-POTENTIAL RELATIONSHIP**

Section 5.1 presents the simulation of a potential distribution on the scalp surface of a volume conductor model resulting from dipolar sources through a multi-layer brain model, which was a relatively accurate guess based on one million simulation iterations. Meanwhile, an analytical function characterizing the source-potential relationship was ideally the goal. This section presents the formulation of a probabilistic model that establishes the relationship between the signal strength on scalp originating to the strength of cortical sources inside a statistically modeled human brain. Benefits of deriving such an analytical relationship include:

- 1) The method could be generalized to derive many variations of cases of surface potential problems knowing dipolar sources located within brain models.
- 2) The analytic function assists the evaluation of skin-contact bio-potential measurement tools. Understanding the optimal signal characteristic gives the proposed device a clear performance indication.

The result was presented by a multi-variant probability density function. These analytical results provided insights into the workings of the single-unit sensor.

### 5.2.1 Formation of the Mathematical Problem

The derivation of a probability density function (*pdf*) of potential on a particular scalp surface point started from the known *pdfs* of dipolar sources inside the human brain. A forward computing algorithm described in [75] was employed. This problem could be formulated into an analytical form: deriving the *pdf* of a function output knowing the multiple *pdfs* of inputs, which was a  $1 \times N$  dimensional vector.

When considering the *pdfs* of input variables (e.g., distribution of dipolar sources), the exact distributions remained unknown. It remained a part of the work for future researchers to determine the analytical formations statistically. Meanwhile, if we assumed distributions are given, also knowing the forward computational method which links the potential at each point on scalp surface to the underlying sources, the goal was to yield the distribution of scalp potential.

The input to the volume conductor model was an 8-dimensional vector, among which three parameters were dipole location vector, three were dipole orientation vector, and two were surface points (the third surface point could be yield knowing first two, and thus eliminated so simplify calculation). The output was a scalar, which was the potential at a specified surface point. The forward solution provided surface potential with respect to dipole parameters and electrode locations. If the *pdfs* of inputs were known, output *pdf* could be calculated.

The solution to the forward problem [75] was abstracted and interpreted by:

$$v = u(\mathbf{X}) \quad (8)$$

where  $\mathbf{X}$  was a vector of eight independent continuous random variables. Among eight random variables, the variables  $r_x, r_y, r_z$  determined the dipole location vector  $\mathbf{r}$ . The variables  $m_x, m_y, m_z$  determined the dipole moment  $\mathbf{m}$ . The variables  $s_x$  and  $s_y$  were used to determine the scalp

surface point  $s$  where potential  $v$  was measured. The third variable  $s_z$  determining the surface point could be derived from  $s_x$  and  $s_y$  knowing the dimension of the sphere, and thus was neglected to simplify the calculation. Therefore, the known conditions were:

- 1)  $\mathbf{X} = [r_x, r_y, r_z, m_x, m_y, m_z, s_x, s_y]$
- 2) The variables  $r_x, \dots, s_y$  were independent and continuous random variables. Their individual *pdfs* were also given.

The functions  $f_r(r_x)$ ,  $f_r(r_y)$ , and  $f_r(r_z)$  represented uniform distributions of randomly generated dipole locations within cerebral cortex range  $(aR, R)$ . The functions  $f_m(m_x)$ ,  $f_m(m_y)$ , and  $f_m(m_z)$  represented dipole moment calculated by Equation (4), in which the area of activated neuron cluster was uniformly randomly generated within the range of  $(-b, b)$ . With the above assumptions and equations being provided, the *pdf* of  $v$  was what needs to be derived. The two general conditions the functions  $f_X$  had to meet were:

- 1) Each *pdf* must be positive and single valued for all  $X_n$  ( $n \in [1, 8]$ )
- 2)  $\int_{-\infty}^{+\infty} f_X dX = 1$

Further, the eight variables  $r_x, \dots, s_y$  must satisfy the following conditions:

- 3)  $r_x, r_y, r_z \in \Re$
- 4)  $aR \leq \sqrt{r_x^2 + r_y^2 + r_z^2} \leq R$  ( $0 < a < 1$ )
- 5)  $m_x, m_y, m_z \in [-b, b]$  ( $0 < b < 1$ )
- 6)  $s_x, s_y \in [-R, R]$



where  $R$  was the outer radius of the sphere. The constant  $a$  and  $b$  were positive coefficients and  $a, b \in (0,1)$ . Two techniques were used to find the probability density function of potential  $v$ , namely, the distribution function technique, and the change-of-variable technique.

### 5.2.2 Approach to the Mathematical Problem

Given the individual *pdf* of eight input variables, the conditions of every vector element in  $\mathbf{X}$  was predefined above. The joint distribution function of eight vector elements of  $\mathbf{X}$  was denoted as  $f_{\mathbf{X}}(\mathbf{X})$ . Having  $\mathbf{X}$  as a vector of eight elements and function output as a scalar, the problem was solvable using the change of variables theorem with certain degrees of transformation. Specifically, the dimension of output was increased so that instead of  $v$  being a scalar, the new output  $\mathbf{Z}$  had the same dimension as the input  $\mathbf{X}$ . The  $N$ -dimensional transformation of random variables had been studied and proven in vast literature before, such as section 14.4 of [82], If  $\mathbf{Z} = \mathbf{u}(\mathbf{X})$  was invertible, then, the problem was formulated as:

$$g_{\mathbf{Z}}(\mathbf{Z}) = f_{\mathbf{X}}(\mathbf{u}^{-1}(\mathbf{Z})) \left| \det \frac{\partial \mathbf{X}}{\partial \mathbf{Z}} \right| \quad (9)$$

To construct the vector  $\mathbf{Z}$  that has the same dimension as  $\mathbf{X}$ , we added seven known continuous functions  $z_1, \dots, z_7$ . And we derived the formulations below:

$$\begin{aligned} z_1 &= h_1(r_x, \dots, s_y) \\ &\vdots \\ z_7 &= h_7(r_x, \dots, s_y) \end{aligned}$$

Then, a new vector function could be constructed as follow:

$$\begin{bmatrix} v \\ z_1 \\ \vdots \\ z_7 \end{bmatrix} = w \begin{bmatrix} r_x \\ r_y \\ \vdots \\ s_y \end{bmatrix}$$

where  $w$  was the function  $[h_1, h_2, \dots, h_7]^T$ . As mentioned, the choices of  $\mathbf{Z}$  could come from the known vectors. By quadratic change of variables using Equation (9), the joint *pdf* of  $v, z_1, \dots, z_7$ ,  $g_{v, z_1, \dots, z_7}(v, z_1, \dots, z_7)$  could be written as:

$$g_{v, z_1, \dots, z_7}(v, z_1, \dots, z_7) = f(r_x, \dots, s_y) \left| \det \frac{\partial(r_x, \dots, s_y)}{\partial(v, z_1, \dots, z_7)} \right| \quad (10)$$

where the Jacobian in Equation (10) was an  $8 \times 8$  matrix:

$$J = \begin{bmatrix} \frac{\partial r_x}{\partial v} & \frac{\partial r_x}{\partial z_1} & \dots & \frac{\partial r_x}{\partial z_7} \\ \frac{\partial r_y}{\partial v} & \ddots & & \\ \vdots & & \ddots & \\ \frac{\partial s_y}{\partial v} & & & \frac{\partial s_y}{\partial z_7} \end{bmatrix}$$

The simplest form of Jacobian matrix was needed to simplify subsequent calculations. Therefore, the vector  $\mathbf{Z}$  could be constructed as  $\mathbf{Z} = [v, r_y, r_z, m_x, m_y, m_z, s_x, s_y]$ , where  $z_1 = r_y$ ,  $z_2 = r_z$ ,  $z_3 = m_x$ , ...,  $z_7 = s_y$ . Solve for the variables  $r_y, \dots, s_y$  we could get  $r_y = z_1$ ,  $r_z = z_2$ ,  $m_x = z_3$ , ...,  $s_y = z_7$ . This choice of the vector  $\mathbf{Z}$  eliminated many terms in the Jacobian matrix. The Jacobian matrix could then be simplified as:

$$J = \begin{bmatrix} \frac{\partial r_x}{\partial v} & \frac{\partial r_x}{\partial z_1} & \dots & \frac{\partial r_x}{\partial z_7} \\ \frac{\partial r_y}{\partial v} & \ddots & & \\ \vdots & & \ddots & \\ \frac{\partial s_y}{\partial v} & & & \frac{\partial s_y}{\partial z_7} \end{bmatrix} = \begin{bmatrix} \frac{\partial r_x}{\partial v} & 0 & 0 & 0 & 0 & 0 & 0 & 0 \\ \frac{\partial r_y}{\partial v} & 1 & 0 & 0 & 0 & 0 & 0 & 0 \\ \frac{\partial r_z}{\partial v} & 0 & 1 & 0 & 0 & 0 & 0 & 0 \\ \frac{\partial m_x}{\partial v} & 0 & 0 & 1 & 0 & 0 & 0 & 0 \\ \frac{\partial m_y}{\partial v} & 0 & 0 & 0 & 1 & 0 & 0 & 0 \\ \frac{\partial m_z}{\partial v} & 0 & 0 & 0 & 0 & 1 & 0 & 0 \\ \frac{\partial s_x}{\partial v} & 0 & 0 & 0 & 0 & 0 & 1 & 0 \\ \frac{\partial s_y}{\partial v} & 0 & 0 & 0 & 0 & 0 & 0 & 1 \end{bmatrix}$$

The calculation of the above 8×8 Jacobian matrix gave:

$$\det(J) = \frac{\partial r_x}{\partial v} \quad (11)$$

Substitute the above result into Equation (10), we got the equation as follow:

$$g_{v,z_1,\dots,z_7}(v, z_1, \dots, z_7) = f(r_x, \dots, s_y) \frac{\partial r_x}{\partial v} \quad (12)$$

The joint distribution  $g_{v,z_1,\dots,z_7}(v, z_1, \dots, z_7)$  could be calculated given  $f(r_x, \dots, s_y) \frac{\partial r_x}{\partial v}$  was solvable. To take a step further, by definition, the marginal distribution  $g_v(v)$  was derived by performing integral on the joint distribution with respect to other terms:

$$g_v(v) = \int \dots \int g_{v,z_1,\dots,z_7}(v, z_1, \dots, z_7) dz_1 \dots dz_7 \quad (13)$$

Then, substituted the Equation (12) into (13) and applied superposition principle, we derived:

$$g_v(v) = \int \dots \int f_r(r_x) \dots f_s(s_x) dz_1 \dots dz_7 \frac{\partial r_x}{\partial v} \quad (14)$$

Recalled that  $z_1 = r_y$ ,  $z_2 = r_z$ ,  $z_3 = m_x$ , ...,  $z_7 = s_y$ , the  $z_1, \dots, z_7$  variables in Equation (14) were supplemented and thus converted to the following:

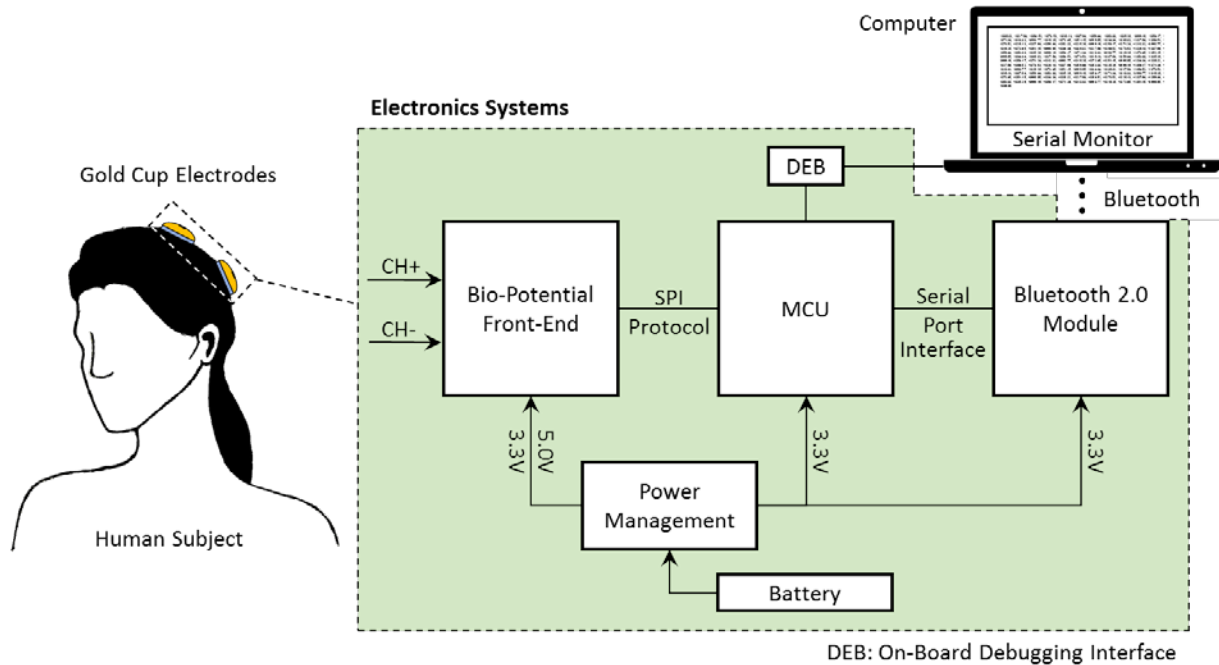
$$\begin{aligned} g_v(v) &= \int \dots \int f_r(r_x) \dots f_s(s_x) dz_1 \dots dz_7 \frac{\partial r_x}{\partial v} \\ &= \frac{\int \dots \int f_r(r_x) \dots f_s(s_x) dr_y dr_z \dots ds_y}{\frac{\partial v}{\partial r_x}} \end{aligned} \quad (15)$$

The  $g_v(v)$  was the probability density function of the surface potential  $v$  denoted in the Equation (5). Given specific distributions of individual *pdf* and the vector function  $v$ , the Equation (15) could be calculated either analytically or numerically.

## 6.0 HARDWARE DESIGN AND IMPLEMENTATION

### 6.1 PROTOTYPE DESIGN

The electronic system in the single-unit sensor is a functional building block to serve the purpose of signal acquisition, conditioning, digitization, and transmission to data hosts (e.g., PC). We illustrate a functional block diagram of the proposed system in Figure 24. The system included five main modules and their external circuitry: a) a bio-potential front-end; b) an MCU; c) a Bluetooth (version 2.0) module; d) a power management circuitry; and e) an onboard debugging interface.



**Figure 24.** Block diagram of the prototype electronic system (depicted in the green dashed area).

An EEG amplifier was needed for the application. The solution adopted in this work was the “TI ADS1299 Low-Noise, 8-Channel, 24-Bit Analog-to-Digital Converter for Biopotential Measurements” [83]. The ADS1299 was an integrated solution designed specifically for precision EEG and bio-potential applications. This biopotential front-end offered up to eight channels of bipolar signal inputs and individual low-noise programmable gain amplifier. The Delta-Sigma analog-to-digital converters (ADCs) enabled simultaneous sampling rate as high as 16 kSPS and sampling resolution to 24-bit. The input-referred noise was just as low as  $1.0 \mu\text{V}_{\text{pp}}$ , with an input bias current of 300 pA. The common-mode rejection ratio (CMRR) was -110 dB. It was equipped with various commonly-required features for EEG applications, such as lead-off detection, and built-in bias driver buffer. While coming with features the above properties, the power consumption of the chip is as low as 5 mW/channel, which was suitable for long-term operations. Controlled through a standard 4-wire SPI protocol ( $\overline{\text{CS}}$ , SCLK, DIN, DOUT), data acquisition parameters such as sampling rate, bias/reference physical arrangement, and other register setups could be configured instantaneously. Figure 25 presents the schematic design for ADS1299 and its external circuit.

The microcontroller of choice was the TI MSP430 microcontroller series. Specifically, the TI MSP430F5438 was adopted in the work, which featured 16-bit RISC architecture, 16-bit registers, 256 KB Flash, 16 KB RAM, 12-Bit ADC and ultra-low power consumption [84]. During the active mode, the power consumption was 312  $\mu\text{A}/\text{MHz}$  at 8 MHz using flash program execution. The consumption was 140  $\mu\text{A}/\text{MHz}$  at 8 MHz using RAM program execution [85]. It had 32 kHz crystals clock and high-frequency crystals up to 32 MHz. The MSP430’s architecture, combined with five low-power modes suitable for varies working conditions, was optimized to achieve extended battery life in portable applications. The chip could wake up from standby mode

in less than 5s. These features were combined with Flash memory sizes reaching 256 KB and a 16 KB SRAM. It was an ideal chip for portable measurement applications. In the hardware design, the clock was an external crystal clock SMD2520, which had a clock of 32 kHz, and the system clock was set to 21.2992 MHz by using frequency lock loop. The MSP430F5438 was utilized in the system to configure the functions of ADS1299 through SPI, such as start, stop, gain setting and sampling rate setting. It was also used to transform the data into a readable format and transmit the data to a Bluetooth module.

During the selection of a wireless data transmission module, Wi-Fi, ZigBee, and Bluetooth were considered. Wi-Fi enabled higher data throughput but higher power consumption, while ZigBee provided better power saving features but limited throughput. The Bluetooth technology was a well-balanced solution in terms of power optimization and data throughput. Therefore, the signal was further transmitted to a data port via a Bluetooth module RN-42 within a limited range. The RN-42 module employed Bluetooth 2.1 standard with low power consumption (26  $\mu$ A sleep, 3 mA connected, 30 mA transmit). It supported the UART and USB data connection interfaces. In the development, the SCI communication mode (RX, TX) through UART of the chip module was utilized. The default communication baud rate with this OEM module was 115.2 kbps. Figure 26 shows the schematic for MSP430, RN-42, and their external circuitry.

A power management circuit we developed (Figure 27) could generate regulated voltages from the coin batteries input (for example, CR2032 Lithium coin battery provide 3 V voltage) to a steady 3 V power which was needed to power up the MCU and Bluetooth module. The steady 3V power would further boost to a steady 5 V power source. The steady 5 V powered the EEG front-end amplifier circuit and its eternal reference circuit.

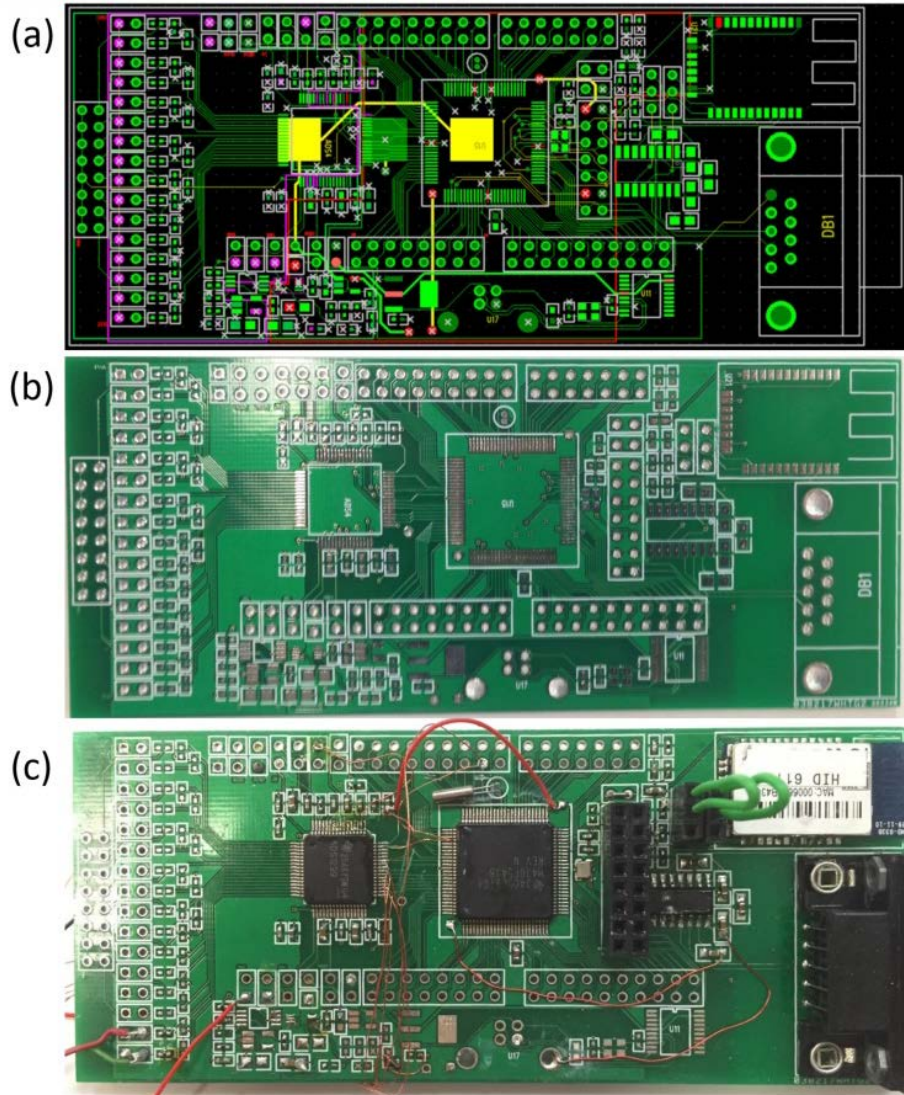






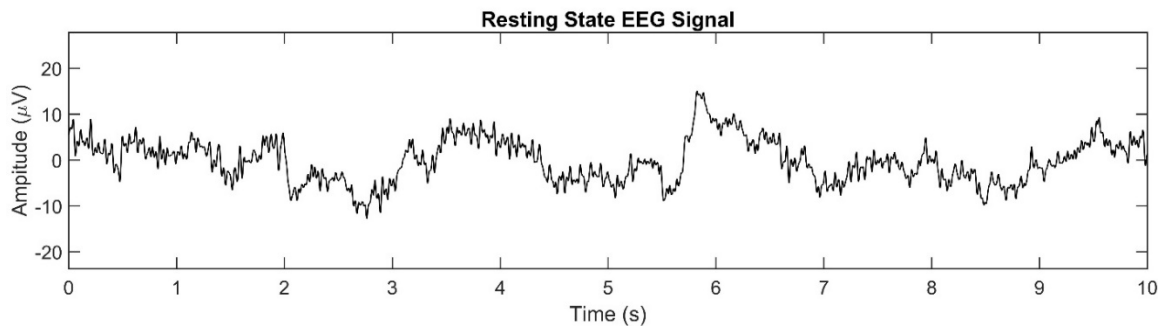


drawn every single pin of MSP430F5438 in logic design to external pin arrays to facilitate better debugging. The board also included an onboard USB and serial debugging ports.

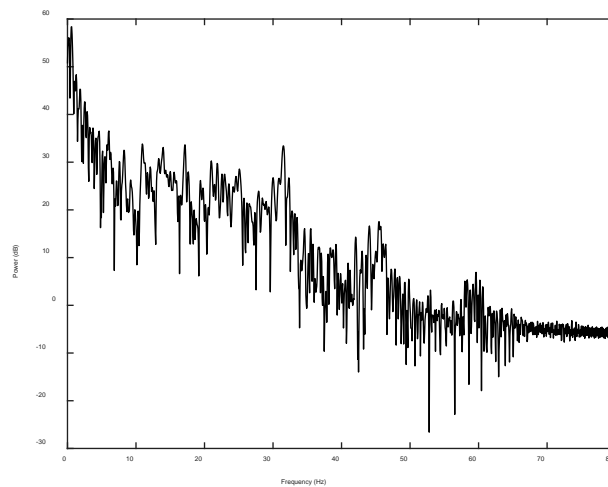


**Figure 28.** The PCB layout design and the produced board. (a) Screen shoot of the finalized two-layer PCB layout design. (b) The manufactured PCB based on the layout design file as shown in (a). (c) The working PCB with circuit components assembled and soldered.

The corresponding firmware for drivers and utilities was developed in IAR Embedded Workbench and uploaded to the hardware through the USB emulator connecting with onboard SPI interface. The board was tested to verify if the correct waveforms could be acquired. Two gold cup electrodes were connected to the bipolar recording inputs (IN1P & IN1N) of the ADS1299. At least 150 seconds of continuous EEG data were collected while the human subject sat in the neutral position. Figure 29 presents a 10-second length of the signal selected from the 150-second signal. The PSD of the 150-second signal is presented in Figure 30.



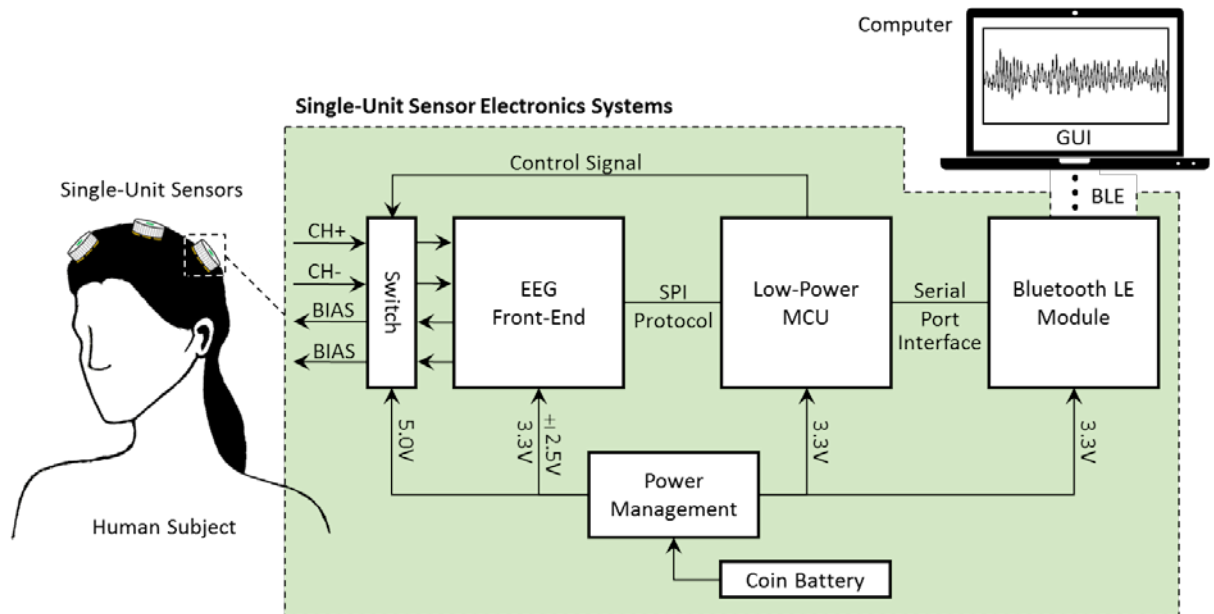
**Figure 29.** Raw EEG signal acquired using the circuit board presented in Figure 28 (c).



**Figure 30.** PSD plot of the 150-second EEG signal acquired from the board.

## 6.2 IMPROVED DESIGN

The new electronic system was then designed in a way to be integrated into the single-unit sensor as a unifying miniature piece. Therefore, the system required minimized hardware size and power saving features. In addition, compared to the prototype developed in Section 6.1, the current design also took into consideration of the close electrode separation in the single-unit sensor. Figure 31 depicts the functional block diagram for the sensor electronic system. Compared to previous design in Section 6.1, a switch module was implemented. Besides, the analog circuitry of bio-potential front-end (ADS1299) was configured differently to include a bias drive circuit. A more compact ATmega328p MCU replaced the original full-featured, but relatively size-occupying MSP430 MCU. The RN-42 Bluetooth module and its external circuitry were replaced by a smaller CC2541 Bluetooth LE module with power-optimized features.



**Figure 31.** Block diagram of the single-unit sensor electronics system (depicted within the green-color area). The communication of the system to a computer is through Bluetooth LE.

Specifically, at the input stage (electrode connecting interface) of the system, four 74HC4051 analog switches were configured to change the orientation of differential recording electrode pair dynamically. The remaining bias pair altered simultaneously via the switch. Therefore, the differential recording pair selectively adapted to the altering gradient of biopotential on human scalp, and therefore the maximum potential drop might be captured. The switch had a short input rise and fall time ( $\sim 500$  ns at 5 V voltage supply), low “on” resistance ( $\sim 50 \Omega$ ) and low leakage ( $\pm 8 \mu\text{A}$  maximum) at 5 V power supply. It also isolated the recording inputs to be directly connected to the amplifier. The switching mechanism can be carried out in many modes. For example, the switch could comply with a specific timing (e.g., every 30 seconds), or it could be manually controlled through PC. Alternatively, the voltage amplitude of each orientation could be compared once in a while for a decision to switch.

The raw signal subsequently entered the respective channels of EEG amplifiers. The ADS1299 bio-potential front-end was again adopted in this version of the design. While still adopting the same solution, the analog circuitry configuration was different. In the previous design, a reference channel was located somewhere far from bipolar recording channels. Meanwhile, the current implementation required the single-unit sensor’s four electrodes to be placed in very close proximity (20 mm for opposite electrodes, approximately 3.25 mm for adjacent electrodes). This recording setup potentially induced large common-mode interferences. An external bias electrode drive was implemented to suppress common-mode interference generated by power lines. The bias drive in amplifier circuit returned negative feedback of common-mode output signal to the bias electrode to improve rejection of the common-mode signal to the amplifier. The schematic of the ADS1299 and external circuits is presented in Figure 32. We utilized the TI ADS1299 Performance Demonstration Kit to configure the ADS1299 and its external circuitry. The

“daughter board” (the board sits on MMB0 Modular EVM motherboard) of the demonstration kit board implemented external bias drive, external oscillator, various voltage inputs, which were suitable for us to verify the hardware design of the single-unit sensor. All the configurable features equipped with the board were accessible via jumper settings. Every pin of the ADS1299 was wired to joint test action group (JTAG) on the board for fast prototyping.

For the MCU of the system, an Atmel picoPower ATmega328P 8-bit AVR [86] was utilized. The MCU sends the control signal to the analog switches, configured recording properties of ADS1299 bio-potential front-end, and interface with the Bluetooth LE module to wirelessly transmit the signal to PC. The 28-pin QFN package (with no pins extend outside the chip main body area) of this chip requires  $4.00\text{ mm} \times 4.00\text{ mm}$  of an area and 1.00 mm in height. The solution was suitable for long-term operation, as the active mode power consumption requires as low as 0.2 mA, the power consumption as the power-down mode goes to 0.1  $\mu\text{A}$ . An Arduino Pro mini development board configured with ATmega328p was utilized to quickly prototype the electronic system, as well as to develop drivers and utilities. The kit features onboard debugging interface, 3.3 V voltage level, 8 MHz onboard oscillator, and JTAGs to facilitate development and prototyping. The schematic of the MCU and external circuitry is presented in Figure 33.

The data transmission between the sensor and PC was realized by a Bluetooth LE module, which interfaced with ATmega328P MCU through the serial port protocol (SPP). Specifically, the TI “CC2541 SimpleLink 2.4 GHz Bluetooth LE and proprietary wireless MCU” was selected based on its minimal power consumption while maintaining a data rate that fully satisfies our EEG data throughput. The CC2541 and similar products in its series have been widely utilized in wearable and intelligent hardware applications targeting healthcare and life improvements, such as wearable activity trackers, smartwatches, and smart home applications. The TI CC2541 supports

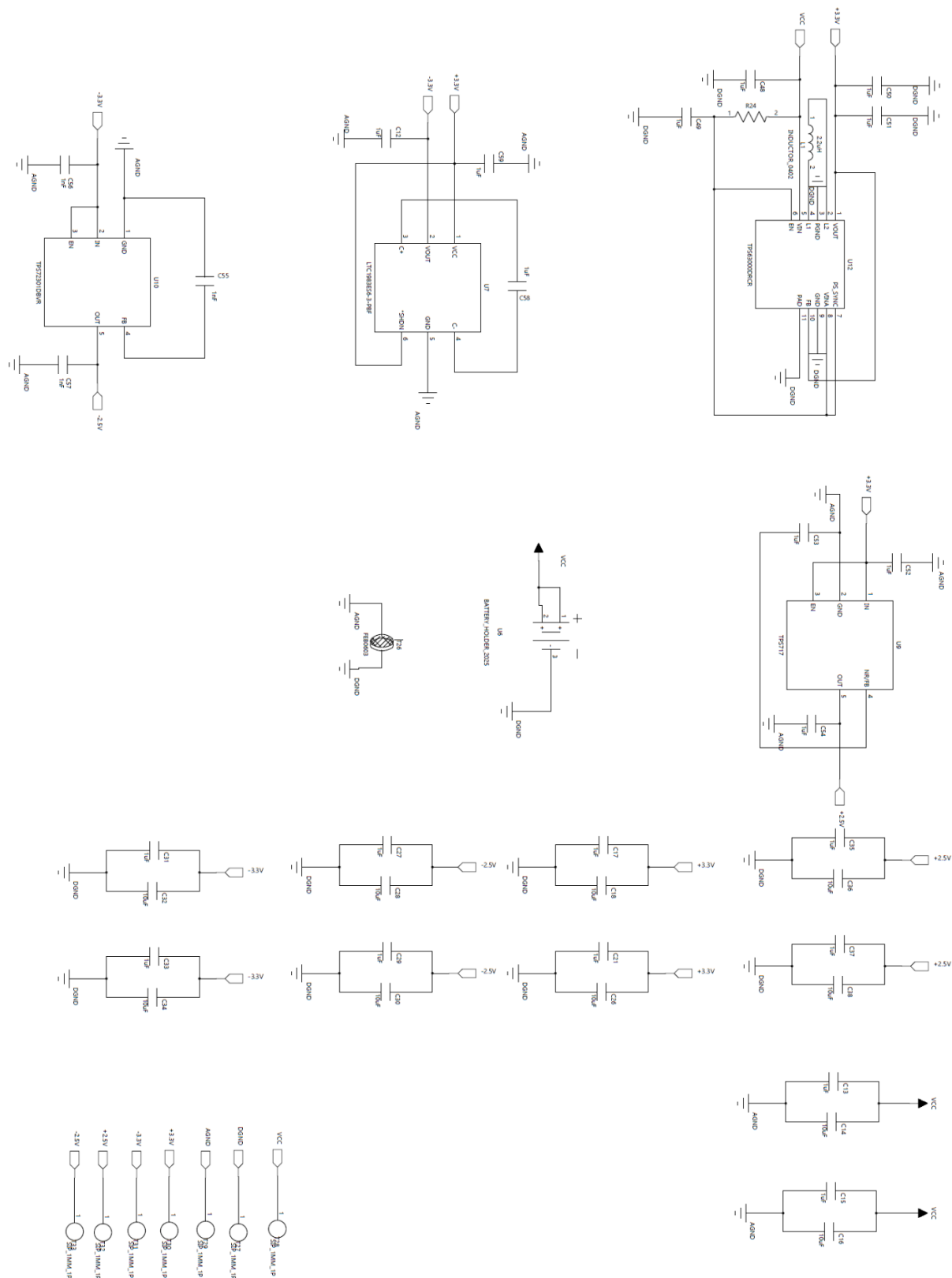
a data rate up to 2 Mbps. A market-available CC2541 Bluetooth LE module was adopted. The board was a whole wireless related function system integrated into a minimal postage stamp PCB. Within as small as 11.0 mm × 16.6 mm of space, a CC2541 chip, crystal oscillators, an integrated antenna, and many RCL components were densely assembled. This type of Bluetooth LE minimal system boards had been widely seen recently as a viable solution to integrate wireless capability to the current design more conveniently and professionally with less labor effort.

The battery power management circuitry in the sensor system regulated the input  $V_{CC}$  voltage coming out from a battery to multiple voltage levels (-2.5 V, 2.5 V, 3.3 V, 5 V, isolated digital and analog ground) suitable for each peripheral in the system. The analog switch utilized a high 5 V voltage to reduce “on” resistance and transition time. The bio-potential front-end utilizes  $\pm 2.5$  V for bio-polar supply biometric signal collection, as well as 3.3 V for the digital SPI interface. The 3.3 V was also designed for MCU and Bluetooth digitized signal. The regulated voltage to the digital part of the circuit helped to save the power consumption. It also avoided losing data frames for an extended length of time when battery energy decays, for the purpose to ensure the accuracy and integrity of the measurement results. It further stabilized the voltage in the system from fluctuation. The schematic of the power management circuitry is presented in Figure 34.









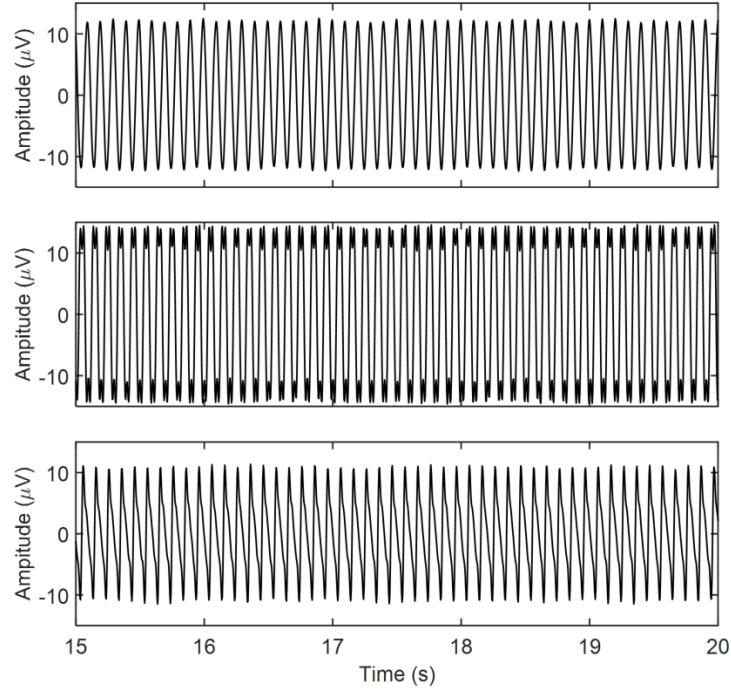
**Figure 34.** Schematic for the power management system.

The choice of component packaging was solely based of size minimization. For example, most of the passive electronic components utilized 0201 SMD packages (0.6 mm × 0.3 mm.) As for the choice of chips, BGA package was ideal once the sensor transferred into industrial fabrication stage. The detailed bill of materials (BOM) for making a single-unit sensor prototype, as well as the cost once entering a mass production state (assume more than 3,000 sensors were planned) are listed in Appendix D. As the cost of making high-precision multi-layer PCB was high, and board assembly environment was limited in our lab, we established a prototype platform using the development board described above with our firmware codes uploaded into the system.

After the construction of the prototype electronic system, the performance of the electronic system was examined. Signals were generated from a function generator, including sinusoidal, square, ramp, and simulated cardiac signals with different frequencies. The frequencies and voltages of the testing signals were set to be around 10 Hz and 10  $\mu$ V, which were similar to actual EEG signal acquired with close proximity electrodes in Section 4.3. Since the minimum peak-to-peak voltage scale by our particular function generator was 1 mV and was often contaminated with 60 Hz noise, a voltage divider circuit was utilized to divide a larger 500 mV of amplitude down to 10  $\mu$ V. The resistors used in the voltage divider circuit were 10 M $\Omega$  (10.22 M $\Omega$  actual measurement value) and 220  $\Omega$  (216  $\Omega$  actual measurement value). Therefore, the voltage yielded was:

$$500mV \times \frac{216\Omega}{216\Omega + 10.22M\Omega} \approx 10.57\mu V$$

The generator's two signal leads were connected to the electronic system's two differential inputs. Figure 35 below shows the acquired sinusoidal, square and ramp signal.



**Figure 35.** The electronic system acquired testing signals generated by function generator. Top panel: the recorded sine wave. Middle panel: the recorded square wave. Bottom panel: the recorded saw tooth wave.

The calibration signal verified the electronic system acquired and restored the signal same to input signal in terms of their amplitude and frequency. With this being verified, the electronic system was then utilized with the constructed single-unit sensor electrode structure to conduct human subject experiment.

## **7.0 EFFICACY DEMONSTRATION ON SINGLE-UNIT SENSOR**

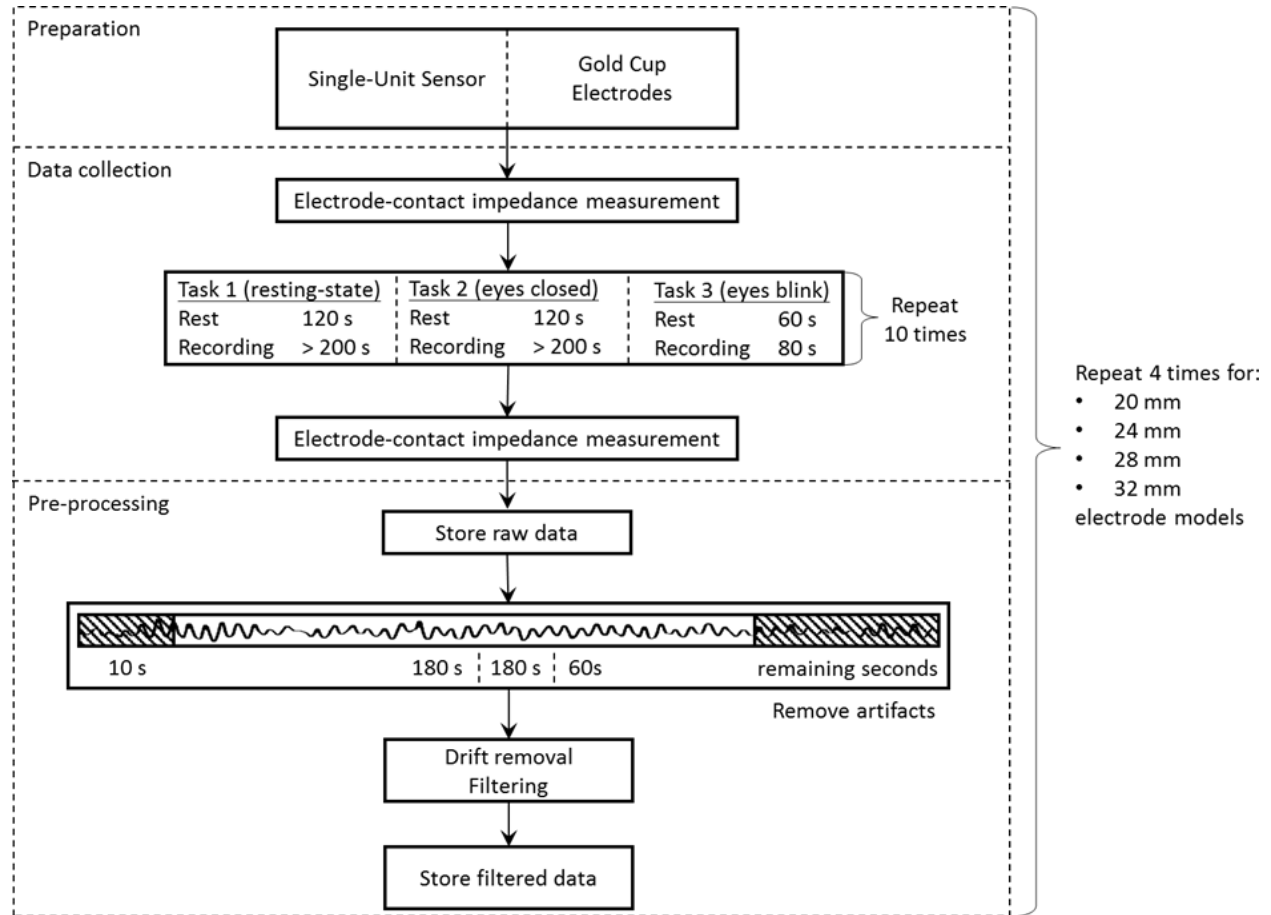
### **7.1 HUMAN SUBJECT EXPERIMENT**

With the construction of the electronic system and the electrode structure, the single-unit sensor prototype was evaluated on a human subject. This could proceed with the series validation questions answered in previous chapters. The experiments aimed to demonstrate whether the single-unit could acquire EEG on human subjects, one step away from demonstrating its efficacy in detection of the epileptic seizure signals. The cup electrodes (the current gold standard) was utilized as a benchmark for single-unit sensor performance evaluation.

The final design demand (the 20-mm-diameter single-unit sensor) was approached by incrementally step forward from a safe and certain assumption. Previously, both theoretical and computational investigations demonstrated that the arc-shaped electrodes could acquire bio-potential signals. Based on these investigations, an experimental proof is presented in this chapter. The study was approved by approved by the University of Pittsburgh Institutional Review Board (IRB). The human subject signed the consent form prior to the experiment. Although only one human subject participated in the experiment, the variation between subjects were expected to be small based on previous study of EEG. The experiment started from a larger 32-mm-diameter single-unit sensor model, and incrementally shifted to the next models with smaller dimensions (28 mm, 24 mm, and eventually to 20 mm) with positive experimental evidence on the current one. Right before conducting each experiment, the electrode-skin contact impedance was measured. The impedance was first measured between two differential input channels, and then

each input channel to the mutual bias channel (by connecting two opposite channels). These impedance values were logged into the Appendix D.

### 7.1.1 Experiment Protocol



**Figure 36.** Flow of the experiment procedures.

The protocol of the human subject experiment is illustrated in Figure 36. During the experiment, the human subject was instructed to perform three distinct tasks:

- 1) Sits still in neutral position with natural eyes blink and minimal movement (Task 1).
- 2) Similar to Task 1, but keep eyes closed (Task 2).

3) Similar to Task 1. The electrodes were placed differently than previous tasks (Task 3).

During Tasks 1 & 2, the sensor was placed at the right occipital region O2 site in the 10-20 system. For Task 3, the right front parietal region FP2 site was selected as the recording site. The choice of placement sites depended on previous knowledge about information processing in the brain regions. For example, the primary visual cortex (V1) that governs the processing of visual stimuli was located in the occipital lobe of the brain, and therefore the O2 site was chosen as the recording site.

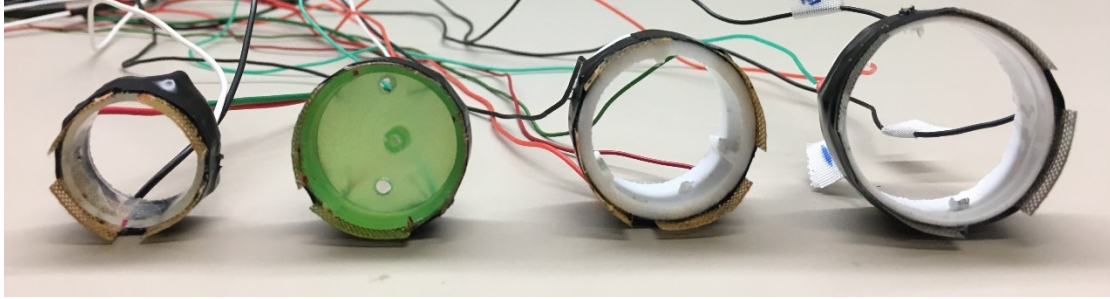
As already mentioned previously, among four electrodes of the single-unit sensor, one pair of electrodes at opposite locations was connected to the differential input terminals of the amplifier, while the other pair of electrodes was connected to the mutual bias buffer in the electronics to suppress common-mode signals in the environment.

While performing each task, at least ten pieces of data were collected using a single-unit sensor model. Each data was a continuous EEG recording of at least 200 seconds. There was a minimum 120-second break between consecutive sessions. Once a session of ten recordings was concluded, impedance values were measured once again, and raw data saved with explanatory notes. Subsequently, Task 2 and 3 were conducted in the same manner. Following the above process, the same procedures were again executed, with the substitution of the single-unit sensor to the gold cup electrodes of the same dimension. The single-unit sensor and the standard gold cup electrodes were compared side by side at the same installation sites.

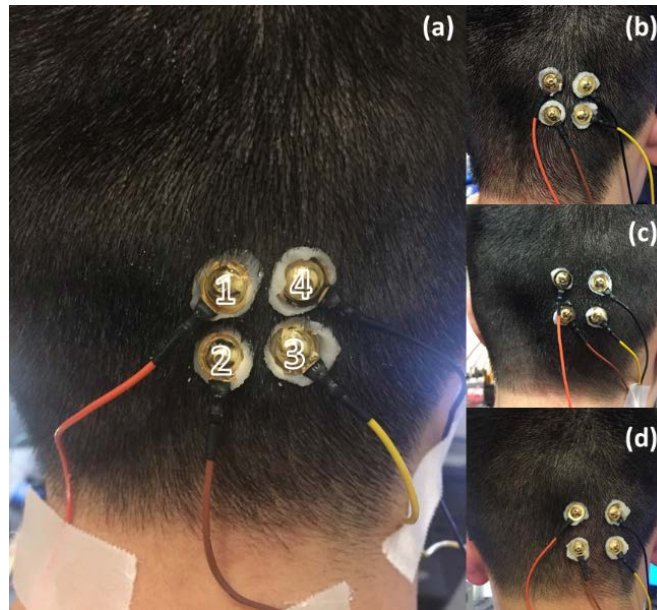
The feasibility of the 32-mm-diameter single-unit sensor model was validated first. Subsequently, 28-mm, 24-mm, and 20-mm-diameter single-unit sensor diameter were evaluated and validated. Figure 37 shows four single-unit sensor models. Therefore, the entire experiment procedures were repeated at least four times for each dimension of single-unit sensor model.



Simultaneously, the four gold cup electrodes with diagonal distances of 28 mm, 24 mm, and 20 mm were implemented for performance comparison.

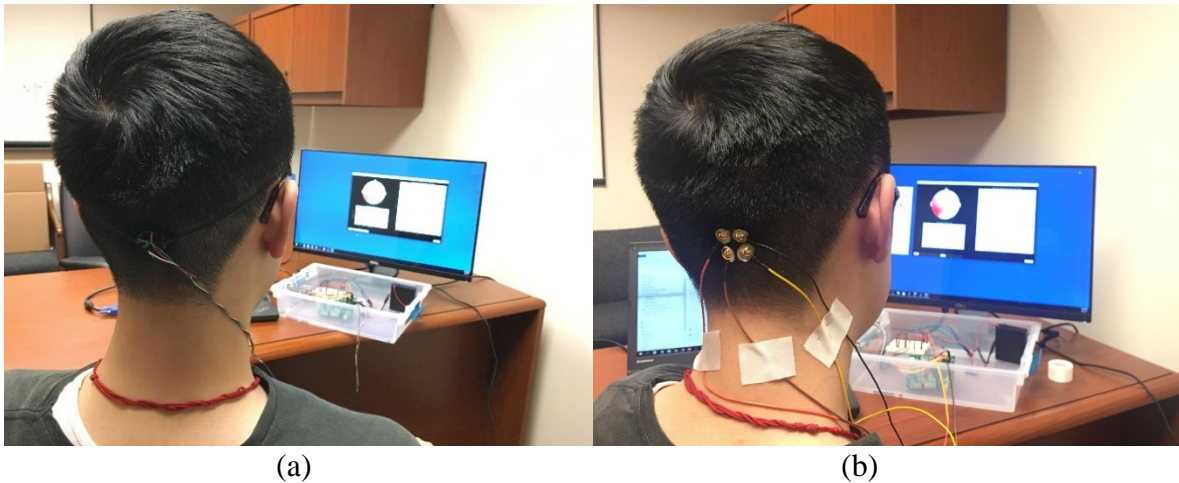


**Figure 37.** Four single-unit sensor electrode structure prototypes. Displayed from left to right, they have diameters of 20 mm, 24 mm, 28 mm, and 32 mm, respectively.



**Figure 38.** Placement configuration of the four gold cup electrodes. The electrodes had diagonal separations of (a) 20 mm, (b) 24 mm, (c) 28 mm, and (d) 32 mm. As default setup, the electrodes 1 & 3 were utilized as differential inputs, and the electrodes 2 & 4 were connected together as a mutual bias channel.

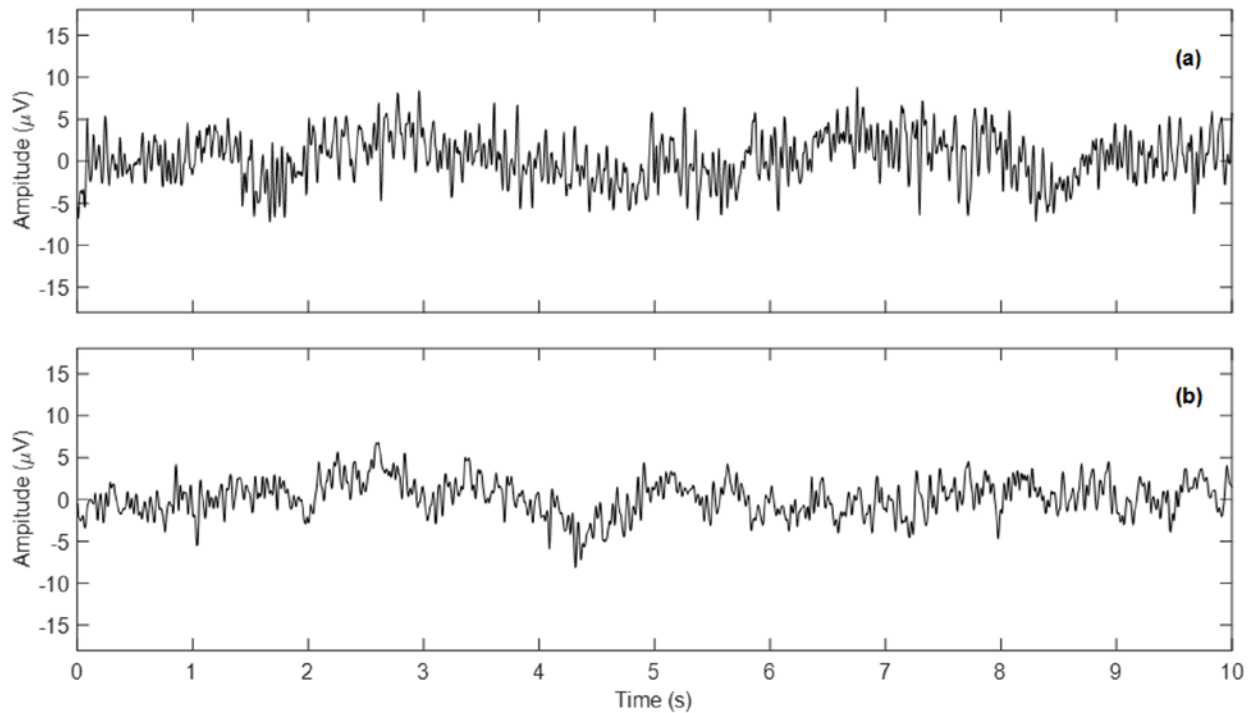
The raw datasets were generated as decimal format time series sampled at 250 Hz. A MATLAB script was developed to pre-process raw datasets. Specifically, the first ten seconds of each time series was truncated to remove rapid amplifier saturation at electronic system power on, and to eliminate possible motion artifacts. The following 180-second length of the signal was extracted. A baseline drift removal algorithm adopting adjacent 500-sample-point sliding window was applied to signal to remove baseline drift to a neutral level. Subsequently, a 1 Hz high-pass filter, a 30 Hz low-pass filter, and a 60 Hz notch filter, all being the third order Butterworth Infinite Impulse Response (IIR) filters, were utilized to remove DC drift and powerline noises.



**Figure 39.** EEG recording environment using the single-unit sensor prototype. The experiment sessions use (a) the 20-mm-diameter single-unit sensor, and (b) the gold cup electrodes with 20-mm diagonal separation. Overall, four comparison groups with different dimensions were set up during data collection.

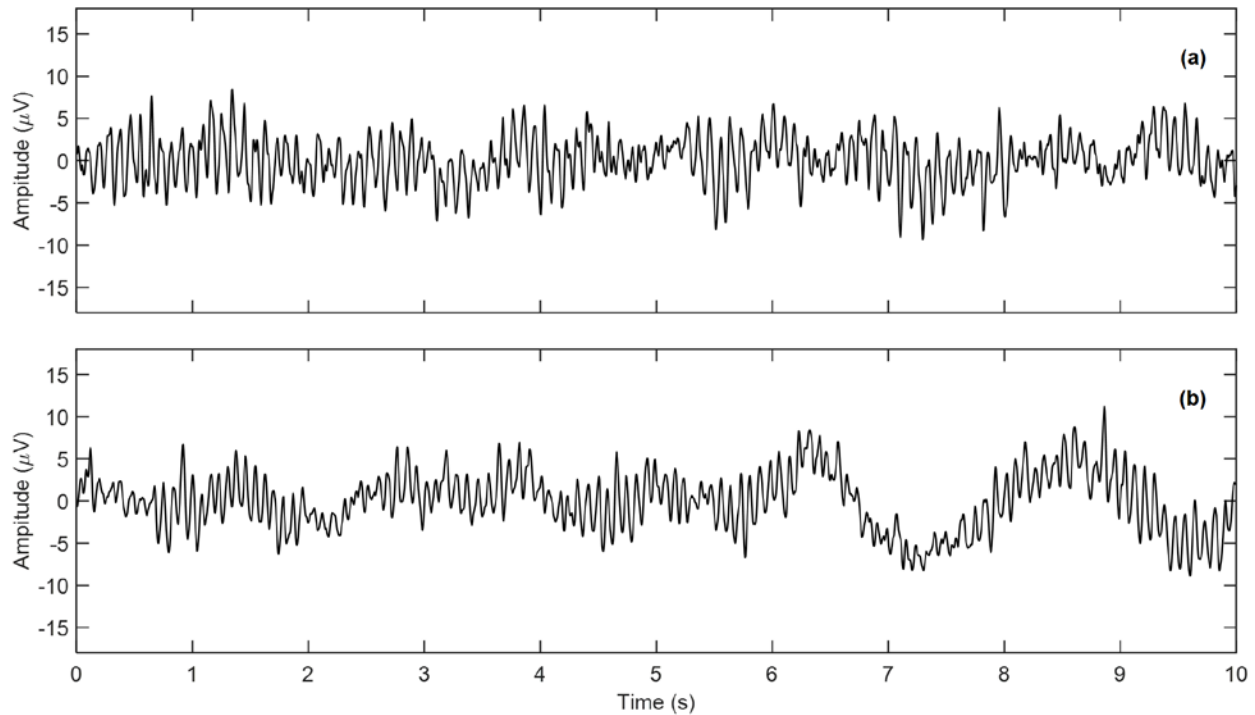
### 7.1.2 Experimental Results

In all single-unit sensor models, including the smallest 20-mm-diameter model, EEG waveforms could be clearly observed. Figure 40 (a) illustrates a 10-second segment of EEG signal acquired from the 20-mm-diameter single-unit sensor while the human subject performed Task 1. Transient waves with approximately  $10\ \mu\text{V}$  to  $15\ \mu\text{V}$  peak-to-peak amplitude can be observed. Figure 40 (b) presents the signal collected using the gold cup electrodes with diagonal separation of 20 mm. The signal shows comparable patterns and amplitude to the 20-mm-diameter single-unit sensor signal presented Figure 40 (a).



**Figure 40.** The EEG signals acquired while performing the Task 1. The signals were recorded using: (a) the 20-mm-diameter single-unit sensor, and (b) the gold cup electrodes with 20-mm diagonal separation.

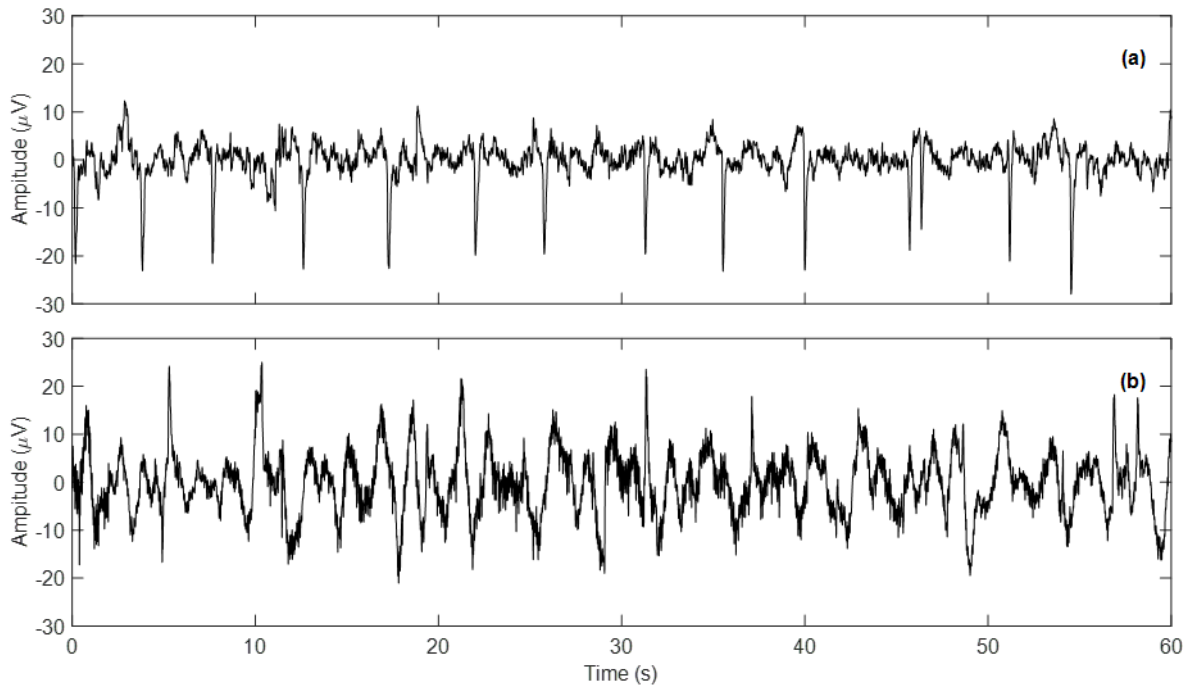
A typical segment of EEG signal collected from 20-mm-diameter single-unit sensor model while performing the Task 2 is presented in Figure 41 (a). The smooth oscillation waves with an occurrence of approximately 8 – 13 oscillations per second were identified. The signal appeared to be similar to the signal collected using the gold cup electrodes with a diagonal separation of 20 mm. A typical segment of the signal from the gold cup electrodes was presented in Figure 41 (b). The two signals showed comparable alpha wave oscillations with amplitudes of approximately 10  $\mu\text{V}$  peak-to-peak.



**Figure 41.** The EEG signals acquired while performing the Task 2. The signals were recorded using: (a) the 20-mm-diameter single-unit sensor, and (b) the gold cup electrodes with 20-mm diagonal separation.

Additional results were obtained while the human subject performed the Task 3. While performing the Task 3, the single-unit sensor and cup electrodes were placed on the FP2 site of the

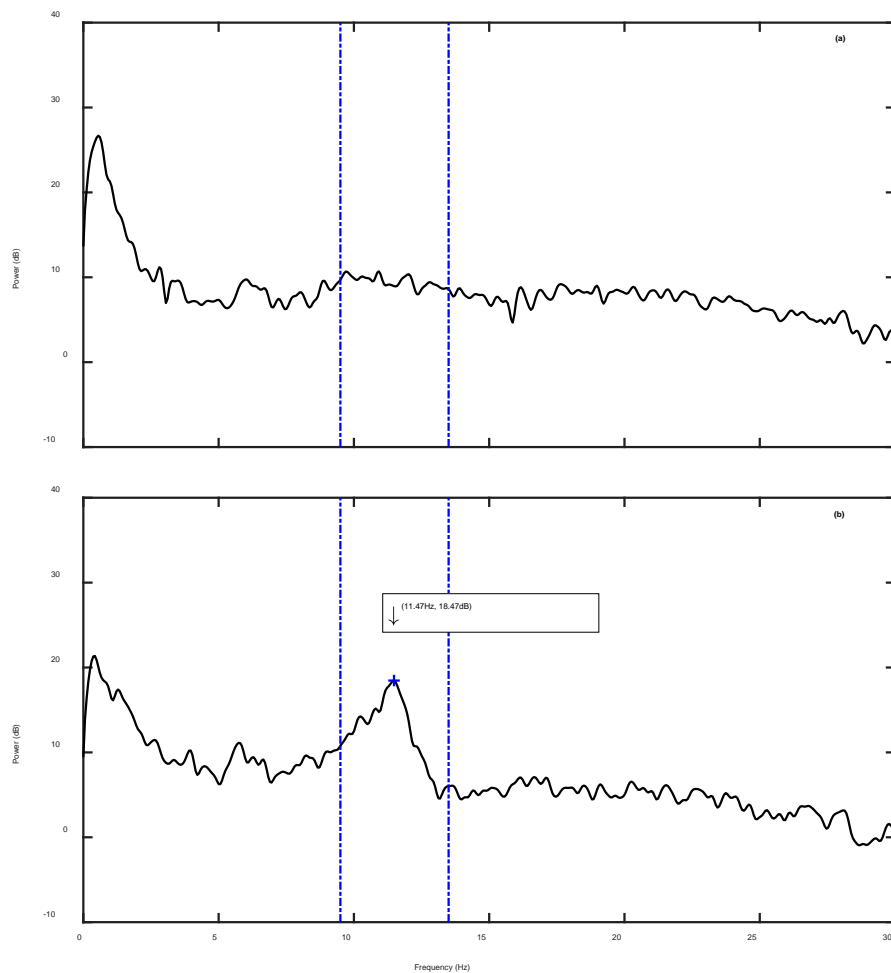
scalp. In Figure 42, the two typical segments of signals are demonstrated. In the top panel (a), the signal from the 20-mm-diameter single-unit sensor contained intermittent downward spikes. These spikes depicted the natural eyeblink activities. The signal also showed some baseline noise. In the bottom panel (b), the signal recorded from the gold cup electrodes with a diagonal separation of 20 mm was contaminated with heavier baseline noises. Although periodic eyeblink signals could be observed, it appeared to be smaller than what has been observed in the top panel (a).



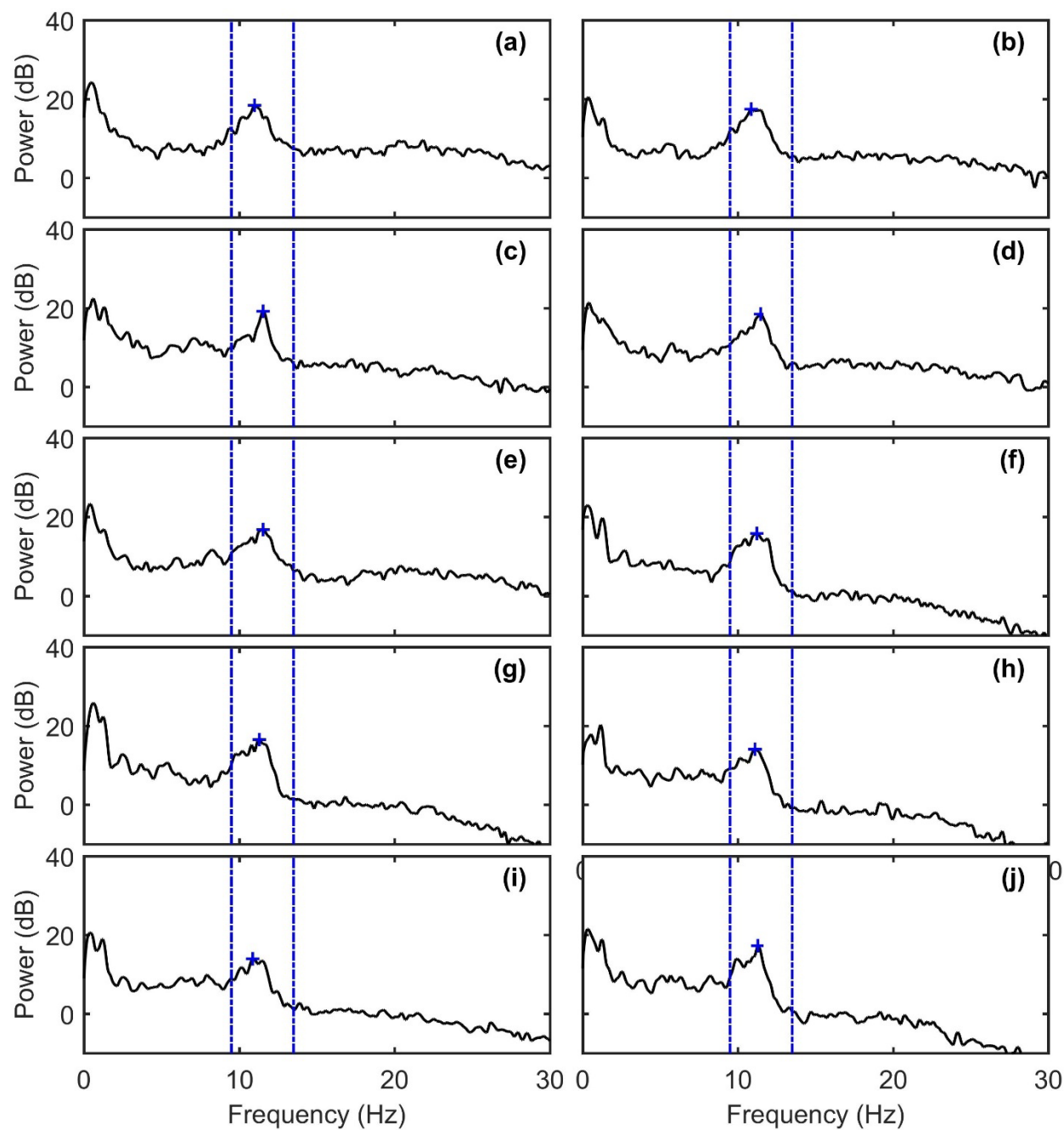
**Figure 42.** The EEG signals acquired while performing the Task 3. The signals were recorded using: (a) the 20-mm-diameter single-unit sensor, and (b) the gold cup electrodes with 20-mm diagonal separation.

Frequency domain analysis was subsequently carried out on raw signal. Firstly, the Welch's method power spectral density (PSD) was performed on acquired signals. The first comparison carried out on signals collected using the 20-mm-diameter single-unit sensor model

while the human subject performed the Tasks 1 (Figure 43 (a)) and the Task 2 (Figure 43 (b)). As showed in Figure 43 (b), a noticeable spectral component appeared within the alpha wave frequency band, which was correlated with the fact that such alpha wave signal was induced by eye closure. While in Figure 43 (a), such signal characteristic was not observed, which correlated with the fact that the resting state did not induce the alpha wave signal.



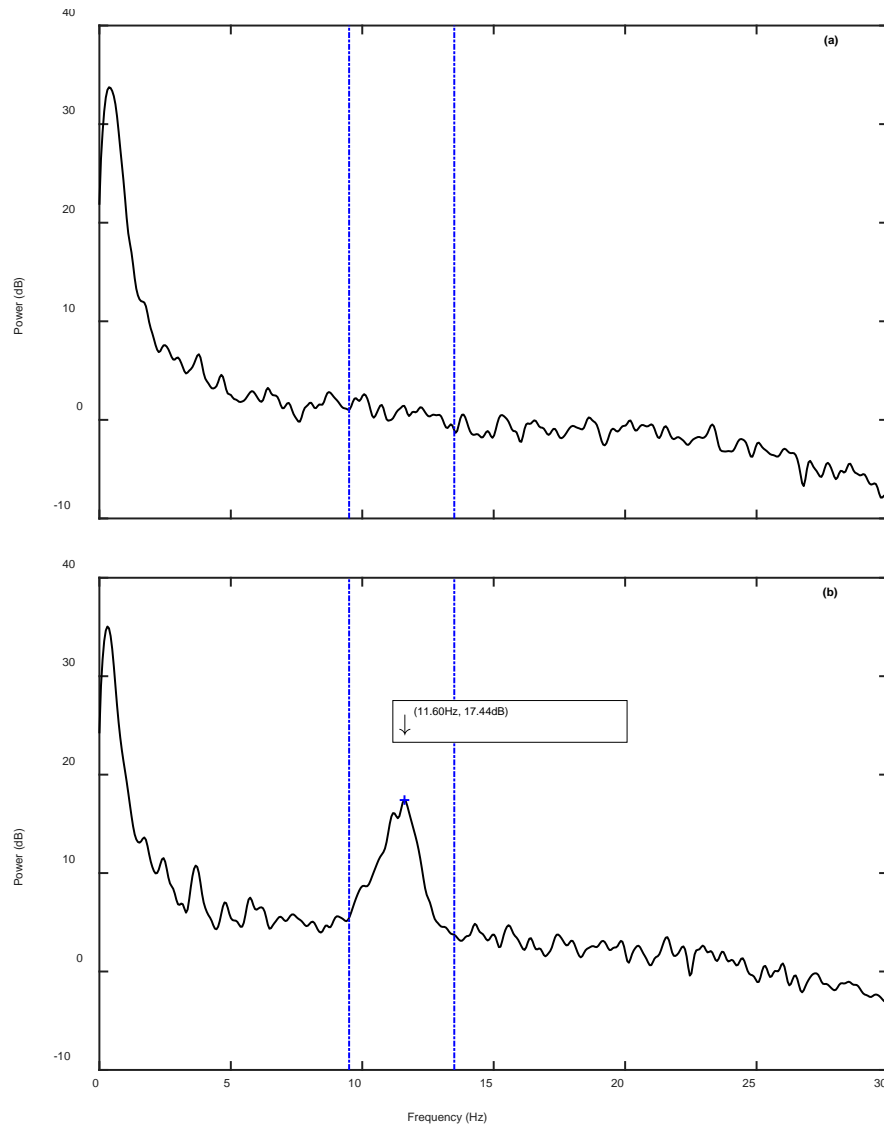
**Figure 43.** PSD plots of two experiment sessions using the 20-mm-diameter single-unit sensor. Two sessions were recorded while the human subject (a) performs the Task 1, and (b) performs the Task 2. The area between the two blue-color dash-dot lines depicts the alpha wave frequency band between 9.5 Hz – 13.5 Hz. The blue “+” mark in (b) represents the local maximum in the alpha frequency band, with frequency and power value tagged above the mark.



**Figure 44.** Spectral plots of data recorded using the 20-mm-diameter single-unit sensor. The area between blue dash-dot line depicts the alpha wave frequency band between 9.5 Hz – 13.5 Hz. The blue “+” mark represents the local maximum in the region.



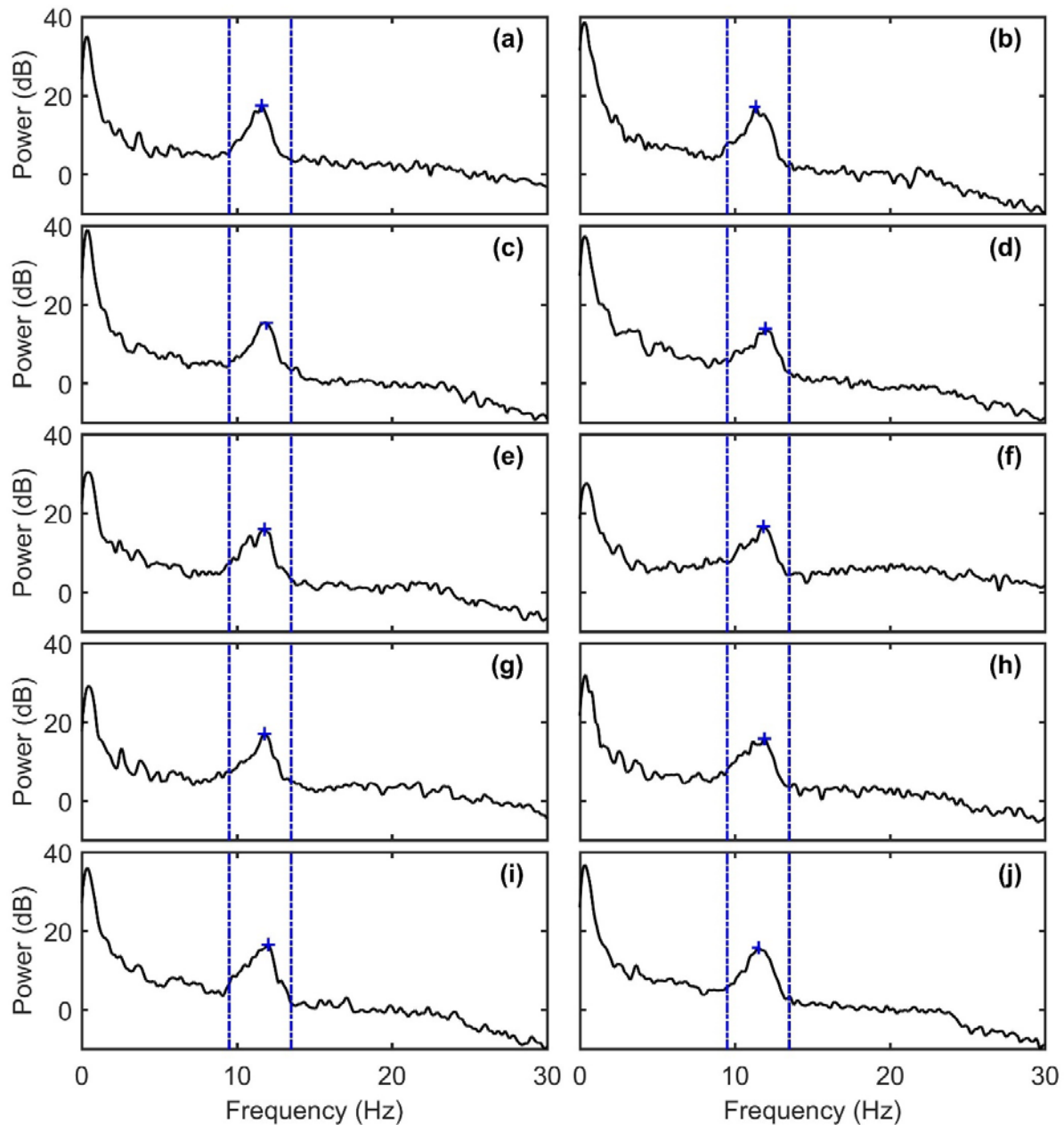
Subsequently, the same frequency domain analysis approach was applied to the dataset acquired using the traditional gold cup electrodes with a diagonal separation of 20 mm while the human subject performs the Tasks 1 (Figure 45 (a)) and the Task 2 (Figure 45 (b)).



**Figure 45.** PSD plots of two experiment sessions using gold cup electrodes. Two sessions were recorded while the human subject (a) performs the Task 1, and (b) performs the Task 2. The area between the two blue-color dash-dot lines depicts the alpha wave frequency band between 9.5 Hz – 13.5 Hz. The blue “+” mark in (b) represents the local maximum in the alpha frequency band, with frequency and power value tagged above the mark.

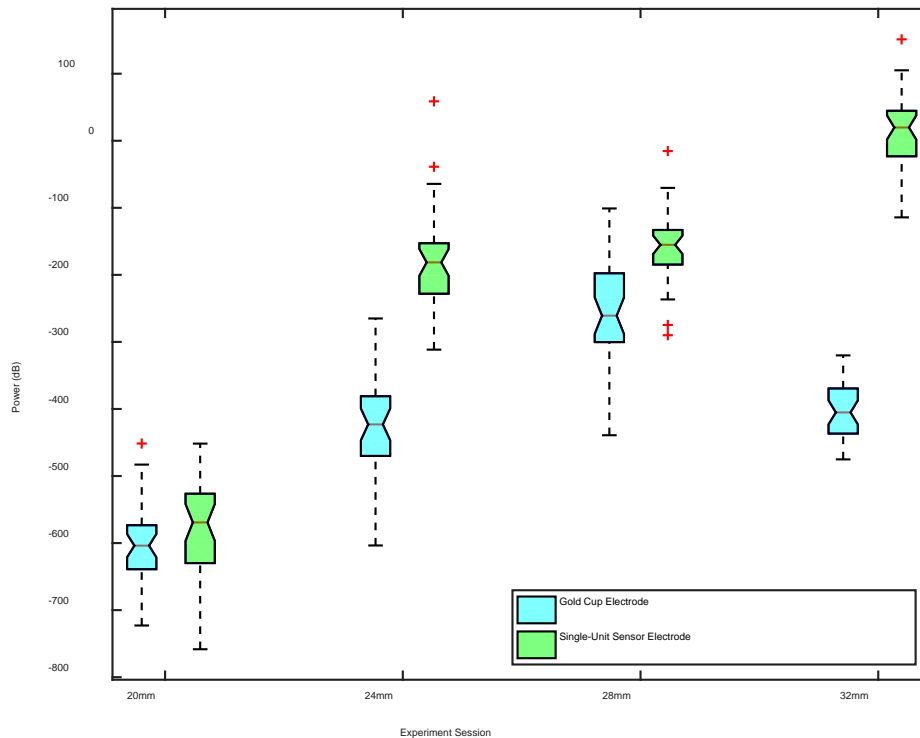


In all the ten Task 2 sessions, apparent peaks can be observed clearly. This demonstrates the consistency of the sensor in collecting characteristic EEG signals.



**Figure 46.** Spectral plots of data recorded using the gold cup electrodes with 20-mm diagonal separation. The area between blue dash-dot line depicts the alpha wave frequency band between 9.5 Hz – 13.5 Hz. The blue “+” mark represents the local maximum in the region.

The signal energy for alpha frequency band was calculated for each experimental session. The maximum and minimum values among ten sessions were discarded as the statistical outliers. The remaining signal energies were averaged and presented in Figure 47. Observed from the figure, it seems the separation distance of bipolar recording electrodes was a factor to impact the voltage amplitude of the collected signal. With an increase of electrode separation, a tendency of a stronger amplitude of energy can be observed. In all cases, comparable or relatively stronger signal energy could be captured from the single-unit sensor. For the 32-mm gold cup electrode group, the small signal energy contradicts the increasing trend. This could happen for various reasons, including motion artifacts, improper electrode installation, and loosen electrodes.



**Figure 47.** Alpha frequency band signal energy comparison. The comparisons were carried out between single-unit sensor and gold cup electrodes placed at same geometric scale, and four geometric scales in total.

**Table 4.** Gold cup electrode designated geometric scale and actual measurement

| Diagonal distance | Electrode pair distance (mm) |       |       |       |                  |                  |
|-------------------|------------------------------|-------|-------|-------|------------------|------------------|
|                   | C1-C2                        | C2-C3 | C3-C4 | C4-C1 | C1-C3 (diagonal) | C2-C4 (diagonal) |
| <b>20 mm</b>      | 15.0                         | 14.1  | 14.0  | 15.0  | 20.0             | 21.0             |
| <b>24 mm</b>      | 16.5                         | 16.5  | 16.0  | 17.0  | 24.0             | 24.0             |
| <b>28 mm</b>      | 20.0                         | 19.0  | 20.0  | 20.0  | 28.0             | 28.0             |
| <b>32 mm</b>      | 23.0                         | 22.0  | 22.0  | 22.5  | 32.5             | 32.3             |

Regarding impedance values, based on more than 48 measurements, we found that the electrode-skin contact impedance of the single-unit sensor electrode structure was comparable to the gold cup electrodes. For most measurements, the arc-electrode impedances were below 50 k $\Omega$ . In some cases, the impedances were in the range between 5 – 10 k $\Omega$ . The lower impedances were typically observed when recording on forehead locations. The variation of the impedance depends on many factors including installation quality, skin condition and the quality of the prototype constructed.

Regarding the accuracy of installation, the single-unit sensor had a higher accuracy because its inter-electrode distances were fixed. For future versions of the product, an elastic band to assist faster/easier identification of installation site and secure fixation could be considered. Further, the gel/paste applied to the gold cup electrodes might overlap with adjacent ones, especially when the recording configuration was very close (e.g., 20 mm session). Therefore, the actual discrepancy due to electrolyte conduction might be larger. In terms of installation time, the time to install arc-shape electrodes was usually between 5 – 30 seconds, including impedance testing, while the installation time for the gold cup electrodes was much longer.

During the human subject experiment, the experiment protocol (as illustrated in Figure 36) was conducted for both the single-unit sensor and the gold cup electrodes. We made inter-group comparisons of EEG signal in both time and frequency domains. The series of results generated

from our experiments in combination with previous tests provided sufficient pieces of evidence that the single-unit sensor was able to acquire EEG signal comparable to the gold cup electrodes.

## **7.2 INDIRECT DEMONSTRATION FOR EFFICACY VALIDATION**

The investigations presented in previous sections have shown the feasibility of the single-unit sensor in acquiring EEG as demonstrated using the alpha wave as a characteristic signal. The remaining gap in knowledge was the efficacy of the single-unit sensor in detecting epileptic seizures for application to emergency medicine, which has been described at the beginning of this dissertation.

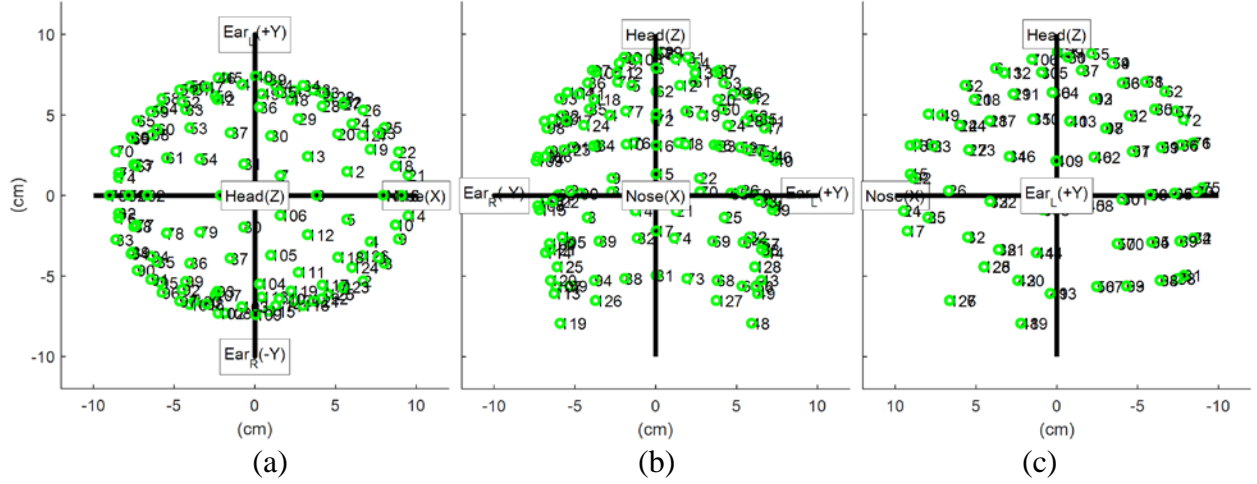
### **7.2.1 Rationality of Validation Study**

To investigate such gap in knowledge, an intuitive approach was to conduct a pilot test on critically ill patients undergoing epileptic seizure disorder management in ICUs or EDs. However, it was not practical to use early-stage prototype medical devices in clinical circumstance on critically ill patients. Therefore, a method of indirect proof-of-concept was carried out as an alternative validation approach based on the investigations conducted in the above two sections:

- 1) In Section 5.1 above, the implementation of a fast computing algorithm in Monte Carlo simulation analytically demonstrated the overall quantitative performance of the single-unit sensor electrode structure was comparable to that of the gold-plated cup electrodes employing standard 10-20 international mapping.

- 2) Furthermore, in Section 7.1 above, human subject experiments established equivalency between the single-unit sensor and the standard gold cup electrodes at the same geometric scale on actual human subject. At the same electrode sites and configurations, the EEG acquired using single-unit sensor electrode structure during multiple tasks were comparable to that of the traditional gold-plated cup electrodes.

If further evidence could be provided demonstrating the actual clinical epileptic signal acquired using the configuration identical to that of the single-unit sensor, it was equivalent to demonstrate that the signal can be acquired by single-unit sensor indirectly. The system employing 10-10 system (128-channel) had on average the separation of two adjacent electrodes similar to the separation of recording electrodes in the single-unit sensor. Therefore, an EEG dataset obtained from a deidentified 8-year-old epilepsy patient was utilized. The dataset included 128 channels of 80-second length EEG signal and other recording information including the electrode locations in 3D cartesian coordinate (Figure 48). The dataset was acquired from a HydroCel Geodesic Sensor Net (HCGSN) EEG system manufactured by Electrical Geodesics, Inc. (EGI) USA. All the channel data were initially referenced to a common mastoid location (channel Cz) during the recording. From the raw time series, at least five segments of signals containing epileptic seizure signals were identified, each segment with two to three seconds in length.



**Figure 48.** Three views of 128 channel locations in 3D space from (a) top, (b) front, and (c) left side of the 3D head model.

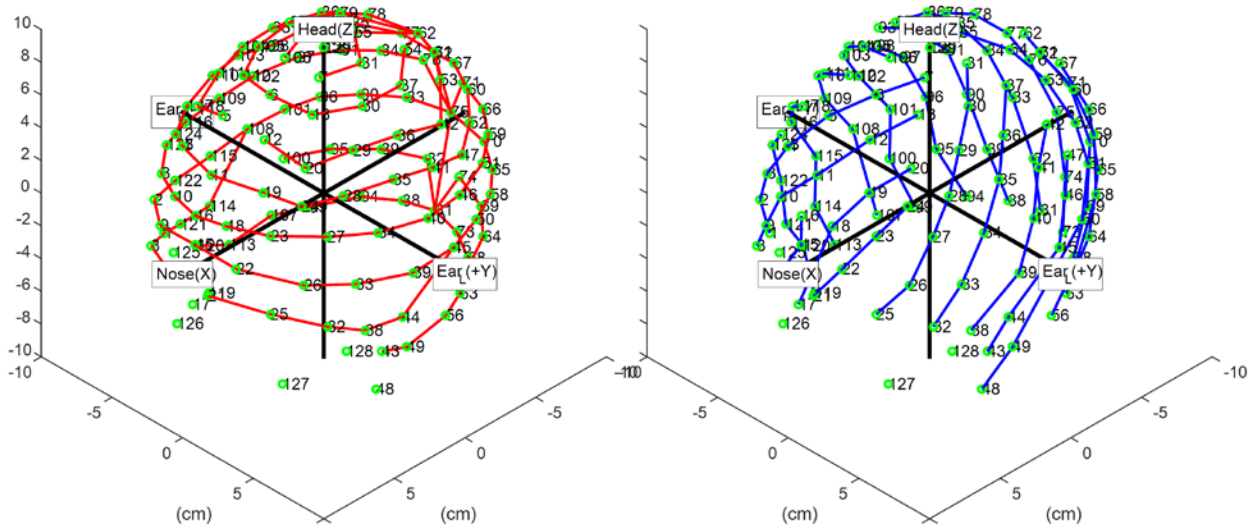
### 7.2.2 Reference Conversion to Bipolar Montage

The 128-channel EEG data were recorded using the Cz referential (monopolar) montage. For example, the signal at any channel among all 128 channels was recorded against a mutual reference Cz. The potential was then computed by the subtraction of the channel to the mutual Cz. Meanwhile, in the single-unit sensor, differential voltages were captured by two electrodes 20 mm apart. This configuration was similar to the bipolar montage recording. Thus, the two adjacent recording channels, Ca and Cb for instance, could be used to compute the potential difference  $Ca - Cb$  without Cz.

We needed to manage the equivalent comparison between the 128-channel EEG dataset to the single-unit sensor under the same montage. Thus, the 128-channel data adopting referential montage was re-referenced to the bipolar montage. The montage re-reference could be done using the re-formatting equation as follow:

$$(Ca - Cz) - (Cb - Cz) = Ca - Cb \quad (16)$$

In the Equation (16), Ca and Cb were the two adjacent electrode sites on the scalp. The reformatted dataset closely imitated the recordings of single-unit sensors over the entire scalp. Based on such equivalency, if the feasibility of detecting epileptic seizure from the newly formed bipolar recording electrode pairs could be demonstrated, it indirectly demonstrated the single-unit sensor that employed the identical electrode configuration. The subtractions of the adjacent electrodes could either follow longitudinal or transverse directions to follow the gradient of bio-potential on the human scalp as shown in Figure 49.



**Figure 49.** Established adjacent bipolar recording pairs following longitudinal orientation (left panel) and transverse orientation (right panel).

The example indirect demonstration was made by selecting the seven adjacent recording sites at the longitudinal direction from temporal lobes in the left hemisphere. Namely, the sites were C22 (FP1), C23 (AF3), C24 (F3), C29 (FC3), C36 (C3), C42 (CP3), and C52 (P3).

**Table 5.** Referential montage recording pairs

| <b>Channel</b> | <b>Derivation</b> |
|----------------|-------------------|
| C22            | FP1 - Cz          |
| C23            | AF3 - Cz          |
| C24            | F3 - Cz           |
| C29            | FC3 - Cz          |
| C36            | C3 - Cz           |
| C42            | CP3 - Cz          |
| C52            | P3 - Cz           |

The bipolar recording pairs of the adjacent electrodes listed in Table 5 were formed by subtractions of channels in series from the top of the table to the bottom. The subtractions were computed based on Equation (16). As results, the bipolar recording pairs were yielded as shown in Table 6. The channels were connected in chain longitudinally in the temporal lobe of the left hemisphere.

**Table 6.** Bipolar montage recording pairs derived from Table 5

| <b>Channels</b> | <b>Derivation</b> |
|-----------------|-------------------|
| C22 - C23       | FP1 - AF3         |
| C23 - C24       | AF3 - F3          |
| C24 - C29       | F3 - FC3          |
| C29 - C36       | FC3 - C3          |
| C36 - C42       | C3 - CP3          |
| C42 - C52       | CP3 - P3          |

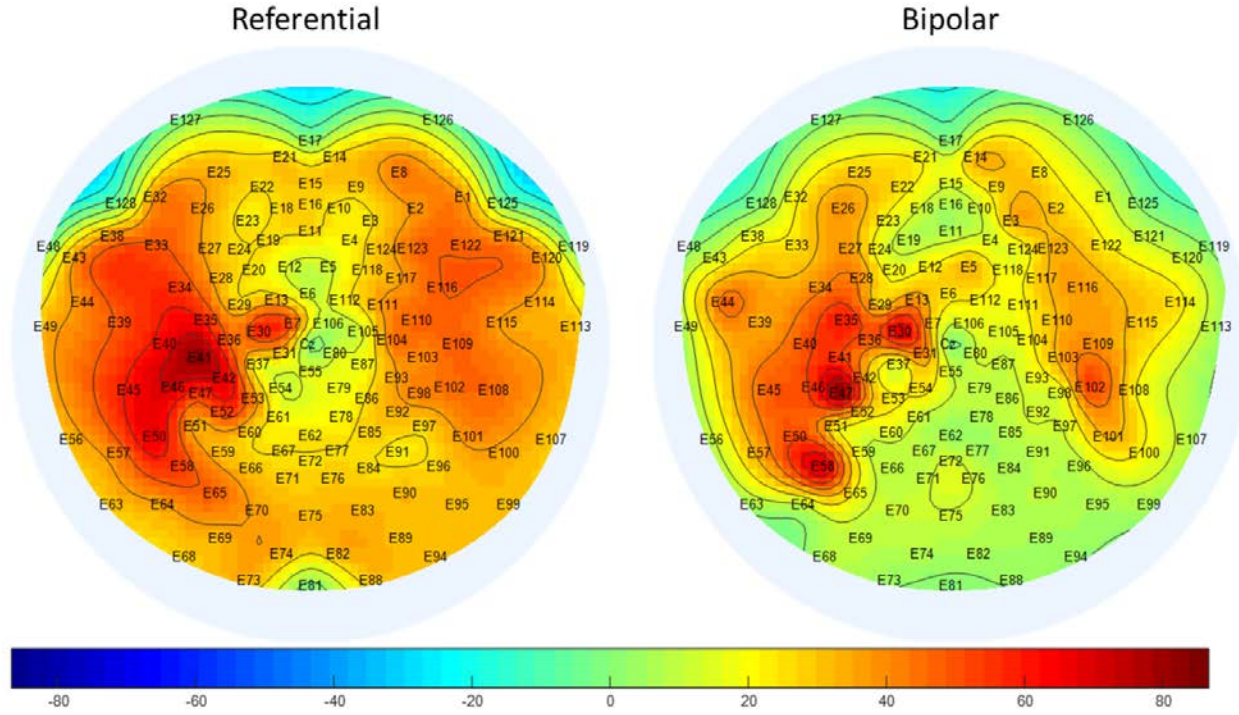
### 7.2.3 Experimental Results

A three-second piece of EEG signal containing epileptic seizure event was selected among identified segments epileptic seizure signal. Figure 50 shows the topographic energy maps of the



three-second signal. The topographic energy maps were plotted using MATLAB software EEGLAB toolbox [90] (version 14.0) developed by Swartz Center for Computational Neuroscience (SCCN). The left panel illustrates the topographic map of the monopolar (referential) recording referencing the mutual channel Cz. The right panel illustrates the topographic map of the bipolar recording (longitudinally subtracted as shown in Figure 49 (a)).

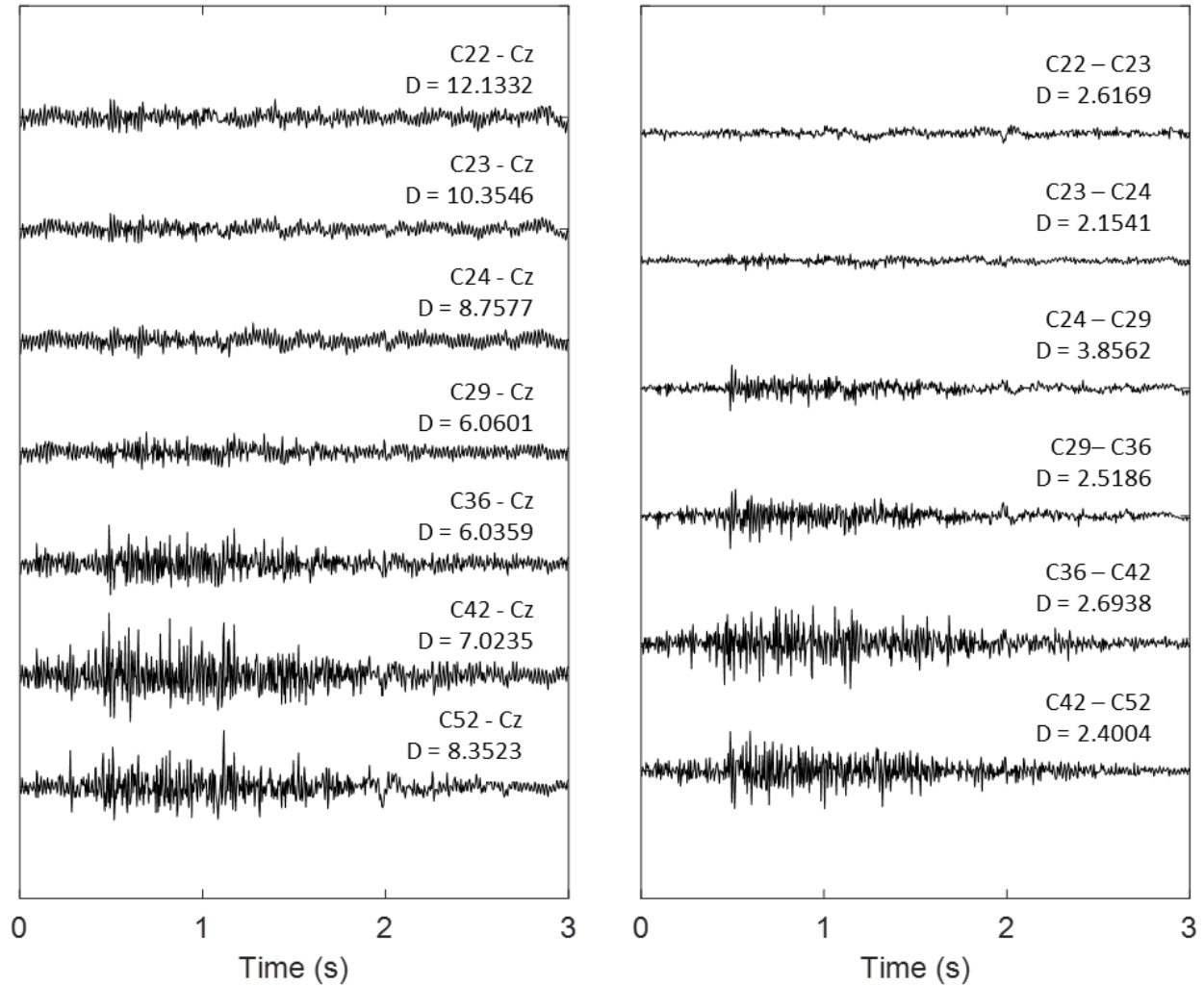
It has been observed that from both topographic maps that stronger amplitudes of signals were accumulated around the temporal lobe in two hemispheres. Particularly, in the left panel, two foci in left hemisphere could be observed at the electrode site 41, as well as in between electrode sites 7 and 30. This indicated that the signals recorded from these electrodes had higher signal energy. In the right hemisphere, the signal tended to be stronger between the electrode site 116 and 122, although the strength was not as strong in the left hemisphere. Interestingly, in the right panel, the locations of foci were different. In the left hemisphere, foci were observed at the electrode site 30, 47, and 58. Both locations and number of foci were different from the referential montage. In the right hemisphere, the location of strongest signal energy was found at the electrode site 102, which also differed from the observations in the referential montage.



**Figure 50.** Topographic energy maps of the epileptic EEG signals recorded via (a) Cz referential montage and (b) bipolar montage. The nose positions are at the top of both plots. The gradient color bar at the bottom depicts the strength of electrical activity, with deep red being the strongest and deep blue being the weakest.

The signals from the individual channels C22, C23, C24, C29, C36, C42, and C52 as shown in Table 7 were extracted for further processing. Time series signals of referential recording channels (as listed in Table 5) and bipolar recording channels (as listed in Table 6) were then plotted and presented in Figure 50. Again, the left panel depicts the signal recorded with referential montage, while the right panel depicts the signals recorded with the bipolar montage. The inter-electrode Euclidean distances are labeled above each signal. Evident epileptic signals characterized by sharp high-frequency spikes can be observed from both panels. It can be seen that comparable amplitudes were demonstrated from both panels. The smaller baseline noises have been observed from the right panel. Based on these observations, we concluded that the bipolar

montage utilized in the single-unit sensor produced similar observable features compared to the standard 10-20 system employing referential montage.



**Figure 51.** Time series plot of 3-second epileptic EEG signals in (a) monopolar recording format as listed in Table 5, and (b) bipolar recording format as listed in Table 6. Two panels have the same horizontal and vertical scales.

## **8.0 SUMMARY OF THE WORK AND FUTURE EXTENSIONS**

This dissertation presents a single-unit sensor for rapid EEG measurement in ICUs and EDs. Series of investigations either analytically or experimentally warranted the efficacy of single-unit sensor in collecting EEG, including the epileptic seizure signal. Chapter 3.0 describes the concept of the single-unit sensor. In Chapter 4.0, a set of validations were carried out on both physical models and human subjects, and the feasibility of a closely spaced electrode configuration was investigated. The outcomes of this section provide experimental evidence to design a novel electrode structure of the single-unit sensor.

In Chapter 5.0, a fast computing algorithm was completed in Monte Carlo simulation. Based on more than one million simulation iterations, we concluded that the distribution of the signal strength of the proposed single-unit sensor electrode structure was comparable to the current gold standard of the 10-20 system. This conclusion indicates that the overall quantitative performance of the electrode structure in capturing EEG signal is comparable to systems employing the standard 10-20 system.

In Chapter 6.0, an electronic system emphasizing small size, low power, and other features specifically suited for the single unit sensor were carried out. The electrode structure prototypes were built with configurations similar to the feasibility test and simulation.

Subsequently, in Chapter 7.0, the electronic system was integrated into the single-unit sensor prototypes, and human subject experiments were conducted. Through series of experiments involving multiple tasks, the feasibility of the single-unit sensor prototype was validated in both time and frequency domains. Comparable performance to the gold cup electrodes was observed. The equivalence of the gold cup electrodes and the single-unit sensor were established at

comparable geometric scales. An indirect demonstration fulfilled the remaining gap in knowledge on the efficacy of the sensor in detecting epileptic signals. This demonstration was proceeded using a clinical epilepsy patient dataset with the recording configuration identical to the setup in the single-unit sensor. The sensor detected epileptic seizures, which had comparable signal features of the original data.

## **8.1 DISCUSSION**

In this work, a single-unit EEG sensor was proposed, and a prototype was constructed. A series of validations warranted the feasibility of the sensor in detecting epileptic seizure signals originate from NCS and NCSE. In this sensor, four electrodes with opposite ones as bipolar channels were placed within a  $20\text{ mm} \times 20\text{ mm}$  area. The results illustrated that the sensor with such high density and configuration of electrodes provided sufficient sensitivity in detecting potentials from small focal areas. Specifically, the case presented in the Section 7.2 demonstrated that the topological maps computed from the conventional electrode montage and bipolar recording using the single-unit sensor produced similar observable features. Thus, they appeared to have equivalent clinical diagnostic values.

Aside, the work also yielded a probabilistic model characterizing the statistical relationship between the dipolar source distribution within a multilayer spherical volume conductor and the potential distribution observed from the scalp. This statistical relationship provided feasibility insights into the design of a single-unit sensor. By applying the superposition principle, the potential due to multiple dipolar sources can be considered as a sum of potentials due to single dipoles. As a result, our derivation has a general significance.

## **8.2 CONTRIBUTION OF THE WORK**

The main contributions of this work are summarized as follows:

1. Theoretically, a statistical relationship was derived from the dipolar source distribution within a multilayer spherical volume conductor and the potential distribution observed from the scalp. This derivation enabled the evaluation of whether certain activities, such as epileptic seizures, taking place within the brain are observable from the scalp in a statistical sense.
2. A novel electrode structure for rapid attachment and capturing EEG was designed. Its validity in reliably collecting EEG data was demonstrated in a series of simulations, physical modeling, and human subject experiments.
3. A unique electronic system specifically for the single-unit EEG sensor was developed, featuring an integrated front-end with amplification and filtration, a new dynamic signal switch, a compact structural design, a wireless communication link, and a power-consumption optimization.
4. The feasibility of the proposed sensor in detecting epileptic signal from the EEG data was demonstrated.

## **8.3 RECOMMENDATIONS FOR FUTURE EXTENSIONS**

Some author's thoughts on future extensions of this work are listed here:

- The detection of waveforms of interest should be more convenient and accurate to improve the healthcare quality and reduce the associated cost. Continuous EEG monitoring

generates plenty of waveforms. Currently, physicians spent tremendous efforts on manual observations and interpretations of those waveforms. This manual effort can be problematic as the interpretation standards vary across different observers, which might lead to discrepancies [15]. Further, although quantitative EEG has currently supplemented portions of raw traces by graphical representations, they are not specific enough [15]. Thus, the improvement can be carried out in following aspects:

- Develop automated algorithms. Some classification algorithms, for example, utilizing deep neural networks, have surpassed the human-level accuracy [87].
  - The software implementing such algorithms could be made available to portable platforms to release the location constraint for medical personnel.
- Optimization of the current electrode structure. The thick layer of hair of certain patients often causes fixation problems during EEG recordings. For the single-unit sensor, the variation of head shapes very occasionally causes one of the electrodes not contacting the scalp surface. Design improvements can be carried out concerning the following two aspects:
  - The microscopic hooks structure at skin-contacting interface could be refined to release stronger skin-grabbing strength and ensure skin contact to improve signal quality.
  - The electrodes could function as a bi-directional communication path to the brain. It could continuously acquire EEG, and produce proper electric stimulation for neural modulations as well.

- With technological advancements including material fabrication and manufacturing techniques, the sensor hardware will be progressively improved, reflecting on following aspects:
  - It is expected to become lighter, smaller, with enhanced performances and better power optimization.
  - The whole sensor can be fabricated at a very low cost (on the order of several dollars). With significantly reduced cost, the future generations of sensor could be entirely disposable. This would further improve the logistical and procedural efficiency.
- In addition to the diagnosis of NCS/NCSE in emergency care, the single-unit sensor could be further extended to other applications. These applications include assessment of patients at the site of initial injury, monitoring the neurological status for athletes during completion, the study of sleep, detection of drowsy driving, providing inputs to brain-computer interface and virtual reality systems, and monitoring wounded soldiers on the battlefields, just to name a few.



## APPENDIX A

### ABBREVIATIONS

| Abbreviation | Definition                         |
|--------------|------------------------------------|
| AC           | Alternating Current                |
| ADC          | Analog-to-Digital Converter        |
| AGND         | Analog Ground                      |
| AMS          | Altered Mental Status              |
| ANOVA        | Analysis of Variance               |
| ASE          | Absence Status Epilepticus         |
| BEAM         | Brain Electrical Activity Mapping  |
| BEM          | Boundary Element Method            |
| BGA          | Ball Grid Array                    |
| BLE          | Bluetooth Low Energy               |
| BOM          | Bill of Materials                  |
| cEEG         | Continuous EEG                     |
| CFM          | Cerebral Function Monitor          |
| CMRR         | Common-Mode Rejection Ratio        |
| CPSE         | Complex Partial Status Epilepticus |
| CSA          | Compressed Spectral Array          |
| CSF          | Cerebrospinal Fluid                |
| CT           | Computerized Tomography            |
| DAQ          | Data Acquisition                   |
| DB           | D-Subminiature                     |
| DC           | Direct Current                     |
| DFT          | Discrete Fourier Transform         |
| DGND         | Digital Ground                     |
| DIN          | Digital Input                      |
| DOUT         | Digital Output                     |
| DRDY         | Data Ready                         |
| ECG          | Electrocardiography                |
| ED           | Emergency Department               |
| EEG          | Electroencephalography             |
| EGI          | Electrical Geodesics, Inc.         |
| EMF          | Electromotive Force                |
| EMI          | Electromagnetic Interference       |

|             |   |
|-------------|---|
| EMU         | Epilepsy Monitoring Unit                          |
| ER          | Emergency Room                                    |
| ERP         | Event-Related Potential                           |
| FDA         | US Food and Drug Administration                   |
| FEM         | Finite Element Method                             |
| fMRI        | functional Magnetic Resonance Imaging             |
| GUI         | Graphic User Interface                            |
| HCGSN       | HydroCel Geodesic Sensor Net                      |
| ICU         | Intensive Care Unit                               |
| IDE         | Integrated Development Environment                |
| IEEE        | Institute of Electrical and Electronics Engineers |
| IIR         | Infinite Impulse Response                         |
| IoT         | Internet of Things                                |
| IP          | Intellectual Property                             |
| IRB         | Institutional Review Board                        |
| JTAG        | Joint Test Action Group                           |
| LE          | Low Energy  |
| LTM         | Long-Term Monitoring                              |
| Mbps        | Megabits per second                               |
| MCU         | Microcontroller Unit                              |
| MEG         | Magnetoencephalography                            |
| MFR         | Manufacturer                                      |
| MPN         | Manufacturer Part Number                          |
| MUX         | Multiplexer                                       |
| NCS         | Non-Convulsive Seizures                           |
| NCSE        | Non-Convulsive Status Epilepticus                 |
| Neuro-ICU   | Neurological Intensive Care Unit                  |
| NI          | National Instruments                              |
| OEM         | Original Equipment Manufacturer                   |
| PC          | Personal Computer                                 |
| PCB         | Printed Circuit Board                             |
| PET         | Positron Emission Tomography                      |
| <i>pdf</i>  | probability density function                      |
| PSD         | Power Spectral Density                            |
| PWDN        | Power Down  |
| qEEG        | Quantitative Electroencephalography               |
| RCL         | Resistors, Capacitors and Inductors               |
| ROI         | Region of Interest                                |
| RTC         | Real-Time Control                                 |
| <i>r.v.</i> | random variable                                   |
| RF          | Radio Frequency                                   |
| RX          | Receive   |
| SCCN        | Swartz Center for Computational Neuroscience      |

|      |   |
|------|---|
| SDK  | Software Development Kit                    |
| SE   | Status Epilepticus                          |
| SMD  | Surface-Mount Device                        |
| SMT  | Surface-Mount Technology                    |
| SoC  | System on a Chip                            |
| SPI  | Serial Peripheral Interface                 |
| SPP  | Serial Port Profile                         |
| SQL  | Structured Query Language                   |
| SRAM | Static Random-Access Memory                 |
| TBM  | Topographic Brain Mapping                   |
| TCP  | Transmission Control Protocol               |
| TI   | Texas Instruments                           |
| TX   | Transmit                                    |
| UART | Universal Asynchronous Receiver/Transmitter |
| USB  | Universal Serial Bus                        |

## APPENDIX B

### ADS1299 REGISTER MAP

| Address  | Name       | Hex Value | BIT7 | BIT6 | BIT5 | BIT4 | BIT3 | BIT2 | BIT1 | BIT 0 |
|--|------------|-----------|------|------|------|------|------|------|------|-------|
| <b>Device Settings (Read-Only Registers)</b>           |            |           |      |      |      |      |      |      |      |       |
| 00h  | ID         | 0x03E     | 0    | 0    | 1    | 1    | 1    | 1    | 1    | 0     |
| <b>Global Settings Across Channels</b>                 |            |           |      |      |      |      |      |      |      |       |
| 01h  | CONFIG1    | 0x96      | 1    | 0    | 0    | 1    | 0    | 1    | 1    | 0     |
| 02h  | CONFIG2    | 0xC0      | 1    | 1    | 0    | 0    | 0    | 0    | 0    | 0     |
| 03h  | CONFIG3    | 0x68      | 0    | 1    | 1    | 0    | 1    | 0    | 0    | 0     |
| 04h  | LOFF       | 0x02      | 0    | 0    | 0    | 0    | 0    | 0    | 1    | 0     |
| <b>Channel-Specific Settings</b>                       |            |           |      |      |      |      |      |      |      |       |
| 05h  | CH1SET     | 0x60      | 0    | 1    | 1    | 0    | 0    | 0    | 0    | 0     |
| 06h  | CH2SET     | 0x60      | 0    | 1    | 1    | 0    | 0    | 0    | 0    | 0     |
| 07h  | CH3SET     | 0xE0      | 1    | 1    | 1    | 0    | 0    | 0    | 0    | 0     |
| 08h  | CH4SET     | 0xE0      | 1    | 1    | 1    | 0    | 0    | 0    | 0    | 0     |
| 09h  | CH5SET     | 0xE0      | 1    | 1    | 1    | 0    | 0    | 0    | 0    | 0     |
| 0Ah  | CH6SET     | 0xE0      | 1    | 1    | 1    | 0    | 0    | 0    | 0    | 0     |
| 0Bh  | CH7SET     | 0xE0      | 1    | 1    | 1    | 0    | 0    | 0    | 0    | 0     |
| 0Ch  | CH8SET     | 0xE0      | 1    | 1    | 1    | 0    | 0    | 0    | 0    | 0     |
| 0Dh  | BIAS_SENSP | 0x00      | 0    | 0    | 0    | 0    | 0    | 0    | 0    | 0     |
| 0Eh  | BIAS_SENSN | 0x00      | 0    | 0    | 0    | 0    | 0    | 0    | 0    | 0     |
| 0Fh  | LOFF_SENSP | 0x00      | 0    | 0    | 0    | 0    | 0    | 0    | 0    | 0     |
| 10h  | LOFF_SENSN | 0x00      | 0    | 0    | 0    | 0    | 0    | 0    | 0    | 0     |
| 11h  | LOFF_FLIP  | 0x00      | 0    | 0    | 0    | 0    | 0    | 0    | 0    | 0     |
| <b>Lead-Off Status Registers (Read-Only Registers)</b> |            |           |      |      |      |      |      |      |      |       |
| 12h  | LOFF_STATP | 0x00      | 0    | 0    | 0    | 0    | 0    | 0    | 0    | 0     |
| 13h  | LOFF_STATN | 0x00      | 0    | 0    | 0    | 0    | 0    | 0    | 0    | 0     |
| <b>GPIO and OTHER Registers</b>                        |            |           |      |      |      |      |      |      |      |       |
| 14h  | GPIO       | 0x0F      | 0    | 0    | 0    | 0    | 1    | 1    | 1    | 1     |
| 15h  | MISC1      | 0x00      | 0    | 0    | 0    | 0    | 0    | 0    | 0    | 0     |
| 16h  | MISC2      | 0x00      | 0    | 0    | 0    | 0    | 0    | 0    | 0    | 0     |
| 17h  | CONFIG4    | 0x00      | 0    | 0    | 0    | 0    | 0    | 0    | 0    | 0     |

\* The red-colored fonts denote the values were different from default factory setting.

\* The original ADS1299 register map can be found in [83].

## APPENDIX C

### SINGLE-UNIT SENSOR HARDWARE BILL OF MATERIALS (BOM)

| Description   | MFR                                | MPN                 | Quantity | Unit Price (\$) | Total (\$) | Unit Price (\$ (3,000 ordered)) |
|---|------------------------------------|---------------------|----------|-----------------|------------|---------------------------------|
| <b>Components Cost</b>  |                                    |                     |          |                 |            |                                 |
| Low-Noise, 8-Channel, 24-bit analog Front-End for Biopotential Measurements | Texas Instruments                  | ADS1299IPAG         | 1        | 56.43           | 56.43      | 20.59                           |
| IC MCU 8BIT 32 KB FLASH 32TQFP  | Microchip Technology               | ATMEGA              | 1        | 1.38            | 1.38       | 1.31                            |
| CC2541 BLE minimal system board   | Ghostyu Technology                 | BLE-M0              | 1        | 3.68            | 3.68       | 2.94                            |
| High-Efficient Single Inductor Buck-Boost Converter With 1.8-A Switches     | Texas Instruments                  | TPS63000DRCR        | 1        | 2.32            | 2.32       | 0.95625                         |
| 100 mA Regulated Charge-Pump Inverters in ThinSOT                           | Linear Technology                  | LTC1983ES6-5#TRMPBF | 1        | 4.28            | 4.28       | 1.90952                         |
| IC REG LDO 2.5 V 0.15 A SC70-5  | Texas Instruments                  | TPS71725DCKR        | 1        | 1.1             | 1.1        | 0.40500                         |
| IC REG LDO NEG ADJ 0.2 A SOT23-5  | Texas Instruments                  | TPS72301DBVR        | 1        | 2.87            | 2.87       | 1.18125                         |
| IC OPAMP GP 5.5 MHZ RRO SOT23-5   | Texas Instruments                  | OPA376AIDBVR        | 1        | 1.78            | 1.78       | 0.73125                         |
| OSC XO 156.25 MHZ HCMOS SMD   | IDT, Integrated Device Technology  | FXO-HC735RGB-156.25 | 1        | 1.58            | 1.58       | 0.5835                          |
| IC SWITCH QUAD SPDT 20LFCSP   | Analog Devices                     | ADG788BCPZ          | 1        | 3.98            | 3.98       | 1.92                            |
| RES SMD XX OHM 1% 1/20 W 0201   | Panasonic Electronic Components    | RC0402JR-071KL      | 50       | 0.10            | 5          | 0.00465                         |
| CAP CER XX UF 6.3 V X5R 0201  | AVX Corporation                    | 02016D104KAT2A      | 25       | 0.10            | 2.5        | 0.00168                         |
| CAP CER 10UF 6.3 V X6S 0402   | Murata Electronics North America   | GRM155C80J106ME11D  | 25       | 0.17            | 4.25       | 0.02226                         |
| LED 0402 SMD  | Vishay Semiconductor Opto Division | VLMS1500-GS08       | 5        | 0.53            | 2.65       | 0.0768                          |
| FIXED IND XX NH 300 MA 500 MOHM   | Johanson Technology                | L-05B4N7SV6T        | 25       | 0.10            | 2.5        | 0.01105                         |
| <b>Board Cost</b>   |                                    |                     |          |                 |            |                                 |
| 4 cm <sup>2</sup> FR4 0.03" Lead Free LPI Four Layer PCB                    | Advanced Circuits                  | N/A                 | 2        | 150             | 300        | 5                               |
| <b>Electrode Cost</b>   |                                    |                     |          |                 |            |                                 |

|  |                       |     |   |      |      |      |
|--|-----------------------|-----|---|------|------|------|
| 316L grade stainless steel screw electrode | Fotofab               | N/A | 1 | 1000 | 1000 | 0.02 |
| Gold Coating                               | Gold Plating Services | N/A | 1 | 20   | 20   | 1    |

The estimated material cost to make one single-unit sensor is \$1416.3. The estimated average material cost to make one single-unit sensor when more than 3,000 sensors are planned is \$38.67.

The currency rate conversion between USD to RMB is assumed to be 1 Dollar to 6.80 Yuan. All manufacturing quotes and purchase prices were as of 2017 May. The part ordered with quantity greater than 3,000 might not have the same MPN and MFR as the part ordered with quantity of less. The quantities of RCL and other circuit components logged in the table might be approximated numbers used on the sensor prototype.

## APPENDIX D

### ELECTRODE-SKIN CONTACT IMPEDANCE MEASUREMENTS

|        |   |       |                    | P-N (k $\Omega$ ) | P-BIAS (k $\Omega$ ) | N-BIAS (k $\Omega$ ) |
|--------|---|-------|--------------------|-------------------|----------------------|----------------------|
|        |   |       |                    |                   |                      |                      |
| Task 1 | Contact-impedance<br>BEFORE measurement | 20 mm | gold cup           | 17.0              | 4.5                  | 14.5                 |
|        |   |       | single-unit sensor | 31.7              | 32.1                 | 30.4                 |
|        |   | 24 mm | gold cup           | 16.0              | 7.7                  | 11.9                 |
|        |   |       | single-unit sensor | 35.8              | 20.0                 | 27.7                 |
|        |   | 28 mm | gold cup           | 5.7               | 5.1                  | 4.8                  |
|        |   |       | single-unit sensor | 10.0              | 4.6                  | 7.9                  |
|        |   | 32 mm | gold cup           | 38.4              | 17.4                 | 39.0                 |
|        |   |       | single-unit sensor | 89.3              | 41.1                 | 88.3                 |
|        | Contact-impedance<br>AFTER measurement  | 20 mm | gold cup           | 39.9              | 17.1                 | 30.3                 |
|        |   |       | single-unit sensor | 31.5              | 32.0                 | 26.5                 |
|        |   | 24 mm | gold cup           | 17.0              | 12.3                 | 10.2                 |
|        |   |       | single-unit sensor | 30.4              | 12.8                 | 26.7                 |
|        |   | 28 mm | gold cup           | 6.0               | 5.5                  | 5.3                  |
|        |   |       | single-unit sensor | 10.4              | 4.8                  | 8.5                  |
|        |   | 32 mm | gold cup           | 52.6              | 21.3                 | 55.0                 |
|        |   |       | single-unit sensor | 86.3              | 41.6                 | 83.3                 |
| Task 2 | Contact-impedance<br>BEFORE measurement | 20 mm | gold cup           | 39.9              | 17.1                 | 30.3                 |
|        |   |       | single-unit sensor | 28.6              | 23.5                 | 26.9                 |
|        |   | 24 mm | gold cup           | 17.5              | 12.9                 | 10.3                 |
|        |   |       | single-unit sensor | 24.7              | 15.6                 | 17.6                 |
|        |   | 28 mm | gold cup           | 5.8               | 5.3                  | 4.4                  |
|        |   |       | single-unit sensor | 10.4              | 4.8                  | 8.5                  |
|        |   | 32 mm | gold cup           | 27.2              | 10.6                 | 27.4                 |
|        |   |       | single-unit sensor | 86.3              | 41.6                 | 83.3                 |
|        | Contact-impedance<br>AFTER measurement  | 20 mm | gold cup           | 47.2              | 21.7                 | 35.2                 |
|        |   |       | single-unit sensor | 31.7              | 32.1                 | 30.4                 |
|        |   | 24 mm | gold cup           | 18.4              | 14.9                 | 10.7                 |
|        |   |       | single-unit sensor | 35.8              | 20.0                 | 27.7                 |
|        |   | 28 mm | gold cup           | 5.6               | 5.0                  | 4.7                  |
|        |   |       | single-unit sensor | 10.8              | 5.1                  | 10.8                 |
|        |   | 32 mm | gold cup           | 38.4              | 17.4                 | 39.0                 |
|        |   |       | single-unit sensor | 77.8              | 43.4                 | 83.6                 |

## BIBLIOGRAPHY

1. Shneker, B.F. and N.B. Fountain, *Assessment of acute morbidity and mortality in nonconvulsive status epilepticus*. Neurology, 2003. **61**(8): p. 1066-1073.
2. Young, B.G., K.G. Jordan, and G.S. Doig, *An assessment of nonconvulsive seizures in the intensive care unit using continuous EEG monitoring an investigation of variables associated with mortality*. Neurology, 1996. **47**(1): p. 83-89.
3. Claassen, J., et al., *Detection of electrographic seizures with continuous EEG monitoring in critically ill patients*. Neurology, 2004. **62**(10): p. 1743-1748.
4. Meierkord, H. and M. Holtkamp, *Non-convulsive status epilepticus in adults: clinical forms and treatment*. The Lancet Neurology, 2007. **6**(4): p. 329-339.
5. Drislane, F.W., *Presentation, evaluation, and treatment of nonconvulsive status epilepticus*. Epilepsy & Behavior, 2000. **1**(5): p. 301-314.
6. Abend, N.S., et al., *Use of EEG monitoring and management of non-convulsive seizures in critically ill patients: a survey of neurologists*. Neurocritical care, 2010. **12**(3): p. 382-389.
7. Jordan, K.G., *Continuous EEG monitoring in the neuroscience intensive care unit and emergency department*. Journal of clinical neurophysiology, 1999. **16**(1): p. 14-39.
8. Jordan, K., *Nonconvulsive seizures (NCS) and nonconvulsive status epilepticus (NCSE) detected by continuous EEG monitoring in the neuro ICU*. Neurology, 1992. **42**(Suppl 1): p. 194.
9. Abend, N.S., et al., *Nonconvulsive seizures are common in critically ill children*. Neurology, 2011. **76**(12): p. 1071-1077.
10. Jordan, K.G., *Neurophysiologic monitoring in the neuroscience intensive care unit*. Neurologic clinics, 1995. **13**(3): p. 579-626.
11. Claassen, J., et al., *Recommendations on the use of EEG monitoring in critically ill patients: consensus statement from the neurointensive care section of the ESICM*. Intensive care medicine, 2013. **39**(8): p. 1337-1351.
12. Thibault, G.E., et al., *Medical intensive care: indications, interventions, and outcomes*. New England Journal of Medicine, 1980. **302**(17): p. 938-942.
13. Lemeshow, S. and J.-R. Le, *Modeling the severity of illness of ICU patients: a systems update*. Jama, 1994. **272**(13): p. 1049-1055.
14. Sun, M., et al., *Single-unit leadless eeg sensor*. 2016, Google Patents.
15. Friedman, D., J. Claassen, and L.J. Hirsch, *Continuous electroencephalogram monitoring in the intensive care unit*. Anesthesia & Analgesia, 2009. **109**(2): p. 506-523.
16. Brenner, R.P., *Is it status?* Epilepsia, 2002. **43**(s3): p. 103-113.



17. Jette, N., et al., *Frequency and predictors of nonconvulsive seizures during continuous electroencephalographic monitoring in critically ill children*. Archives of Neurology, 2006. **63**(12): p. 1750-1755.
18. Claassen, J., et al., *Electrographic seizures and periodic discharges after intracerebral hemorrhage*. Neurology, 2007. **69**(13): p. 1356-1365.
19. Litt, B., et al., *Nonconvulsive status epilepticus in the critically ill elderly*. Epilepsia, 1998. **39**(11): p. 1194-1202.
20. Jordan, K., G. Young, and G. Doig, *Delays in emergency department (ED) diagnosis and treatment of nonconvulsive status epilepticus*. Neurology, 1995. **45**(suppl 4): p. 346.
21. Jordan, K.G., *Nonconvulsive status epilepticus in acute brain injury*. Journal of clinical neurophysiology, 1999. **16**(4): p. 332-340.
22. Laccheo, I., et al., *Non-convulsive status epilepticus and non-convulsive seizures in neurological ICU patients*. Neurocritical care, 2015. **22**(2): p. 202-211.
23. Kaplan, P.W., *Nonconvulsive status epilepticus in the emergency room*. Epilepsia, 1996. **37**(7): p. 643-650.
24. Dasta, J.F., et al., *Daily cost of an intensive care unit day: the contribution of mechanical ventilation*. Critical care medicine, 2005. **33**(6): p. 1266-1271.
25. Penberthy, L., et al., *Estimating the economic burden of status epilepticus to the health care system*. Seizure, 2005. **14**(1): p. 46-51.
26. Krumholz, A., *Epidemiology and evidence for morbidity of nonconvulsive status epilepticus*. Journal of clinical neurophysiology, 1999. **16**(4): p. 314-322.
27. Lennox, W.G., *The petit mal epilepsies: their treatment with tridione*. Journal of the American Medical Association, 1945. **129**(16): p. 1069-1074.
28. Krumholz, A., et al., *Complex partial status epilepticus accompanied by serious morbidity and mortality*. Neurology, 1995. **45**(8): p. 1499-1504.
29. Jordan, K.G., *Continuous EEG and evoked potential monitoring in the neuroscience intensive care unit*. Journal of Clinical Neurophysiology, 1993. **10**(4): p. 445-475.
30. Caton, R., *Electrical Currents of the Brain*. The Journal of Nervous and Mental Disease, 1875. **2**(4): p. 610.
31. Berger, H., *Über das Elektrenkephalogramm des Menschen*. Archiv für Psychiatrie und Nervenkrankheiten, 1929. **87**(1): p. 527-570.
32. Collura, T.F., *History and evolution of electroencephalographic instruments and techniques*. Journal of clinical neurophysiology, 1993. **10**(4): p. 476-504.
33. Fischer, M. and H. Löwenbach, *Aktionsströme des Zentralnervensystems unter der Einwirkung von Krampfgiften*. Naunyn-Schmiedeberg's Archives of Pharmacology, 1934. **174**(5): p. 502-516.
34. Gibbs, F.A., H. Davis, and W.G. Lennox, *The electro-encephalogram in epilepsy and in conditions of impaired consciousness*. Archives of Neurology & Psychiatry, 1935. **34**(6): p. 1133-1148.

35. Michel, C.M., et al., *128-channel EEG source imaging in epilepsy: clinical yield and localization precision*. Journal of Clinical Neurophysiology, 2004. **21**(2): p. 71-83.
36. Smith, S., *EEG in the diagnosis, classification, and management of patients with epilepsy*. Journal of Neurology, Neurosurgery & Psychiatry, 2005. **76**(suppl 2): p. ii2-ii7.
37. Salinsky, M., R. Kanter, and R.M. Dasheiff, *Effectiveness of multiple EEGs in supporting the diagnosis of epilepsy: an operational curve*. Epilepsia, 1987. **28**(4): p. 331-334.
38. Noachtar, S. and J. Rémi, *The role of EEG in epilepsy: a critical review*. Epilepsy & Behavior, 2009. **15**(1): p. 22-33.
39. He, B., *Neural Engineering*. 2007: Springer US.
40. Holmes, M.D., *Dense array EEG: methodology and new hypothesis on epilepsy syndromes*. Epilepsia, 2008. **49**(s3): p. 3-14.
41. Jurcak, V., D. Tsuzuki, and I. Dan, *10/20, 10/10, and 10/5 systems revisited: their validity as relative head-surface-based positioning systems*. Neuroimage, 2007. **34**(4): p. 1600-1611.
42. Hämäläinen, M., et al., *Magnetoencephalography—theory, instrumentation, and applications to noninvasive studies of the working human brain*. Reviews of modern Physics, 1993. **65**(2): p. 413.
43. Geddes, L., *Historical evolution of circuit models for the electrode-electrolyte interface*. Annals of biomedical engineering, 1997. **25**(1): p. 1-14.
44. Chi, Y.M., T.-P. Jung, and G. Cauwenberghs, *Dry-contact and noncontact biopotential electrodes: Methodological review*. IEEE reviews in biomedical engineering, 2010. **3**: p. 106-119.
45. Searle, A. and L. Kirkup, *A direct comparison of wet, dry and insulating bioelectric recording electrodes*. Physiological measurement, 2000. **21**(2): p. 271.
46. Huigen, E., A. Peper, and C. Grimbergen, *Investigation into the origin of the noise of surface electrodes*. Medical and biological engineering and computing, 2002. **40**(3): p. 332-338.
47. Tallgren, P., et al., *Evaluation of commercially available electrodes and gels for recording of slow EEG potentials*. Clinical Neurophysiology, 2005. **116**(4): p. 799-806.
48. Cooper, R., J.W. Osselson, and J.C. Shaw, *EEG technology*. 2014: Butterworth-Heinemann.
49. Teplan, M., *Fundamentals of EEG measurement*. Measurement science review, 2002. **2**(2): p. 1-11.
50. Jasper, H.H., *The ten twenty electrode system of the international federation*. Electroencephalography and clinical neurophysiology, 1958. **10**: p. 371-375.
51. Nunez, P., et al., *A theoretical and experimental study of high resolution EEG based on surface Laplacians and cortical imaging*. Electroencephalography and clinical neurophysiology, 1994. **90**(1): p. 40-57.

52. Chatrian, G., E. Lettich, and P. Nelson, *Ten percent electrode system for topographic studies of spontaneous and evoked EEG activities*. American Journal of EEG technology, 1985. **25**(2): p. 83-92.
53. Oostenveld, R. and P. Praamstra, *The five percent electrode system for high-resolution EEG and ERP measurements*. Clinical neurophysiology, 2001. **112**(4): p. 713-719.
54. Nuwer, M.R., *Quantitative EEG: I. Techniques and problems of frequency analysis and topographic mapping*. Journal of Clinical Neurophysiology, 1988. **5**(1): p. 1-44.
55. Nuwer, M.R., *Quantitative EEG: II. Frequency analysis and topographic mapping in clinical settings*. Journal of Clinical Neurophysiology, 1988. **5**(1): p. 45-86.
56. Taflove, A. and S.C. Hagness, *Computational Electrodynamics: The Finite-difference Time-domain Method*. 2005: Artech House.
57. Huhta, J.C. and J.G. Webster, *60-Hz interference in electrocardiography*. IEEE Transactions on Biomedical Engineering, 1973(2): p. 91-101.
58. Sun, M., et al. *A low-impedance, skin-grabbing, and gel-free EEG electrode*. in *Engineering in Medicine and Biology Society (EMBC), 2012 Annual International Conference of the IEEE*. 2012. IEEE.
59. Sun, M., et al., *Skin screw electrode*. 2012, Google Patents.
60. Tam, H. and J.G. Webster, *Minimizing electrode motion artifact by skin abrasion*. IEEE Transactions on Biomedical Engineering, 1977(2): p. 134-139.
61. Webster, J.G., *Reducing motion artifacts and interference in biopotential recording*. IEEE Transactions on Biomedical Engineering, 1984(12): p. 823-826.
62. Brown, H.D., *New and interesting grasshoppers from southern Africa-3 (Orthoptera: Acridoidea)*. Journal of the Entomological Society of Southern Africa, 1962. **25**(2): p. 198-229.
63. Saver, J.L., *Time is brain—quantified*. Stroke, 2006. **37**(1): p. 263-266.
64. Meldrum, B.S., R.A. Vigouroux, and J.B. Brierley, *Systemic factors and epileptic brain damage: prolonged seizures in paralyzed, artificially ventilated baboons*. Archives of Neurology, 1973. **29**(2): p. 82-87.
65. Instruments, T. and B. Brown, *INA118 Data Sheet*. 1998, Abril.
66. Sallen, R.P. and E.L. Key, *A practical method of designing RC active filters*. IRE Transactions on Circuit Theory, 1955. **2**(1): p. 74-85.
67. Stok, C.J., *The influence of model parameters on EEG/MEG single dipole source estimation*. Biomedical Engineering, IEEE Transactions on, 1987(4): p. 289-296.
68. Stok, C.J., *The inverse problem in EEG and MEG with application to visual evoked responses*. 1986: SI.
69. Sidman, R., et al., *A method for localization of sources of human cerebral potentials evoked by sensory stimuli*. Sensory Processes, 1978.
70. Luan, B., et al. *A feasibility study on a single-unit wireless EEG sensor*. in *Signal Processing (ICSP), 2014 12th International Conference on*. 2014. IEEE.

71. da Silva, F.L., *EEG: Origin and measurement*, in *EEG-fMRI*. 2010, Springer. p. 19-38.
72. Yan, Y., P. Nunez, and R. Hart, *Finite-element model of the human head: scalp potentials due to dipole sources*. Medical and Biological Engineering and Computing, 1991. **29**(5): p. 475-481.
73. He, B., Y. Wang, and D. Wu, *Estimating cortical potentials from scalp EEGs in a realistically shaped inhomogeneous head model by means of the boundary element method*. IEEE Transactions on Biomedical Engineering, 1999. **46**(10): p. 1264-1268.
74. Cuffin, B.N. and D. Cohen, *Comparison of the magnetoencephalogram and electroencephalogram*. Electroencephalography and clinical neurophysiology, 1979. **47**(2): p. 132-146.
75. Sun, M., *An efficient algorithm for computing multishell spherical volume conductor models in EEG dipole source localization*. Biomedical Engineering, IEEE Transactions on, 1997. **44**(12): p. 1243-1252.
76. Murakami, S. and Y. Okada, *Contributions of principal neocortical neurons to magnetoencephalography and electroencephalography signals*. The Journal of physiology, 2006. **575**(3): p. 925-936.
77. Kandel, E.R., J.H. Schwartz, and T.M. Jessell, *Principles of neural science*. Vol. 4. 2000: McGraw-Hill New York.
78. Nunez, P.L. and R. Srinivasan, *Electric fields of the brain: the neurophysics of EEG*. 2006: Oxford University Press, USA.
79. Luan, B. and M. Sun. *A simulation study on a single-unit wireless EEG Sensor*. in *Biomedical Engineering Conference (NEBEC), 2015 41st Annual Northeast*. 2015. IEEE.
80. Kiourti, A. and K.S. Nikita, *Design of implantable antennas for medical telemetry: Dependence upon operation frequency, tissue anatomy, and implantation site*. International Journal of Monitoring and Surveillance Technologies Research (IJMSTR), 2013. **1**(1): p. 16-33.
81. Niedermeyer, E. and F.L. da Silva, *Electroencephalography: basic principles, clinical applications, and related fields*. 2005: Lippincott Williams & Wilkins.
82. Kay, S., *Intuitive probability and random processes using MATLAB®*. 2006: Springer Science & Business Media.
83. Instruments, T., *Low-Noise, 8-Channel, 24-Bit Analog Front-End for Biopotential Measurements ADS1299*. Datasheet.
84. *MSP430F543x and MSP430F541x Mixed-Signal Microcontrollers Datasheet*.; Available from: <http://www.ti.com/lit/ds/symlink/msp430f5419.pdf>.
85. Decuir, J., *Bluetooth 4.0: Low Energy*. Cambridge, UK: Cambridge Silicon Radio SR plc, 2010.
86. *ATmega328/P 8-bit microcontrollers datasheet*. .
87. Sze, V., et al., *Efficient processing of deep neural networks: A tutorial and survey*. arXiv preprint arXiv:1703.09039, 2017.